Global Stability Analysis of Non-parallel Flows

A Thesis

Submitted for the Degree of

DOCTOR OF PHILOSOPHY

in the Faculty of Engineering

by

GAYATHRI SWAMINATHAN

ENGINEERING MECHANICS UNIT
JAWAHARLAL NEHRU CENTRE FOR ADVANCED SCIENTIFIC RESEARCH
(A Deemed University)
Bangalore – 560 064

November 2010

To My Father

DECLARATION

I hereby declare that the matter embodied in the thesis entitled "**Global Stability Analysis of Non-parallel Flows**" is the result of investigations carried out by me at the Engineering Mechanics Unit, Jawaharlal Nehru Centre for Advanced Scientific Research, Bangalore, India under the supervision of Prof. Rama Govindarajan and that it has not been submitted elsewhere for the award of any degree or diploma.

In keeping with the general practice in reporting scientific observations, due acknowledgment has been made whenever the work described is based on the findings of other investigators.

Gayathri Swaminathan

CERTIFICATE

I hereby certify that the matter embodied in this thesis entitled "**Global Stability Analysis of Non-parallel Flows**" has been carried out by Ms. Gayathri Swaminathan at the Engineering Mechanics Unit, Jawaharlal Nehru Centre for Advanced Scientific Research, Bangalore, India under my supervision and that it has not been submitted elsewhere for the award of any degree or diploma.

Prof. Rama Govindarajan
(Research Supervisor)

Acknowledgements

Contents

Abstract

The main motivation of my work has been to study the stability characteristics of spatially developing flows. Transition is triggered by instability of the base state and understanding the stability characteristics has great implications in flow control.

Most of the earlier work on flow stability use the local approach, wherein, the stability characteristics are determined based on the local velocity profile. Many of these studies aim at finding the critical Reynolds number (Re_{crit}) above which the flow will become unstable. This appproach is valid when the base flow profile does not vary much between locations or does not vary at all. Common examples are flow through a straight channel, flat plate boundary layer at high Re, which are a parallel flow and a weakly non-parallel flow respectively. In most real life flow situations the non-parallelism is not weak, i.e., the profiles and flow vary drastically in the streamwise direction. While the former type of flows can be studied using a local approach, the latter need to be studied using a global approach. The first step in the present work is to develop a software to perform global stability on many complex flow geometries. With this, we study three non-parallel flows and report new instability characteristics. Many flows have been studied using a global stability approach. In boundary layer type flows these studies find stability behavior that is very similar qualitatively to what local studies already foretold. In very complex geometries they obtain global modes that are actually localized to certain portions of the geometry which bear no resemblance to the wave-like disturbances of local studies.

The objective of most of the global studies has usually been to design the most effective control strategy. Our focus is quite different. It is to understand some basic ways in which non-parallel flows differ from parallel. The first flow studied is that through an infinitely diverging channel, namely Jeffery-Hamel flow. This is chosen as it is the simplest non-parallel flow. The Reynolds number of this flow is constant downstream and

the profile is self-similar. While it is well known that the critical Reynolds number of this flow is dramatically sensitive to wall divergence, the cause of this sensitivity is not explained in the literature. We begin by asking why this happens and propose a scaling argument, which gives a good approximation for variation in the Re_{crit} with wall divergence. The estimation of Re_{cr} uses only results from the straight channel. We show that even in this simplest non-parallel flow, the global instability modes recovered are very different from what one would obtain by making a weakly non-parallel assumption. We also show using a wavelet transform of the global modes that a perceived 'wavenumber' of a global mode can change with streamwise and wall-normal directions, a result not reported before to our knowledge. Most importantly, the modes are not wave-like, whereas stability studies so far have made this assumption. This questions the validity of Robin boundary conditions commonly used in global stability analysis, which impose a wave-like boundary condition on the disturbances. We also report that a few global modes can propagate upstream, in contrast to the local modes which have a positive phase velocity. Since a Jeffery-Hamel flow is not realizable in experiments, we study a more realistic geometry, where the divergence is confined to a short region of a straight channel and find no qualitative difference in the stability characteristics. The base flow for this geometry is obtained by direct numerical simulations of the Navier-Stokes equations using a full multi-grid technique.

Next, we study the flow through a channel with a series of divergent and convergent sections, but whose average width is constant. Onemotivation for such a geometry is to achieve low Reynolds number instability. We study channels with large wall waviness amplitudes, in contrast to most previous studies which study small waviness amplitudes. This is because our ultimate aim is to achieve good mixing in these channels whereas previous studies aim at studying the effect of surface roughness. In contrast to all previous work, we introduce fore-aft asymmetry in the channels and get significant differences from previous studies. We also show that the periodic boundary conditions used in all the previous studies of these flows is not valid, as the flow exhibits a new type of spatial growth, which we term as an instability ratchet. This instability ratchet is defined as the sequential spatial growth in the energy of the disturbances over successive periodic units. Modes exhibiting a spatial ratchet are interesting because they can enhance both transient growth and nonlinearities downstream. We find in fact that these flows exhibit localized pockets of large transient growth. Hence the transient growth characteristics of these flows need to be determined on a local basis and not in the traditional

integrated way. In addition, we get exponential instability of the global modes at Re as low as 50, by introducing large wall waviness amplitudes. By performing a numerical Floquet analysis, we find that several manifestations of instability are possible and show that the instability contained in a mode may be demonstrated in time or space. We find that increase in one type of instability leads to a decrease in other one and this interplay is enhanced by the introduction of the fore-aft asymmetry in the channel walls. We also show that the growth behaviour of these global modes cannot be described by a single Floquent exponent and it is space and scale dependent. This problem has a large number of parameters involved and we study a wide range of parameters to make comparisons.

We finally study the stability characteristics of a fully developed wall jet, which obeys self-similarity at large Re. A local stability study on this flow predicts a neutral curve in which there is a small stable region within the unstable regime. This was attributed to the presence of two types of instability modes but cannot be explained on physical grounds. No researchers to our knowledge have attempted to understand what happens behind this stable bubble, and we study this region on a local basis using the Orr-Sommerfeld equation. We also perform global stability computations on a longer domain and obtain global modes. The critical Reynolds number obtained from a global approach coincides with that predicted by a local approach. In the case of wall jets, the global modes obtained exhibit a small amount of non-wave-like behaviour. However the differences between the local and global stability results are much smaller in this flow than in the previous two.

Refereed conference papers

- An instability ratchet at low Reynolds number channel flows, Accepted for presentation at the Eighth Euromech Fluid Mechanics Conference, to be held in Germany, September 2010.

- Global instabilities in non-symmetric convergent-divergent channels, ISBN-13: 978-84-692-6247-4, Proceedings of Fourth Symposium on Global Flow Instability and Control, Crete, Greece, September 2009.

- Global instabilities in wall jets, Gayathri Swaminathan, A Sameen and Rama Govindarajan, Proceedings of the Seventh IUTAM Symposium on Laminar Turbulent Transition, Stockholm, Sweden, June 2009.

- A general method of linear instability computations for flow through arbitrary two-dimensional geometries, Proceedings of Seventh Asian Computational Fluid Dynamics Conference, Bangalore, November 2007.

Journal publications

- Global instabilities in diverging channel flows, Gayathri Swaminathan, K. C. Sahu, A. Sameen and Rama Govindarajan, Theoretical and Computational Fluid Dynamics, Special Issue on Global Instability Complex, Published online March 2010, In press.

- An instability ratchet in low Reynolds number converging-diverging channel flows, Gayathri Swaminathan and Rama Govindarajan, Manuscript under preparation.

List of Figures

List of Tables

CHAPTER 1

INTRODUCTION

1.1 Stability Analysis of Fluid Flows

Most shear flows are spatially developing, i.e., their velocity profile evolves as the flow proceeds downstream. Typically, as the Reynolds number increases, the laminar shear flow undergoes a linear instability, followed by an often complicated, and not completely understood, route to turbulence. Oftentimes, the flow might not undergo the different stages of instability, but directly becomes turbulent, through a process called bypass transition. The route which a flow chooses to become turbulent by depends upon many parameters like goemetry, free stream disturbances, etc. As with any work on flow stability and transition, this thesis also starts by referring to the work of Osborne Reynolds in 1883, which was the first systematic study on the stability of flow through pipes. The review paper by Jackson & Launder (2007) discusses the two important papers by Reynolds and his interactions with the referees, that have so greatly influenced the development of Engineering Fluid Mechanics over the past century.

To perform stability analysis of a flow, the laminar state is perturbed and the evolution of the disturbances is monitored to see if the disturbances grow or decay. A growing disturbance indicates an unstable system, while the disturbances decay in a stable system. It is very important to understand the stability characteristics of a flow, as it plays a major role in flow control. In situations where we require the flow to be laminar, the disturbance energy growth has to be curbed whereas in situations where we prefer a turbulent flow, the disturbance energy growth is enhanced. This suppression or enhancement of the disturbance energy could be performed in many ways, like blowing and suction, heating and cooling, vortex generators, etc. The above mentioned techniques fall under active flow control methods. The disturbance energy can also be tuned by passive options where, for example, the geometry is optimally designed. To perform flow control, we need information about what to control, where to control and how to control. This information is obtained from the disturbance and it is obtained a-priori by doing a stability analysis. Thus, stability analysis is the first step in flow control. In addition, stability analysis gives us information about the underlying physics of the less-understood (in many cases), transition process. The main aim of the present work is to try to understand

the characteristics of flow through non-parallel, but not very complicated geometries.

In the past it was assumed that stability properties can be determined by studying the local velocity profile. In any non-parallel flow, such an assumption need not hold good. In chapter 2, a discussion about global stability analysis is done, along with an introduction to non-parallel flows. It will be seen that this approach is not restricted by any type of assumption and it can be used to study the stability characteristics of flow through complicated geometries too. In this work, global stability approach has been used to study both bounded and semi-bounded flows, namely channel flows and wall jets. This approach can also be easily extended to unbounded flows like wakes and mixing layers, without any violation of assumptions.

Linear stability theory predicts that the flow through a straight channel becomes unstable for Reynolds numbers greater than 5772. But in real life this flow becomes unstable at much lower Reynolds number and this phenomenon is called subcritical transition. Nishioka *et al.* (1975) showed that by reducing the free stream disturbances and by making the walls of the channel extremely smooth, this flow can be maintained in a laminar state well above the critical Reynolds number. This hints about the effect of surface roughness, and in turn the change in geometry, on flow stability. It is well known that divergence and convergence in a channel have a dramatic effect on flow stability. It was shown by Sahu & Govindarajan (2005) that a pipe with any non-zero wall divergence has a finite critical Reynolds number. Such flows have not been studied using a global approach before, to our knowledge. This motivates us to study the effect of change in geometry in channel flows. The first change in geometry we consider is wall divergence and this is discussed in chapter 3.

Divergence and convergence have opposite stability characteristics and it will be interesting to study the flow through a channel with a series of alternating convergence and divergence. Such geometries are known to have smaller critical Reynolds number compared to a straight channel and hence are widely used in heat exchangers.

Wall jets have many industrial applications especially in heat and mass transfer. The applications depend on the parameters under which it will remain laminar or turbulent and hence it is important to understand its stability characteristics. This flow, whose critical Reynolds number is very small, has been studied using local stability approaches. We study this using a global stability approach, and discuss it in chapter 5.

CHAPTER 2

GLOBAL STABILITY ANALYSIS

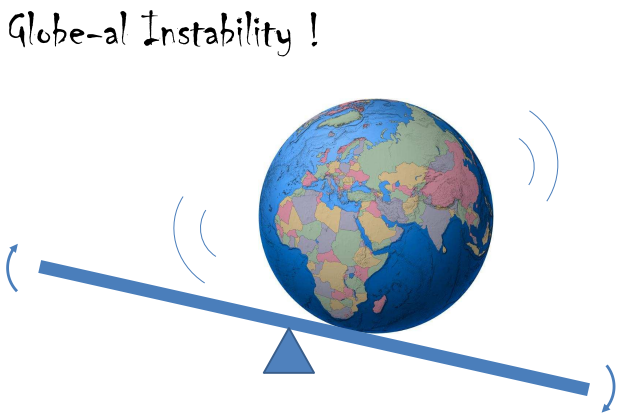

This chapter introduces the global stability approach and the need for such an approach to study the stability of non-parallel flows. We first introduce the two commonly used approximations which result in a problem solvable locally at one stream-wise location. These are the parallel flow assumption and the weakly non-parallel assumption. Some applications of each are described. Then we introduce strongly non-parallel flows and the global stability analysis with a few examples. The formulation of the problem and the numerical discretization schemes used in the present work are discussed next. This is followed by the method of solving the problem numerically, the techniques used and the validation.

2.1 Introduction

A flow can be defined completely by the functional dependence of the flow quantities on the three co-ordindate directions, x, y, z and time t. Quantities such as the velocity field, pressure, temperature, density, viscosity, etc. are required for the complete flow description. For our purposes, flows can be classified in two ways, based on their dependence on time and space. First, they can be steady or unsteady, based on their time

dependence. An unsteady flow varies with time, requires the flow variables expressed at every time instant for a complete description, and is beyond the scope of this thesis. A steady flow is independent of time. The second type of classification is based on the spatial dependence of the flow quantities. Under this classification flows can be parallel or non-parallel. A parallel flow is one whose flow quantities depend only on one direction, usually a cross-flow direction. Common examples are fully developed pipe flow and channel flow. Here, the flow velocity is described as a function of the wall-normal co-ordinate alone. Most other shear flows however are spatially developing, where the flow quantities change from one stream-wise location to the next. Examples of non-parallel flows are wakes, jets, boundary layers, free shear layers, flow behind a backward facing step, separated flows and flow through complex geometries. So strictly parallel flows in real-life situations are very few. Even in the case of a straight channel or pipe, the flow is often not fully developed. High Reynolds number flows have a very long entry region where the flow quantities vary significantly with distance, and it can be classified as a non-parallel flow. In fact the entire length of the pipe or channel may be part of this 'entry region'. A non-parallel flow depends on more than one spatial co-ordinate and it can be two-dimensional (2D) or three-dimensional (3D).

Under special circumstances, the variation of the flow quantity will be mild from station to station and these flows will be classified as weakly non-parallel flows as the non-parallel effects are 'weak'. A flat plate boundary layer at high Reynolds numbers and flow through diverging channels at small angles of divergence are common examples of weakly non-parallel flows. Also many flows whose laminar profiles obey self-similarity such as wakes and jets are assumed to exhibit only weak non-parallelism at very high Reynolds numbers.

The classifications discussed above, based on time and space, are independent of each other. A steady flow can be parallel or non-parallel, whereas a non-parallel flow can be steady or unsteady.

2.2 Linear Stability Theory

An incompressible flow, steady or unsteady, parallel or non-parallel, can be defined by the Navier-Stokes equations and continuity equation, given below.

$$\frac{\partial u}{\partial t} + u\frac{\partial u}{\partial x} + v\frac{\partial u}{\partial y} + w\frac{\partial u}{\partial z} = \frac{-1}{\rho}\frac{\partial p}{\partial x} + \frac{1}{Re}(\frac{\partial^2 u}{\partial x^2} + \frac{\partial^2 u}{\partial y^2} + \frac{\partial^2 u}{\partial z^2}). \tag{2.1}$$

$$\frac{\partial v}{\partial t} + u\frac{\partial v}{\partial x} + v\frac{\partial v}{\partial y} + w\frac{\partial v}{\partial z} = \frac{-1}{\rho}\frac{\partial p}{\partial y} + \frac{1}{Re}(\frac{\partial^2 v}{\partial x^2} + \frac{\partial^2 v}{\partial y^2} + \frac{\partial^2 v}{\partial z^2}). \tag{2.2}$$

$$\frac{\partial w}{\partial t} + u\frac{\partial w}{\partial x} + v\frac{\partial w}{\partial y} + w\frac{\partial w}{\partial z} = \frac{-1}{\rho}\frac{\partial p}{\partial z} + \frac{1}{Re}(\frac{\partial^2 w}{\partial x^2} + \frac{\partial^2 w}{\partial y^2} + \frac{\partial^2 w}{\partial z^2}). \tag{2.3}$$

$$\frac{\partial u}{\partial x} + \frac{\partial v}{\partial y} + \frac{\partial w}{\partial z} = 0. \tag{2.4}$$

Here x, y, z are the stream-wise, cross-stream and span-wise directions of the flow respectively, u, v, w are the respective velocity components in those directions, p is the pressure, ρ is the density, t is the time and Re is the Reynolds number. This set of equations coupled with suitable boundary conditions needs to be solved to define the flow field for a given situation. Dropping the time derivatives, we may obtain steady solutions satisfying the above equation, and certain classes of boundary conditions. These solutions are termed as 'base flow'. We distinguish the term 'base flow' from 'mean flow', although the two are often used interchangeably in this context. A base flow satisfies the steady Navier-Stokes equations but a mean flow may not, since it is merely the average of many realizations of the unsteady equations. The stability characteristics of the base flow are determined by adding a time and space perturbation , and tracking the perturbations in time and space to check if they grow or decay. The growth and decay of the perturbation defines the instability and stability of the base state, respectively.

Flows studied in this work are two-dimensional (2D) in nature and are defined by $W = 0$ and $\partial(U, V)/\partial z$. The concepts of stability are best explained using 2D base flows. Their extension to 3D base flows is straightforward. Also, we confine ourselves to the addition of 2D perturbations. 3D perturbations can cause qualitatively different instabilities and are much richer.

A flow quantity can be expressed, for example, as

$$u = U + \hat{u}, \quad v = V + \hat{v}, \quad p = P + \hat{p}, \tag{2.5}$$

where the uppercase letters stand for the base flow and the quantities with a hat (ˆ) indicate the perturbations. Substituting equation 2.5 in equations 2.1, 2.2 and 2.4, neglecting non-linear terms in the perturbation, and subtracting out the base flow equation, we get the evolution equations for the perturbations as,

$$\frac{\partial \hat{u}}{\partial t} + U\frac{\partial \hat{u}}{\partial x} + \hat{u}\frac{\partial U}{\partial x} + V\frac{\partial \hat{u}}{\partial y} + \hat{v}\frac{\partial U}{\partial y} = \frac{-1}{\rho}\frac{\partial \hat{p}}{\partial x} + \frac{1}{Re}(\frac{\partial^2 \hat{u}}{\partial x^2} + \frac{\partial^2 \hat{u}}{\partial y^2}). \tag{2.6}$$

$$\frac{\partial \hat{v}}{\partial t} + U\frac{\partial \hat{v}}{\partial x} + \hat{u}\frac{\partial V}{\partial x} + V\frac{\partial \hat{v}}{\partial y} + \hat{v}\frac{\partial V}{\partial y} = \frac{-1}{\rho}\frac{\partial \hat{p}}{\partial y} + \frac{1}{Re}(\frac{\partial^2 \hat{v}}{\partial x^2} + \frac{\partial^2 \hat{v}}{\partial y^2}). \tag{2.7}$$

$$\frac{\partial \hat{u}}{\partial x} + \frac{\partial \hat{v}}{\partial y} = 0. \tag{2.8}$$

This widely used approach is referred to linear stability theory (LST). As the transition to turbulence is characterized by instability followed by rapid non-linearization in many shear flows, researchers criticize the use of LST, see for example Waleffe (1995), as it would at best be able to give information only about the initial stages of transition. However an LST study is crucial in many flow situations and gives many important pointers about the initial stages of transition, signatures of which are often clearly visible even in fully developed turbulence. Besides this, linearly stable flow can undergo large transient growth and reach a completely different state. Alternatively, nonlinear instability could be the first to occur, creating a 'bypass' route to transition to turbulence. A remarkable success of LST is the accurate prediction of the critical Rayleigh number of 1708 for a Rayleigh-Benard flow. Its failure to match with experimental data for a plane Poiseuille flow has been explained using non-modal stability theory, see for example Schmid (2007).

We are specifically interested in understanding the initial stages of transition in flows where LST is among the most significant phenomena taking the flow towards turbulence. In fact, a major portion of this thesis is devoted to channel flow, where a change in geometry changes the dominant transition mechanism from one of transient growth to one of exponential and, a non-exponential, but still modal, spatial growth. Our question is, what triggers instability and what are the parameters involved? Henningson (1996) has showed that the nonlinear terms of the disturbance equation are conservative and if the energy of the disturbance has to grow, it has to be through a 'linear process only', thus supporting LST. Note that this observation is strictly true for a parallel flow only, since an assumption is made about the spatial periodicity of disturbance. It is nevertheless instructive about the importance of linear terms. To quote him, "The disturbance energy produced by linear mechanisms is the only disturbance energy available and in particular that this implies that the disturbance energy produced by transient mechanisms in subcritical transition cause the total increase of E (energy) during the transition process." This can be understood by considering the evolution equation for the kinetic disturbance

energy, see for example Schmid & Henningson (2001),

$$u_i\frac{\partial u_i}{\partial t} = -u_iu_j\frac{\partial U_i}{\partial x_j} - \frac{1}{Re}\frac{\partial u_i}{\partial x_j}\frac{\partial u_i}{\partial x_j} + \frac{\partial}{\partial x_j}\left[-\frac{1}{2}u_iu_iU_j - \frac{1}{2}u_iu_iu_j - u_ip\delta_{ij} + \frac{1}{Re}u_i\frac{\partial u_i}{\partial x_j}\right]. \tag{2.9}$$

This equation is obtained by substituting equation 2.5 in equations 2.1-2.3 and expressing them in the Einstein notation, multiplying them with u_i. Now, the left hand side is the rate of change of the kinetic energy of the disturbance, E. Remember that the non-linear terms are retained. We now assume that the disturbances are localized or spatially periodic. This assumption many not hold true for a non-parallel flow. Integrating the equation over a control volume V, and using Gauss's theorem the derivative terms drop out, giving,

$$\frac{dE_V}{dt} = -\int u_iu_j\frac{\partial U_i}{\partial x_j}dV - \frac{1}{Re}\int\frac{\partial u_i}{\partial x_j}\frac{\partial u_i}{\partial x_j}dV. \tag{2.10}$$

This equation is called as the Reynolds-Orr equation. We can see here that the terms remaining in the right hand side are obtained from the linear terms of the original equation and the terms obtained from the non-linear terms of the original equation have dropped out. This equation says that the kinetic energy of the disturbance grows purely by the linear terms and non-linear terms do not contribute to the energy growth.

2.3 Stability of Parallel Flows

Considering 2D perturbations allows us to express the disturbance in terms of the stream-function ϕ which automatically satisfies the continuity equation. Eliminating pressure between the equations 2.6 and 2.7, we get the equation which determines the evolution of perturbations as,

$$\left\{\left[U\frac{\partial}{\partial x} + V\frac{\partial}{\partial y}\right]\nabla^2 + \left[\frac{\partial^2 V}{\partial x\partial y} - \frac{\partial^2 U}{\partial y^2}\right]\frac{\partial}{\partial x} + \left[\frac{\partial^2 U}{\partial x\partial y} - \frac{\partial^2 V}{\partial x^2}\right]\frac{\partial}{\partial y} - \frac{1}{Re}\nabla^4\right\}\phi = \frac{\partial}{\partial t}\nabla^2\phi. \tag{2.11}$$

Here, $\hat{u}$ and $\hat{v}$ are replaced with $\partial\phi/\partial y$ and $-\partial\phi/\partial x$ respectively, $\nabla^2 = (\partial^2/\partial x^2 + \partial^2/\partial y^2)$. This perturbation equation is a partial differential equation. Solving this equation numerically is difficult and time-consuming. A few further simplifications are possible based on the type of flow considered and this leads to a classification based on the different stability approaches, as discussed below.

As its name suggests this method is applicable for strictly parallel flows. Over the decades non-parallel flows have however often been studied using this approach. When the stream-wise variation is slow, as in many high Reynolds number shear flows, the idea is that the flow may be treated as being locally parallel. As the steady base flow depends only on the wall-normal direction (y) and is independent of the stream-wise direction (x) and time t, the disturbance can be Fourier transformed in the independent co-ordinates as follows,

$$\phi(x, y, t) = \phi(y)e^{\iota(\alpha x - \omega t)}. \tag{2.12}$$

Here, α is the wavenumber in x and ω is the frequency. Depending on whether we choose a complex α or complex ω, we perform a spatial or temporal stability analysis, respectively. The imaginary part of α and ω will give information about the spatial and temporal growth/decay rate of the disturbance, respectively. Assuming a complex ω and real α in equation 2.12, and substituting it in equation 2.11, we get an ordinary differential eigenvalue problem for ω as,

$$[(U - c)(D^2 - \alpha^2) - U'']\phi = \frac{1}{i\alpha Re}[D^2 - \alpha^2]^2\phi. \tag{2.13}$$

Here, the eigenvalue $c = \omega/\alpha$ is the phase velocity of the disturbance, $D = \partial/\partial y$ and the prime denotes differentiation with respect to y. In a temporal framework, the equation is solved for the eigenvalue c by supplying a real α and Re. In general, the eigenvalue obtained is complex, and a plot of the frequency ω_r versus the growth rate ω_i is called the frequency spectrum. A sample spectrum obtained for a plane Poiseuille flow at a Reynolds number of 5770 and α=1.02 is shown in figure 2.1. As we can see from the figure, this flow is stable for this α as all the eigenvalues have a negative decay rate ω_i, meaning the disturbances decay exponentially in time. Also note that this flow is near-neutral at this Reynolds number. A small increase in Reynolds number, to 5772.3 will push this mode towards the unstable half plane to exhibit exponential instability with a growth rate of ω_i.

The equation discussed above is the famous Orr-Sommerfeld equation, derived independently in the beginning of the 20^{th} century by the Irish mathematician William McFadden Orr and the German theoretical physicist Arnold Johannes Wilhelm Sommerfeld. Soon thereafter, many people developed methods for approximate solutions of this equation using expansion methods, a discussion of which is given in Drazin & Reid (1981). Tollmien (1929) first solved the Orr-Sommerfeld equation for the Blasius

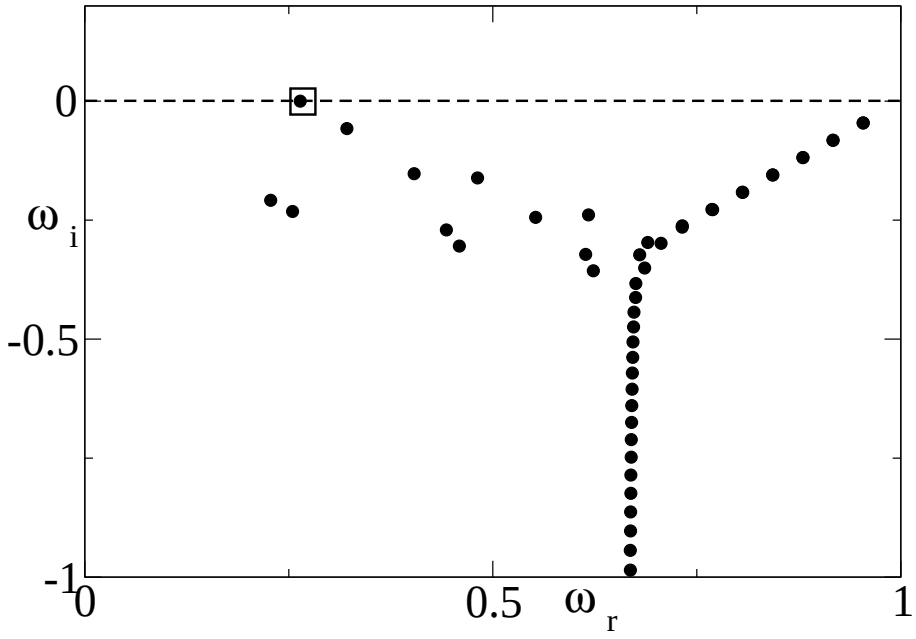

Figure 2.1: Spectrum obtained by solving Orr-Sommerfeld equation at $Re = 5770$ with $\alpha = 1.02$ for a plane Poiseuille flow. As can be seen, this flow is near-neutral in that one eigenvalue, shown in the box, is on the verge of moving into the unstable half plane ($\omega_i > 0$).

boundary layer and obtained a neutral curve. Most of the earlier literature on hydrodynamic stability considers very simple flow configurations like plane Poiseuille flow and plane Couette flow. The reason for this is that stability studies need information on the base flow state and it is possible to get the base state information analytically for these flows. Even though this method is restricted to strictly parallel flows, many researchers have applied this approach to study flows which evolve slowly downstream and were often able to get reasonable agreement with experiments. But it has to be noted that this agreement is case dependent and does not hold good for a variety of flow geometries. Hence, a different approach was evolved to study the stability of flows which vary downstream, as discussed below.

2.4 Stability of Weakly Non-parallel Flows

As mentioned before, the Orr-Sommerfeld equation neglects the stream-wise variation of the base flow as well as of the eigenfunction, and solves for the flow locally. This initially was thought to be the reason for mismatch between theory and experiments.

Hence many researchers were involved in developing theories which would incorporate non-parallel effects. They attacked it as a perturbation problem of the Orr-Sommerfeld equation or the resulting solutions, for example see Bottaro *et al.* (2003) in which the authors studied the stability of plane Couette flow with small variations in the base flow and found that this flow is destabilized even though the unperturbed flow is linearly stable for all Reynolds numbers. Gaster (2000) studied the effect of non-parallel terms in the stability of boundary layers and did not find drastic differences from the parallel flow results. The main difference between parallel and weakly non-parallel (WNP) theory is that parallel theory neglects all variations in x, whereas WNP retains terms upto order Re^{-1} in both mean and perturbations, and neglects higher orders. The disturbance thus takes the form,

$$\phi(x, y, t) = \phi(x, y)e^{\iota(\int \alpha(x)dx - \omega t)}. \tag{2.14}$$

Here, the wavenumber α accounts for the fast variations in x, and $\phi(x)$ is assumed to vary slowly with x, i.e. $\partial/\partial x \sim 1/Re$ and $\partial^2\phi/\partial x^2 \sim 0$. The Parabolized Stability Equations developed by Bertolotti *et al.* (1992) and Herbert (1997) and the Minimal Composite Theory developed by Govindarajan & Narasimha (1995), Govindarajan & Narasimha (1997) are examples of the WNP approach. This approach has been widely used in many flows like boundary layers - Gaster (1974), Bertolotti & Herbert (1991), Bertolotti *et al.* (1992), mixing layers - Monkewitz *et al.* (1993), Bhattacharya *et al.* (2006) and diverging pipes - Sahu & Govindarajan (2005). Since both parallel and weakly non-parallel approaches use the local velocity profiles, and other local quantities to determine the stability characteristics at a given stream-wise location, they are called local approaches.

2.5 Global Stability Analysis

The applications of the local approaches are limited to parallel and weakly non-parallel flows. A global approach is necessary when the stream-wise change of the flow is not negligible. More significantly, as will be shown later in the thesis, even in apparently weakly non-parallel flows which obey self-similarity, a global approach reveals results which are inaccessible to the local approaches. Even a flow between two parallel plates might exhibit non-parallelism in the region very close to inlet where the flow is not fully developed. In such flows, the disturbance is not Fourier transformable in x and is left as

an arbitrary function of x and y as,

$$\phi(x, y, t) = \phi(x, y)e^{-\iota\omega t}. \tag{2.15}$$

Substitution of 2.15 in equation 2.11 results in a partial differential eigenvalue problem in ω as,

$$\left\{ \left[U\frac{\partial}{\partial x} + V\frac{\partial}{\partial y} \right] \nabla^2 + \left[\frac{\partial^2 V}{\partial x \partial y} - \frac{\partial^2 U}{\partial y^2} \right] \frac{\partial}{\partial x} + \left[\frac{\partial^2 U}{\partial x \partial y} - \frac{\partial^2 V}{\partial x^2} \right] \frac{\partial}{\partial y} - \frac{1}{Re}\nabla^4 \right\} \phi = i\omega\nabla^2\phi. \tag{2.16}$$

The only difference between equations 2.11 and 2.16 is in the time derivative. This approach gives a global picture of the disturbance in terms of the eigenfunction as against a local approach. This approach can be termed as biglobal and triglobal based on whether the base flow considered is 2D or 3D, following Theofilis (2003). The present work, as mentioned before, is restricted to 2D flows. Extension to 3D base flows is straightforward but computationally very costly, as we will see later.

The first global study in the present context dates back to the work by Pierrehumbert (1986), where he studied two-dimensional disturbances in inviscid vortices. First calculations on viscous flows were reported by Jackson (1987), who studied the flow past variously shaped bodies and Zebib (1987), who studied flow past a circular cylinder. This approach slowly became popular with researchers in the study of free surface flows - Christodolou & Scriven (1988), rectangular ducts - Lee *et al.* (1989), Tatsumi & Yoshimura (1990) and boundary layers - Lin & Malik (1996), Lin & Malik (1997). But applying this method to large domains and at high Reynolds numbers was hindered by the large computational costs involved in solving the global stability equation. This is because the matrices emerging from the discretization process are large, dense and non-symmetric. All the above mentioned researchers (except Christodolou & Scriven (1988)) have used the traditional QR algorithm to solve the resulting matrix. The shortcoming, and sometimes the strength, of this algorithm is that it must compute all the eigenvalues. Since the instability in many shear flows is triggered by very few 'dangerous' modes, it would be computationally far more economical to calculate only those dangerous eigenvalues. Hence, many researchers were involved in developing efficient methods to attack the global stability problem by solving only for those eigenvalues which are physically relevant. Many algorithms like the Minimal Residual algorithm and the Conjugate Gradient method were tried. Since these methods were restricted to

symmetric, sparse matrices, researchers were involved in extending these methods to handle the non-symmetric generalized matrix systems arising out of the global stability approach, for example see Saad & Schultz (1986) and Christodolou & Scriven (1988). Iterative techniques like the Arnoldi iteration together with 'shift-invert strategy' and Lanczos iteration are explained in Saad (1980) and Nayar & Ortega (1993). Other examples are the low-dimensional Galerkin methods (see in Noack *et al.* (1993), Noack & Eckelmann (1994)) and Simultaneous (Subspace) Iteration technique used in Dijkstra *et al.* (1995). The techniques developed were used for a variety of fluid dynamical problems, like Rayleigh-Benard flow by Dijkstra *et al.* (1995), channel flow over riblets by Ehrenstein (1996), attachment-line boundary layer by Theofilis (1997), and the flow around a circular cylinder by Morzynski *et al.* (1999), where Krylov subspace methods were used to compute only a part of the physically relevant eigenvalues.

Since the beginning of the 21^{st} century, this global stability approach has been used to study a wider variety of complex flow geometries. Theofilis *et al.* (2000) studied 2D steady laminar separation bubble using WNP and DNS and got an excellent matching of the stability characteristics for both 2D and 3D. But by performing a global stability study, they show the existence of new instability modes which are inaccessible to either of the approaches. They propose that flow control studies, which normally consider the T-S waves and DNS frequencies, should consider the global mode frequencies to get better control. Barkley *et al.* (2002) performed a bi-global stability study on a backward facing step and found that the critical eigenmode is localized in the recirculation regions behind the step. Schmid & Henningson (2002) performed a global stability analysis on a falling liquid curtain. They show that while a single global mode cannot match the experimental results, an optimal superposition of many global modes was able to get very good agreement with the experimentally observed frequencies.

Theofilis *et al.* (2003) studied a swept attachment-line boundary layer flow using both DNS and global stability study and showed that the temporal and spatial solution of this problem can be obtained by a three-dimensional extension of Gortler-Hammerlin model at a lower computational cost. A very detailed review about global stability analysis is given in Theofilis (2003). In Theofilis *et al.* (2004), the authors studied the stability characteristics of four flow types using a global stability study. The global eigenvalue spectrum of a rectangular duct has been obtained and compared with that a plane Poiseuille flow. It was shown that the flow through a rectangular duct stabilizes in the limit of the geometry going towards a square duct. They also calculated the global spectrum of a

bounded Couette flow and found only stable modes. A lid driven cavity was also studied and critical Reynolds numbers obtained. This study was able to achieve excellent agreement with experimental results and was able to explain the error in the stability prediction of wall-bounded Couette flows based on the in-plane velocity. In Theofilis *et al.* (2005), the authors studied the global stability of separated profiles in three different flow configurations. In these flows, they show that the amplitude of the global modes is less in the separated region than in the wake region or shear layer region, depending on the problem under consideration. They also hint about the necessity to consider information from the global modes for flow control studies.

Mittal & Kumar (2003) studied the flow past a rotating cylinder and gave critical values for the occurrence of instability. Mittal & Singh (2005) used a finite element method to study vortex shedding behind cylinders at subcritical Reynolds numbers. They found that vortex shedding is possible at very low Reynolds numbers and were able to obtain a very good match between global stability results and numerical simulations. Ehrenstein & Gallaire (2005) studied the global stability characteristics of a flat plate boundary layer, which had hitherto been studied on a local basis. By an optimal superposition of the temporal global modes, the authors were able to simulate the convective nature of instability of the boundary layer. Chedevergne *et al.* (2006) studied solid rocket motors with fluid injection and found that the global eigen-spectrum is discrete for this case. The obtained global mode frequencies compare very well with experimental results and the authors propose that these global modes give insight about the thrust oscillations in solid rocket motors.

Gonzalez *et al.* (2007), for the first time, developed a finite element method with unstructured meshes for biglobal stability applications. Mittal & Kumar (2007) have developed a new approach for global stability in which the equations are written in a moving frame of reference, which travels with the disturbance. This approach thus determines the global convective instability of the modes at a particular instant, as against the large volume of temporal global instability studies. This method was used to study flow past a circular cylinder and excellent agreement was obtained with the direct numerical simulations. Alizard & Robinet (2007) performed a biglobal stability analysis on a flat plat boundary layer and obtained a very good match with the global stability results and the weakly non-parallel results. These authors were also able to show the convective nature of instability of the boundary layer using these global modes. They also study the transient amplifying behavior of the global modes and discuss them in

detail. Akervik *et al.* (2008) perform a global stability study on the flat plate boundary layer and calculate the maximum energy growth possible with these global modes using a reduced order model. They show that even with global modes, the optimal energy growth is not obtained with just a few least stable modes. This explains the need to consider few stable global modes also to capture the disturbance dynamics, which is very crucial in flow control, as we will see below.

In the later part of the last decade global modes have been predominantly used in flow control. To achieve better control, the disturbance modes considered should have good observability and good controllability. The best observable modes need not always be the best controllable modes. A balance should be achieved in terms of observability and controllability while selecting the modes for flow control. In active flow control, the disturbance energy is sensed at one stream-wise location and an appropriate response is actuated at another stream-wise location, generally an upstream location. In a local stability analysis, the modes at the sensor location and the actuator location are not connected to each other. Whereas, while using global modes, which extend throughout the domain including the sensor and actuator locations, the information is contained well within the global mode and hence these modes work much better in designing the desired control compared to local modes. The observability and controllability of global modes are determined by the maximum amplitude of the direct global mode and the adjoint global mode, respectively. An adjoint global mode is the global mode obtained by solving the adjoint global stability equation. A direct global mode is obtained by solving directly the global stability equation, which has been just referred to as a ‘global mode’ in the previous discussions.

While using global modes for control, the sensor is placed at the location where the direct global modes have their maximum amplitude and the actuators are placed where the adjoint global modes have their maximum amplitude. See Akervik *et al.* (2007) for a control study of a separated boundary layer in a cavity using global modes. In Henningson & Akervik (2008), the authors have developed reduced order models from the global modes, to perform flow control on three flow configurations, namely, a falling liquid sheet, Blasius boundary layer and a boundary layer flow along a shallow cavity. A reduced-order model does not consider all the global modes, but extracts the essential information from the global modes, converts them in a reduced form, and uses it to perform the flow control. Proper Orthogonal Decompositon (POD) is an example of a reduced order model, see Barbagallo *et al.* (2009) for example. This paper discusses in

detail about using global modes, POD modes and balanced POD modes for the control of a separated boundary layer. POD modes are best controllable whereas balanced POD modes are both observable and controllable. Marquet *et al.* (2009) studied a smoothed backward facing step using global modes and identified the non-normality associated with the governing equations in two forms - a lift-up non-normality resulting from the transport of the base flow by the perturbation and a convective non-normality resulting from the transport of the perturbations by the base flow. By computing the adjoint global modes, the authors were able to identify the optimal location of the sensors and actuators, in terms of both controllability and observability, for this flow.

In the previous sections, the term 'global stability analysis' has been used to refer to the partial differential eigenvalue problem where more than one direction is taken as the eigen-direction. In the weakly non-parallel framework, this term has often been used in a slightly different context, like in Monkewitz *et al.* (1993), Martin *et al.* (2006). Primarily to clarify the terminology, we briefly discuss the concepts of convective and absolute instability in order to understand the definition of global stability used here. These concepts were first developed in the early 1950's in the field of plasma physics; see Sturrock (1958), Bers (1983) for elaborate reviews. In contrast to the spatial or temporal analysis where we consider a complex α or ω respectively, a convective-absolute stability analysis considers both α and ω to be complex. This approach is a spatio-temporal analysis, giving information about the disturbance evolution in both space and time and hence this approach was widely called as the global stability analysis. Like the WNP, this approach too uses the (Wentzel-Kramers-Brillouin-Jeffreys) WKBJ approximation, details of which along with an elaborate review about the absolute/convective and local/global instabilities are available in Huerre & Monkewitz (1990).

In a convectively unstable but absolutely stable flow, a disturbance introduced at a localized region grows in time, but gets convected downstream, thus leaving the base flow at that location free of disturbance at a later time. Plane Poiseuille flow - Deissler (1987), circular jets and flat plate boundary layers - Gaster (1968), Gaster (1975), and mixing layers (for co-flow or small counter flow) - Huerre & Monkewitz (1985) are examples of convectively unstable flows. Convectively unstable flows are called 'globally stable' flows as the flow becomes free of the disturbance as it gets convected away and the flow eventually becomes stable.

In an absolutely unstable flow, a disturbance introduced at a given stream-wise station grows at that station, propagating both upstream and downstream, sometimes con-

taminating the entire flow field. Examples are bluff body wakes - Betchov & Criminale (1966), Pier (2008), mixing layers (for large counter flow) - Huerre & Monkewitz (1985), boundary layer on a rotating disk - Lingwood (1995), Pier (2007). It is important to remember that the presence of absolute instability does not necessarily imply a global instability. It has been shown in Monkewitz *et al.* (1993) that a region of absolute instability is a necessary, but not sufficient condition for global instability. This is because, if a flow has a 'pocket' or finite region of absolute instability, like a bluff body wake, then the flow can sustain temporally growing modes only inside that region. Elsewhere, the flow may only be convectively unstable. The review paper, Huerre & Monkewitz (1990) contains an appendix which lists the various convective and absolute stability studies done in wall bounded shear flows, jets, wakes and mixing layers.

Even though global stability studies as undertaken in the present work have been in existence since the 1980's, the term 'global stability' was used to represent this spatio-temporal absolute/convective approach till the early 21st century. The present definition of 'global stability' considering the stream-wise direction also as an eigen-direction (bi-global or tri-global) has gradually gained currency in the past decade. The first symposium exclusively on the global stability approach was conducted in 2001, with the increase in the number of researchers using this method. In fact, when I was a week-old student in JNC in 2005, my advisor attended one of these exclusive symposia on global stability, in Crete, Greece and that laid the foundation stone for my thesis!

2.6 Numerical Discretization

The art of expressing a continuous quantity defining a flow field at discrete points in the domain is called discretization. This is necessary because the equation governing the flow cannot be solved numerically at 'every point' in the domain, but can be solved at 'many points' in the domain. Different types of discretization methods exist, e.g. Finite Difference (FD), Finite Element method (FEM), Finite Volume method (FVM), Spectral method (SP). One of the commonly used spectral methods is the Fourier method which has trigonometric functions as the basis functions and an exponential convergence rate. But the drawback is that it can be used only for periodic functions. Chebyshev method uses Chebyshev polynomials as the basis functions. Legendre and other polynomials may also be used in spectral methods but they are not discussed here. The discretization scheme used in this work is Chebyshev-spectral collocation. Srinivasan *et al.* (1994)

has a very 'easy to understand' introduction to Chebyshev spectral method and how to use it to solve fluid dynamical problems. I learnt to use spectral methods from this paper and would recommend this reference for anyone new to SP discretization. When a differential equation is discretized, we get a discretized equation in matrix form. The discretization is explained first for an ODE which governs 1D flow and then for a PDE which governs a 2D flow.

2.6.1 1D discretization

Let u be the flow parameter of a 1D flow, governed by the equation $u'' - \alpha u = 0$. Here a prime denotes differentiation with respect to y. Let us discretize this equation with m grid points, with the value of u at each point expressed as $u_1, u_2, ..., u_{m-1}, u_m$. Now the equation has to be solved at each grid point and thus for m grid points, we will have m equations as,

$$\frac{d^2 u_i}{dy^2} = \alpha u_i, \qquad i = 1, 2, ...m.$$

If we define a differentiation matrix D to represent the discretized form of d/dy and D^2 for d/dy^2, the above set of equations can be written in matrix form as,

$$\begin{pmatrix} & & & & \\ & D^2 & & & \\ & & & & \\ & & & & \\ & & & & \end{pmatrix} \begin{pmatrix} u_1 \\ u_2 \\ . \\ . \\ u_m \end{pmatrix} = \begin{pmatrix} \alpha & 0 & 0 & 0 & 0 \\ 0 & \alpha & 0 & 0 & 0 \\ 0 & 0 & \alpha & 0 & 0 \\ 0 & 0 & 0 & \alpha & 0 \\ 0 & 0 & 0 & 0 & \alpha \end{pmatrix} \begin{pmatrix} u_1 \\ u_2 \\ . \\ . \\ u_m \end{pmatrix}.$$

The coefficients of the differentiation matrix D depend on the type of discretization used. FD methods are derived from Taylor's expansion and its accuracy depends upon the number of terms retained in the Taylor's expansion. For example, by considering upto the third term of the Taylor's expansion, we may derive a second order accurate FD formula as,

$$f'(x) = \frac{f(x+h) - f(x-h)}{2h}. \tag{2.17}$$

To improve the accuracy, one would retain more and more terms in the Taylor's expansion and get information from more grid points. Given m number of points, the best

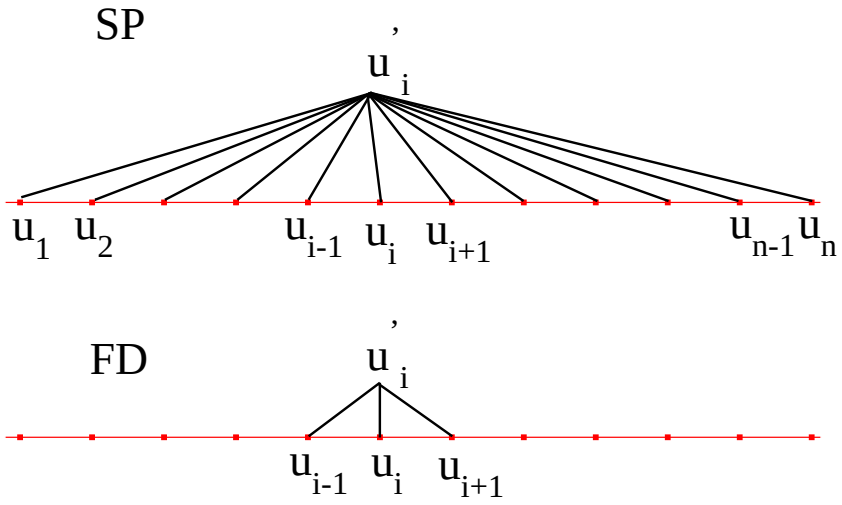

Figure 2.2: Schematic representation showing the dependence of the derivative at a point on the other grid points. As can be seen, SP methods have information from all the grid points, which gives high accuracy

one could do is to consider all the m points, and that is what SP method does. SP methods are known to exhibit higher levels of accuracy compared to FD methods. This is shown schematically in figure 2.2. But the price to pay for getting higher accuracy with SP methods is that the resulting matrix is dense. A sample D matrix from FD and SP discretizations will look like,

$$\begin{pmatrix} d_1 & d_{1+1} & 0 & 0 & 0 \\ d_{i-1} & d_i & d_{i+1} & 0 & 0 \\ 0 & d_{i-1} & d_i & d_{i+1} & 0 \\ 0 & 0 & d_{i-1} & d_i & d_{i+1} \\ 0 & 0 & 0 & d_{m-1} & d_m \end{pmatrix} \qquad \begin{pmatrix} d_{11} & d_{12} & d_{1.} & d_{1.} & d_{1m} \\ d_{21} & d_{22} & d_{2.} & d_{2.} & d_{2m} \\ d_{.1} & d_{.2} & d_{..} & d_{..} & d_{.m} \\ d_{.1} & d_{.2} & d_{..} & d_{..} & d_{.m} \\ d_{m1} & d_{m2} & d_{m.} & d_{m.} & d_{mm} \end{pmatrix}.$$

We can note that for a discretization with 'm' grid points, the D matrix is of size $m \times m$. In FD method, the D matrix is sparse (l-diagonal for a scheme which is usually accurate upto the order $(l-1)/2$). Occasionally higher-order accuracy can be obtained by clever algebraic manipulations for a given number of non-zero elements. For a given m this requires less memory for matrix storage and less computational time to operate on. On the contrary, the SP method gives a matrix where all the elements are non-zero, requiring large memory and computational time. But accurate results are obtained with

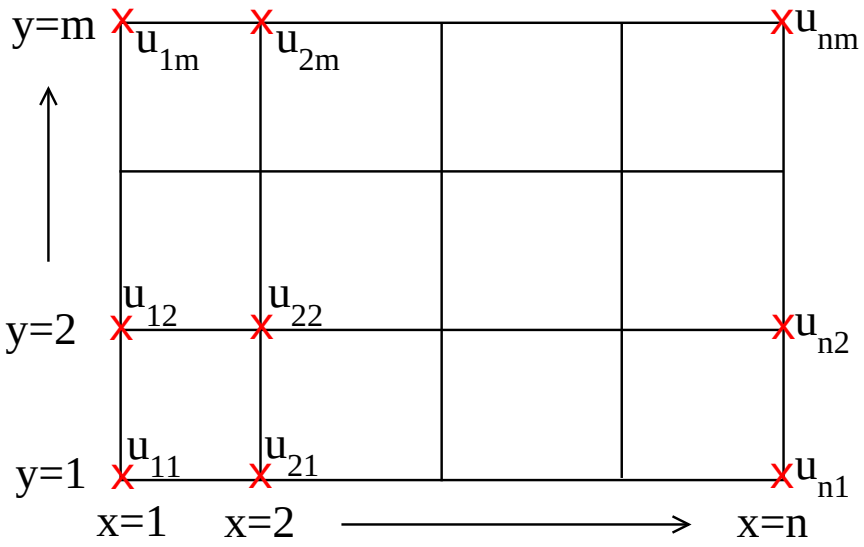

Figure 2.3: Nomenclature used for the grids locations in a 2D domain

less number of grid points in SP than would be required to get the same level of accuracy using FD.

In Chebyshev spectral discretization, the grid points are not equally spaced but are defined by a cosine function given as,

$$y_j = \cos\frac{j\pi}{m}, \qquad j = 1, 2, ..., m-1, m.$$

This defines the value of y between $+1$ and -1. A transformation can be enforced to make y vary between physically relevant values based on the problem. This will be explained in section 2.6.4. For $1 > y > -1$, the D matrix is defined as follows:

$$D(k,j) = \frac{c_k}{c_j}\frac{(-1)^{k+j}}{(y_k - y_j)} \qquad 1 \leq k, j \leq m, k \neq j \tag{2.18}$$

$$D(k,k) = -\frac{y_k}{2(1-{y_k}^2)} \qquad 2 \leq k \leq m-1 \tag{2.19}$$

$$D(0,0) = -D(m,m) = \frac{2m^2+1}{6} \tag{2.20}$$

with

$c_1 = c_m = 2, \qquad c_j = 1$ for $2 \leq j \leq m-1$

Higher derivatives are calculated by operating the D matrix onto itself, like $D^2 = D * D$

2.6.2 2D discretization - y

Now, let us consider the flow variable u in a 2D domain and choose a rectangular geometry in the $x-y$ plane for simplicity. Let us discretize this domain with n points in x and m points in y, as shown in figure 2.3. The value of u at each grid station is indicated as u_{ij}, where i corresponds to the x grid number and j corresponds to the y grid number, as shown in figure 2.3. Here, the total number of grid points will be nxm=nm. For demonstration, let us discretize the following equation,

$$\frac{\partial u}{\partial x}+\frac{\partial u}{\partial y}=0. \tag{2.21}$$

As before, the value of u at all the nm grid locations can be written as a column vector with the first m values corresponding to the first x location, the next m values for the next x location and so on, like,

$$\begin{pmatrix} u_{11} \\ u_{12} \\ . \\ . \\ u_{1m} \\ u_{21} \\ u_{22} \\ . \\ . \\ u_{2m} \\ . \\ . \\ . \\ . \\ u_{n1} \\ u_{n2} \\ . \\ . \\ u_{nm} \end{pmatrix}.$$

Here, each x location is indicated with a different color for ease of viewing. The discretization matrix in y (dy) can be defined using the formula 2.20 for each x location of size $m \times m$ and hence the D_y matrix for the 2D domain will take the form,

$$\begin{pmatrix} dy_{11} & dy_{12} & dy_{1.} & dy_{1m} & & & & & & & & & & & & \\ dy_{21} & dy_{22} & dy_{2.} & dy_{2m} & & & & & & & & & & & & \\ dy_{.1} & dy_{.2} & dy_{..} & dy_{.m} & & & & & & & & & & & & \\ dy_{.1} & dy_{.2} & dy_{..} & dy_{.m} & & & & & & & & & & & & \\ dy_{m1} & dy_{m2} & dy_{m.} & dy_{mm} & & & & & & & & & & & & \\ & & & & dy_{11} & dy_{12} & dy_{1.} & dy_{1m} & & & & & & & & \\ & & & & dy_{21} & dy_{22} & dy_{2.} & dy_{2m} & & & & & & & & \\ & & & & dy_{.1} & dy_{.2} & dy_{..} & dy_{.m} & & & & & & & & \\ & & & & dy_{.1} & dy_{.2} & dy_{..} & dy_{.m} & & & & & & & & \\ & & & & dy_{m1} & dy_{m2} & dy_{m.} & dy_{mm} & & & & & & & & \\ & & & & & & & & dy_{11} & dy_{12} & dy_{1.} & dy_{1m} & & & & \\ & & & & & & & & dy_{21} & dy_{22} & dy_{2.} & dy_{2m} & & & & \\ & & & & & & & & dy_{.1} & dy_{.2} & dy_{..} & dy_{.m} & & & & \\ & & & & & & & & dy_{.1} & dy_{.2} & dy_{..} & dy_{.m} & & & & \\ & & & & & & & & dy_{m1} & dy_{m2} & dy_{m.} & dy_{mm} & & & & \end{pmatrix} \begin{pmatrix} u_{11} \\ u_{12} \\ . \\ . \\ u_{1m} \\ u_{21} \\ u_{22} \\ . \\ . \\ u_{2m} \\ . \\ . \\ . \\ . \\ u_{n1} \\ u_{n2} \\ . \\ . \\ u_{nm} \end{pmatrix}.$$

2.6.3 2D discretization - x

The differentiation matrix in x (dx) can be defined using equation 2.20 for x defined between 1 and -1. Since the column vector is arranged in a particular manner, the differentiation matrix D_x of the 2D domain will take the form:

$$\begin{pmatrix} dx_{11} & 0 & 0 & 0 & 0 & dx_{12} & 0 & 0 & 0 & 0 & dx_{1m} & 0 & 0 & 0 & 0 \\ 0 & dx_{11} & 0 & 0 & 0 & 0 & dx_{12} & 0 & 0 & 0 & 0 & dx_{1m} & 0 & 0 & 0 \\ 0 & 0 & . & 0 & 0 & 0 & 0 & . & 0 & 0 & 0 & 0 & . & 0 & 0 \\ 0 & 0 & 0 & . & 0 & 0 & 0 & 0 & . & 0 & 0 & 0 & 0 & . & 0 \\ 0 & 0 & 0 & 0 & dx_{11} & 0 & 0 & 0 & 0 & dx_{12} & 0 & 0 & 0 & 0 & dx_{1m} \\ dx_{21} & 0 & 0 & 0 & 0 & dx_{22} & 0 & 0 & 0 & 0 & dx_{2m} & 0 & 0 & 0 & 0 \\ 0 & dx_{21} & 0 & 0 & 0 & 0 & dx_{22} & 0 & 0 & 0 & 0 & dx_{2m} & 0 & 0 & 0 \\ 0 & 0 & . & 0 & 0 & 0 & 0 & . & 0 & 0 & 0 & 0 & . & 0 & 0 \\ 0 & 0 & 0 & . & 0 & 0 & 0 & 0 & . & 0 & 0 & 0 & 0 & . & 0 \\ 0 & 0 & 0 & 0 & dx_{21} & 0 & 0 & 0 & 0 & dx_{22} & 0 & 0 & 0 & 0 & dx_{2m} \\ 0 & . & 0 & 0 & 0 & 0 & . & 0 & 0 & 0 & 0 & . & 0 & 0 & 0 \\ 0 & 0 & . & 0 & 0 & 0 & 0 & . & 0 & 0 & 0 & 0 & . & 0 & 0 \\ 0 & 0 & 0 & . & 0 & 0 & 0 & 0 & . & 0 & 0 & 0 & 0 & . & 0 \\ 0 & 0 & 0 & 0 & . & 0 & 0 & 0 & 0 & . & 0 & 0 & 0 & 0 & . \\ dx_{n1} & 0 & 0 & 0 & 0 & dx_{n2} & 0 & 0 & 0 & 0 & dx_{nm} & 0 & 0 & 0 & 0 \\ 0 & dx_{n1} & 0 & 0 & 0 & 0 & dx_{n2} & 0 & 0 & 0 & 0 & dx_{nm} & 0 & 0 & 0 \\ 0 & 0 & . & 0 & 0 & 0 & 0 & . & 0 & 0 & 0 & 0 & . & 0 & 0 \\ 0 & 0 & 0 & . & 0 & 0 & 0 & 0 & . & 0 & 0 & 0 & 0 & . & 0 \\ 0 & 0 & 0 & 0 & dx_{n1} & 0 & 0 & 0 & 0 & dx_{n2} & 0 & 0 & 0 & 0 & dx_{nm} \end{pmatrix} \begin{pmatrix} u_{11} \\ u_{12} \\ . \\ . \\ u_{1m} \\ u_{21} \\ u_{22} \\ . \\ . \\ u_{2m} \\ . \\ . \\ . \\ . \\ u_{n1} \\ u_{n2} \\ . \\ . \\ u_{nm} \end{pmatrix}.$$

As discussed before, calculation of higher order derivatives is straightforward once we have the basic D_x and D_y matrices.

As mentioned before, extension to a 3D basic flow is straightforward but it will become too large a matrix. In addition to the above performed discretization, if we have

p points in the third direction, then the leading dimension of the differentiation matrices in all the three directions, D_x, D_y, D_z will be $n \times m \times p$.

2.6.4 Co-ordinate Transformation and Grid Stretching

To be remembered is the fact that these matrices are derived for $1 > x > -1$ and $1 > y > -1$ (Note that x(1)=1 and x(n)=-1; y(1)=1 and y(m)=-1). To apply this method to any real world application, say x going from 0 to some length L, we do the following transformation: Let x be the set of spectral collocation points extending between 1 and -1 and x_{real} be the real x co-ordinate in the physical system. Then,

$$x_{real} = (x * (-0.5) + 0.5) * L. \tag{2.22}$$

Then, the derivative matrix in the physical space can be obtained by the transform,

$$Dx_{real} = Dx/(-0.5)/L. \tag{2.23}$$

Here, $\frac{1}{-0.5 * L}$ is called the Jacobian of transformation. Similar transformation can be done in the y co-ordinate also from the spectral space to the real space, using the appropriate Jacobian of transformation.

It is worth mentioning here about yet another Jacobian which could arise in the derivative matrices, namely the Jacobian of stretching. The collocation points obtained from Chebyshev method are not uniformly spaced but are distributed according to the cosine function. This clusters the grid points close to the start and end of the co-ordinate direction. In bounded flows like a channel flow or pipe flow, this type of grid clustering close the wall in the y direction is very advantageous, as the gradients of the flow are very close to the wall and a clustered grid in this region is necessary to capture these steep gradients. Whereas in unbounded or semi-bounded flows, like in jets, wakes and boundary layers, clustering of the grid points in this fashion is not desirable. In boundary layers it is desirable to have the clustering close to the wall region, whereas for wakes and jets we need more clustering around the center region. Similarly, in the x direction, Chebyshev discretization clusters the grid close to the inlet and exit of the domain, which is not desirable. Depending on the flow configuration, we could use a suitable stretching to cluster the grids at a given region. We use the following stretching function, (see in

Govindarajan (2004)),

$$x_j = \frac{\mathrm{a}}{\sinh(\mathrm{b}x_0)}[\sinh((x_c - x_0)\mathrm{b}) + \sinh(\mathrm{b}x_0)], \tag{2.24}$$

$$x_0 = \frac{0.5}{\mathrm{b}} \log\left[\frac{(1 + (e^{\mathrm{b}} - 1)\mathrm{a})}{(1 + (e^{\text{-b}} - 1)\mathrm{a})}\right], \tag{2.25}$$

Here, x_c is the collocation point, a is the x location around which clustering, relative to the collocation points, is required, and b is the degree of clustering. The values of a and b can be fixed depending upon the flow configuration and the amount of clustering required. This can be used in both the directions to achieve a desired grid clustering. On account of this stretching function, there will be a Jacobian matrix multiplying the Dx and Dy matrices to account for the stretching. The values of the stretching coefficients, a and b, used for the different flow configurations are given in the appropriate sections.

2.6.5 Domain transformation

Many researchers follow the idea of domain transformation in which a complicated geometry is mapped onto a rectangular geometry for ease of computation and for the easy application of boundary conditions, Cebeci *et al.* (2005). An example of one of the domains studied in the present work is shown in figure 2.4, where the grids on the physical and computational domain are shown. This transformation from the physical $x-y$ plane to the computational $\zeta - \eta$ plane is achieved using the following formulae,

$$d\zeta = dx, \tag{2.26}$$

$$\eta = \frac{y}{h(x)}, \tag{2.27}$$

where, $h(x)$ is the local semi-height of the physical domain. For this transformation, we get the differentiation matrices in the physical $x - y$ domain as,

$$\frac{\partial}{\partial x} = \frac{\partial}{\partial \zeta} + \left(\frac{-\eta h'}{h}\right)\frac{\partial}{\partial \eta} \tag{2.28}$$

$$\frac{\partial}{\partial y} = \frac{1}{h}\frac{\partial}{\partial \eta}. \tag{2.29}$$

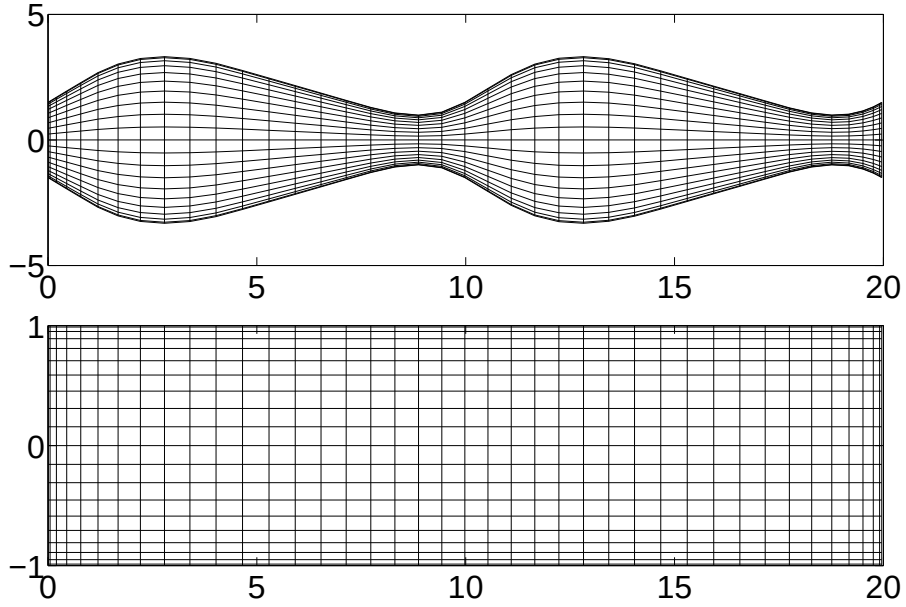

Figure 2.4: Grids on the physical domain and the computational domain

It can be noted that even though D_η and D_ζ matrices thus constructed are sparse, higher derivatives of these matrices are dense. A schematic representation of the density these matrices is shown in figure 2.5, where a blue dot represents a null element and a red star represents a non-zero element. The density of the colour red in the figure is directly proportional to the density of the matrix. As can be seen, the D_x, D_y and D_{yy} matrices are sparse, whereas the D_{xx} and D_{xy} matrices are dense. Thus, using spectral discretization in both the directions with co-ordinate transformation of the above kind will lead to the final A and B matrices being dense. This density of the matrices will restrict the type of solution method, as we will see in section 2.9.

2.7 Base flow calculation

Having discussed the various derivative terms in the global stability equation 2.16 and the ways to calculate them, we are left with the base flow terms in the equation. One important reason why global stability analysis did not come into existence much earlier than it actually did is the necessity to know the base flow accurately. It is well known that small errors in the base flow can produce huge errors in the growth or decay rates. We will see in later chapters how sensitive the stability is to small changes in the base flow.

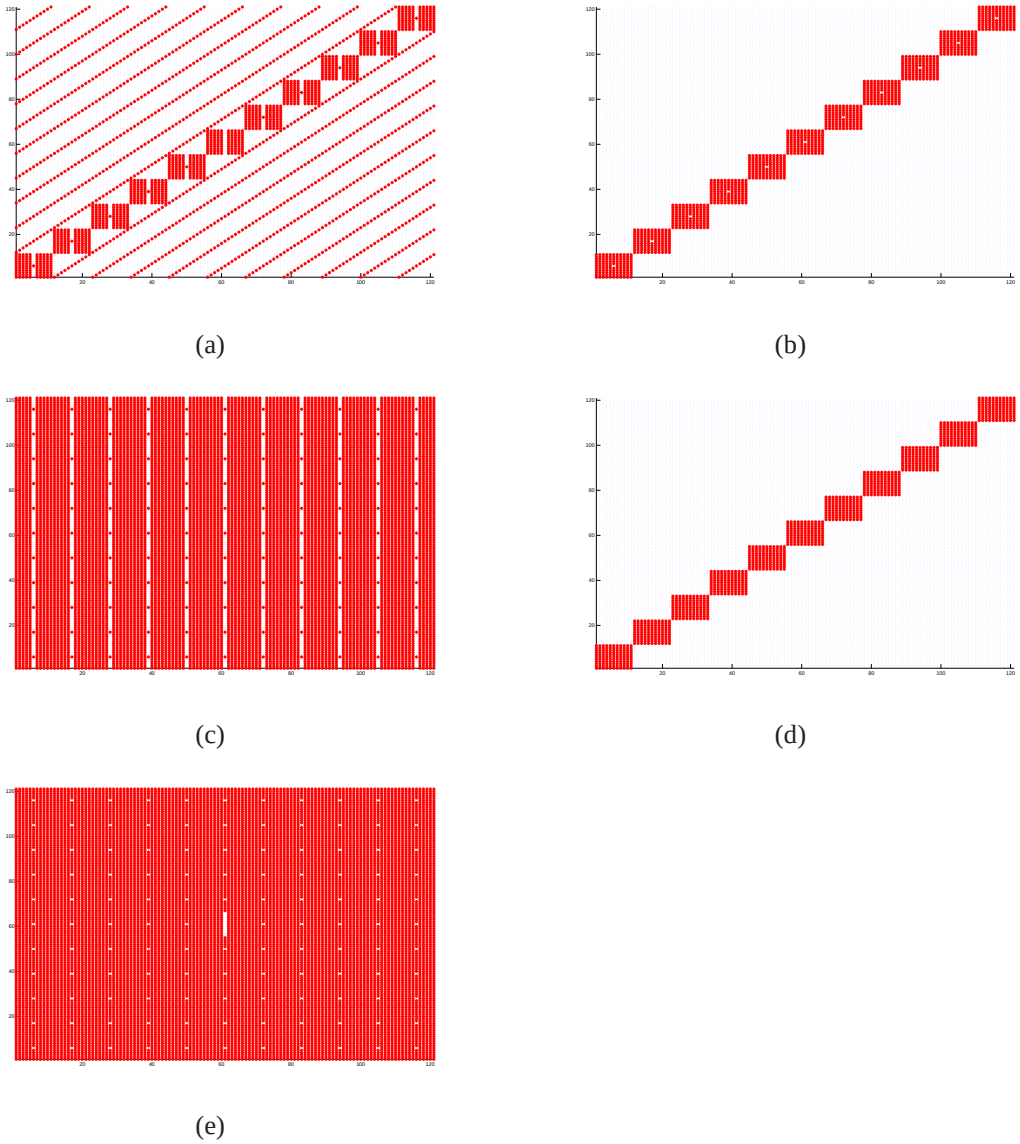

Figure 2.5: Schematic representation showing the density of the matrices (a) D_x (b) D_y (c) D_{xx} (d) D_{yy} (e) D_{xy}. The blue dots represent zero entry and red stars represent non-zero elements.

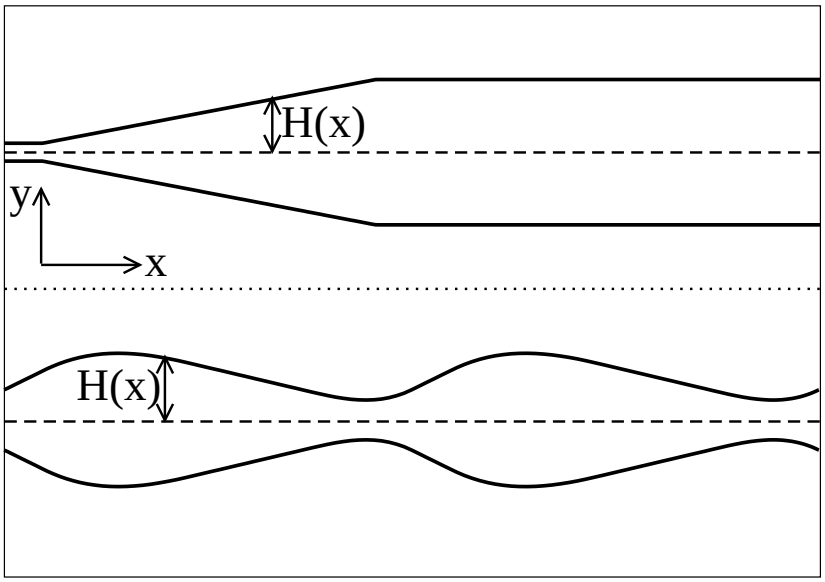

Figure 2.6: Typical geometries handled by the base flow code in the present work. Top: A finite diverging channel. Bottom: A converging-diverging channel. The stream-wise boundary conditions differ in the two cases.

The base flow, especially in a complex geometry, is often not straightforward to obtain and we need huge computational resources to calculate it. Even in a weakly non-parallel flow, and even with a very efficient numerical technique, it is remarkable that obtaining the base flow can be the slowest step in the proceedings. This is one of the shortcomings of the global stability analysis, where studying really complex flow geometries becomes problematic. In the present work, the base flow profiles are obtained from a self-similar solution, if it exists, or by solving the Navier-Stokes equations directly, using a code developed by Sahu (2003). I thank him for sharing this code with us, which has been used here both for a channel with a finite diverging region, discussed in chapter 3, and a converging-diverging channel, discussed in chapter 4. Most of the base flow calculations for the diverging channel flow for the required parameters are made by him. A few modifications to the converging-diverging channel flow code are made by him to suit the different parametric requirements. A comparison of the two types of geometries handled by this code is given in figure 2.6. The details of the numerical method are given below.

The steady two-dimensional Navier-Stokes equations are solved in the streamfunction-vorticity formulation. This can become very time consuming, so a full multigrid technique is used to accelerate the convergence, and a fast parallel solver is incorporated, details of which are available in Venkatesh *et al.* (2006). The governing dimensionless

equations are

$$\frac{\partial \Omega}{\partial t} + (\vec{U}.\nabla)\Omega = \frac{1}{Re}\nabla^2\Omega \qquad \Omega = -\nabla^2\psi,$$

where $\vec{U}$ is the velocity vector, t is time, and Ω and ψ are the mean vorticity and stream-function respectively. The solution is facilitated by a transformation of coordinate, defined by $d\zeta = dx/H(x)$, and $\eta = y/H(x)$, where H is the local half-width (for both diverging channel and converging-diverging channel, as shown in figure 2.6). Since the geometries considered are top-down symmetric, the equations are solved only for half the domain. Symmetry boundary conditions $\psi = \Omega = V = \partial U/\partial y = 0$ are used at the centerline; no-slip and impermeability boundary conditions, $U = V = 0$, are imposed at the wall. There is also a set of boundaries studied which are not top-down symmetric, and the flow here is solved for over the entire domain. The boundary conditions for that case will be no-slip and no-penetration at both the walls. The stream-wise boundary conditions for the channel with a finite diverging region is Neumann at the inlet and exit. A parabolic flow is prescribed at the inlet. For the converging-diverging channel with periodic units in series, the equations are solved for just one periodic unit, with periodic boundary conditions at the inlet and the exit.

Except for the boundary conditions and the domain boundary, the solution procedure is the same for both the cases. We begin with a guess solution: usually a parabolic velocity profile at every stream-wise location, and march in psuedo-time until a steady-state solution is obtained. The vorticity distribution at each new time step is calculated adopting first-order accurate forward differencing in time and second-order accurate central differencing in space. This vorticity distribution is used to solve the Poisson equation for the streamfunction by a Jacobi iterative scheme. Numerical acceleration is achieved by a six level full-multigrid technique. The procedure is repeated until the cumulative change in vorticity reduces to below 10^{-8}. The grid sizes required for each case depend on the parameters under consideration and they are given in the relevant chapters.

The base flow is obtained on equally-spaced grid points while the stability analysis is performed on a spectral-spectral grid. Hence, the base flow obtained is interpolated onto the spectral-spectral grid using a cubic spline interpolation. This code, in addition to fitting a cubic spline between the given points, has a special feature of minimizing the length of the spline being fit, thus avoiding spurious oscillations of the curve. While cubic spline interpolation is performed at the interior grid points, linear interpolation is

used at the boundaries of the domain. The base flow thus obtained after interpolation is checked for spurious values and compared with the original (equi-distant) data, before proceeding further.

2.8 Boundary conditions

The global stability equation 2.16 is a generalized eigenvalue problem of the form $Ax = \lambda Bx$. So far, we have seen the techniques involved in calculating the A and B matrices. Before solving this eigenvalue problem, we need to enforce the boundary conditions in these matrices, as discussed below.

In addition to the above mentioned necessity to know the base flow accurately, there is yet another hurdle for the global stability approach, of not knowing the stream-wise boundary conditions for the disturbance. There are a few guidelines for the implementation of these boundary conditions, based on the flow configuration. In the wall-normal direction, no-slip and no-penetration boundary conditions are used in solid walls (like in channel flow); decaying boundary conditions are given in far field boundaries (like in wakes and boundary layers). In the stream-wise direction, the most commonly used are the periodic boundary conditions. The justification for their use is often not clear. It has been assumed that they are valid, particularly in periodic geometries. We shall see however, that a periodicity in geometry is not reason for expecting the same periodicity in the perturbations. In localized flows such as a separation bubbles and cavity flows, homogeneous Dirichlet boundary conditions are used because the disturbance is expected to be localized within the flow and that it is therefore valid to assume the incoming and outgoing flow to be free of disturbance. Inhomogeneous Neumann and Dirichlet boundary conditions are applied when some property of the disturbance is known before hand, like the frequency of the mode. A special type of Neumann boundary condition is the Robin boundary condition, in which the derivative of the disturbance is specified based on the wavenumber of the disturbance. This is expressed as

$$\frac{\partial u}{\partial x} = i\alpha u, \tag{2.30}$$

where α is the wavenumber. This boundary condition has its roots in the parallel stability approach, see equation 2.12. Equation 2.30 is just a restatement of equation 2.12. In fact, due to its nature, this boundary condition has played a major role in the validation of the

global stability code developed during my PhD, details of which are given in section 2.12. We shall find the limitations as well of this boundary conditions.

When the stream-wise dependence of the disturbance is not known a priori, use of any of the above mentioned boundary conditions are not valid. Homogeneous Neumann boundary conditions are used in such situations, which does not allow for any change in the stream-wise direction of the disturbance at the inlet and exit. Few researchers also propose to use the homogeneous second derivative conditions at the boundary, which would mean that the slope of the disturbance does not vary in x. But, we consider this also as a restrictive boundary condition, and use 'Extrapolated Boundary Condition' (EBC), see Theofilis (2003), as it is the least intrusive boundary condition. According to this, all disturbance quantities at the boundary are prescribed to be linear extrapolations of their values in the interior of the domain. For example, the flow quantity u at the inlet, say (1), is written as a linear function of the values at the next two grid locations $(2, 3)$ as,

$$u_1[x_3 - x_2] - u_2[x_3 - x_1] + u_3[x_2 - x_1] = 0. \tag{2.31}$$

Similarly, the value at the exit can be written as a linearly extrapolated function of the values prior to the exit. For most of the results presented in this thesis, EBC are used. For the sake of comparison, periodic and Robin boundary conditions are also used and this is mentioned then and there.

Once the boundary conditions are decided, they can be implemented by replacing a few rows of the operator matrices (A and B matrices). This is very clearly explained in Srinivasan *et al.* (1994). If the boundary conditions are homogeneous Dirichlet, then a common practice is to ignore (remove) the rows corresponding to this boundary conditions and solve for the remaining matrix. This will reduce the size of the matrix and hence the computational cost, to a certain extent.

2.9 Numerical Method

The numerical discretization using spectral method in both x and y along with the co-ordinate transformation results in generalized eigenvalue problem with dense non-symmetric matrices. But the final form of the matrices obtained depend on the type of discretization and transformation used, if any. For example, using FVM or FD in x and spectral in y will give a sparse matrix. In such cases, iterative solvers to solve

for only part of the eigenspectrum is very successful. One of the commonly used iterative solver is ARPACK (since 1996), which uses the iterative Arnoldi algorithm. There are also other eigenvalue solvers like LAPACK, SCALAPACK, EISPACK, LINPACK, UMFPACK, BiCGStab. The choice of the solver depends on the type of the matrix we get which again depends on the discretization scheme we use.

In the present work, we started working with the package LAPACK, which is a direct solver solving all the eigenvalues using QZ algorithm. Since this was a very time consuming process, we resorted to the iterative solver ARPACK, which solves only for few eigenvalues. In this, we used the 'shift-invert strategy', where the eigenvalues are solved in the vicinity of the 'shift' supplied. But for large matrices of the order used in this work, ARPACK was taking more time than LAPACK, against our expectation. This is because the iterative process is carried out through a series of matrix-vector multiplications. For a sparse matrix this operation is fast, giving faster convergence. But for a dense matrix, this matrix-vector multiplication is not very fast and ARPACK takes much longer than LAPACK, to calculate just a few eigenvalues. Thus, the use of ARPACK is not helpful for our work. A comparison of the spectra obtained using LAPACK and ARPACK for few eigenvalues with a 'shift' mentioned is shown in figure 2.7. Also, this being the first global stability study in the problems considered, the choice of shift and the number of eigenvalues to ask for is not straight-forward.

The use of LAPACK which is a direct solver to solve all the eigenvalues could be speeded up using the parallelized version of LAPACK, called SCALAPACK. But, this software does not have an inbuilt subroutine for non-symmetric matrices of the kind we get. Hence we resort to the longer, time consuming, computationally costlier way of solving the equation, using LAPACK.

One more point to note about the global stability equation (2.16) is that it employs complex variables. A complex system will have twice the memory requirement and a corresponding increase in the computational cost compared to a real system. We convert this complex system of equations into a real system by the transformation mentioned in Theofilis (2003). This is simply done by defining $\lambda = i\omega$, thus making A and B matrices real and solving for complex λ. This real system is solved using the inbuilt subroutine of LAPACK called dggev (formerly dgegv).

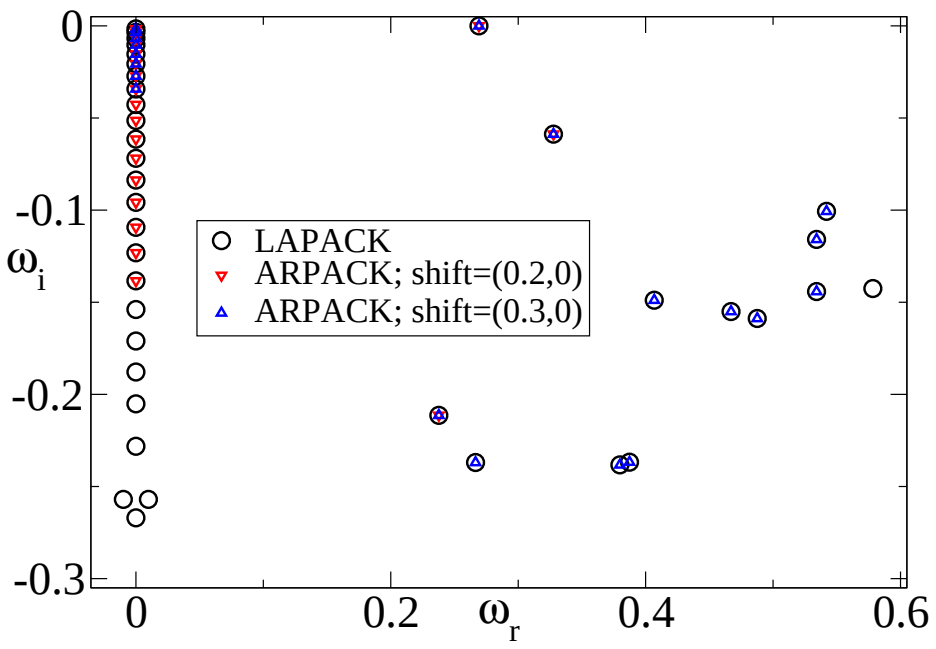

Figure 2.7: Comparison of the spectra obtained for a typical non-symmetric generalized dense matrix system, using LAPACK (entire spectrum) and ARPACK (for 20 eigenvalues in the vicinity of the shift provided). The values of the shift are given in the inset.

2.10 Issues with Global Stability Theory

With great increases in processor speed, RAM, processor memory, global stability analysis is being widely adopted to solve complex fluid dynamical problems. Even though this analysis is very good in solving complex problems, it has a few issues when it comes to implementation. They are listed as follows:

- A global stability study can be conducted on any complex 2D or 3D field, provided the base flow is known exactly. Obtaining the base flow for many complex flows is often not straight forward, and even when it is, requires a lot of computational effort.

- As mentioned before, the x boundary conditions depend on the physics governing the flow. For localized flows, the x boundary conditions are fairly straightforward whereas for many convectively unstable flows like the flat plate boundary layer, and other flow configurations the boundary conditions are still not very clear. Many researchers agree that if a sufficiently long enough domain is considered in the stream-wise direction, then the effect of the boundary conditions will not be

'felt' in the interior of the domain. In such a case, a homogeneous Dirichlet or Neumann boundary condition would be considered safe. But again to consider a very long domain, we need to consider many grid points, which in turn will increase the computational cost. Thus, the issue of x boundary conditions in a 'finite' domain is still very unclear for a majority of flows.

- Even though many iterative techniques which solve for very few physically relevant eigenvalues exist for global stability studies, usage of such techniques are restricted to a class of flows which do not require a co-ordinate transformation. In addition, if we use FD method in one direction to achieve a sparse matrix, then more number of points need to be considered to achieve good accuracy. A dense matrix is not a good candidate for the iterative algorithms. Thus global stability study in general requires high computational resources.

- The modes obtained from parallel analysis are limited by Howard's semi-circle theorem which states that the disturbance cannot move faster than or slower than the base flow velocity. This theorem has been used as a guideline to eliminate physically irrelevant modes in a system. This theorem is not necessarily valid for non-parallel flows. Hence it is difficult to pin down the physically relevant disturbance modes and eliminate the spurious modes. Even if we assume that the disturbances cannot propagate faster/slower than the maximum/minimum base flow speed respectively, there is no 'direct' method to estimate the disturbance wave speed. Time evolution of the mode (in a movie form) can give us quantitative information, but that is not easy to implement on all the modes calculated numerically.

2.11 Grid Sensitivity

As mentioned before, the size of the matrices obtained are big and hence the computational cost is huge. This limits the maximum grid size studied and hence might affect accuracy. A sample grid size used by many researchers studying global stability of different flows is given below. The grid sizes give a representative number and has to be fixed for each problem depending upon the domain and the flow characteristics.

Author	Flow	Method	Size
Ehrenstein *et al*.	Separated boundary layer	Chebyshev x Chebyshev	350x65
Ehrenstein *et al*.	Boundary layer	Chebyshev x Chebyshev	180x45
Casalis *et al*.	Solid rocket motor	Chebyshev x Chebyshev	120x120
Theofilis *et al*	Duct, Couette flow	Chebyshev x Chebyshev	72x40
Theofilis *et al*	Square lid driven cavity	Chebyshev x Chebyshev	48x48

In the present work, care has been taken to ensure grid insensitivity in each of the results presented. The grid size required and the grid sensitivity results are presented in each chapter, in the relevant subsections.

2.12 Validation

This is the section which took the longest duration of the entire code development phase. The code is written in Fortran language with a feature called 'dynamic memory allocation' which helps to handle really large memory requirements encountered with large size matrices. The idea is to allocate the required amount of memory for a variable until the values dependent on it are calculated. After the dependent values are calculated, the memory is freed so that it can be used for some other variable. With this, a large memory requirement program can be run efficiently with the available less computer memory.

For the purpose of validation, we consider one of the benchmark problems in hydrodynamic stability, the stability of a plane Poiseuille flow. The fully developed parabolic flow through a straight channel becomes linearly unstable at a Reynolds number (based on the channel half-width and centerline velocity) of 5772 for a disturbance of wavenumber $\alpha = 1.02$, see Orszag (1971). Since the present global stability formulation does not have a wavenumber in it, to compare with the parallel approach Orr-Sommerfeld results, we need to force a wavelike nature of the disturbance. It is worth noting that replacing $\phi(x) \sim e^{i\alpha x}$ in the global stability equation and forcing $V = 0$ and $dU/dx = 0$ (corresponding to a parallel flow), we get the Orr-Sommerfeld equation. For validation, we consider a 2D rectangular domain corresponding to a finite domain of the plane Poiseuille flow. The base flow is given as the fully developed parabolic profile of the

plane Poiseuille flow ($U = 1 - y^2, V = 0$). No-slip and no-penetration boundary conditions are forced at the top and bottom walls of the domain. The boundary conditions in the stream-wise direction are chosen as follows: to force a wavelike nature of the disturbance, we fix the non-dimensional length of the domain equal to the wavelength of the wave under consideration ($2\pi/\alpha$) and force periodic boundary conditions at inlet and exit. But the results obtained were not as expected. There was something more we need to do. One of the underlying assumptions of parallel approach is the wave-like nature of the disturbance with a wavenumber, say α. Even though a wave is periodic over one period of its wavelength, the boundary condition we had given will allow for any shape of the eigenfunction which is periodic over the prescribed length. We will thus not be restricted to Orr-Sommerfeld like modes. The only way to fix the disturbance with a single wavenumber is to encourage this behavior at the inlet and exit by applying Robin boundary conditions, stated as $d\phi/dx = i\alpha\phi$. It can thus be seen that this boundary condition has its roots from the parallel approach (see section 2.8).

As mentioned in later part of section 2.9, the global stability equation is made 'real' by solving for $i\omega$. But enforcing Robin boundary conditions will make the entire system of equations complex again. To avoid this, we supply a modified form of the Robin boundary condition as, $\frac{d^2\phi}{dx^2} = -\alpha^2\phi$ and $\frac{d^4\phi}{dx^4} = \alpha^4\phi$. Since the global stability equation is fourth order in x, we need to give four boundary conditions in x. The four boundary conditions used in this validation are,

(i) ϕ is periodic i.e. $\phi_1 = \phi_n$

(ii) $\frac{d^2\phi_1}{dx^2} = -\alpha^2\phi_1$

(iii) $\frac{d^2\phi_n}{dx^2} = -\alpha^2\phi_n$

(iv) $\frac{d^4\phi_n}{dx^4} = \alpha^4\phi_n$.

With this, we are able to reproduce the parallel results of Orszag (1971) on a plane channel flow. A sample spectrum obtained at a Reynolds number of 5772 with $\alpha = 1.02$ is shown in figure 2.8. Here also, we don't get an exact match with the entire spectrum of the Orr-Sommerfeld results, because the Robin boundary conditions will allow for higher harmonics of α over the same wavelength whereas the Orr-Sommerfeld results hold good for a single α. This is the reason we see some additional eigenvalues in the global approach. Nevertheless, we are able to get a good match for the least stable eigenmode. The structure of the eigenfunction is also matched with very good accuracy,

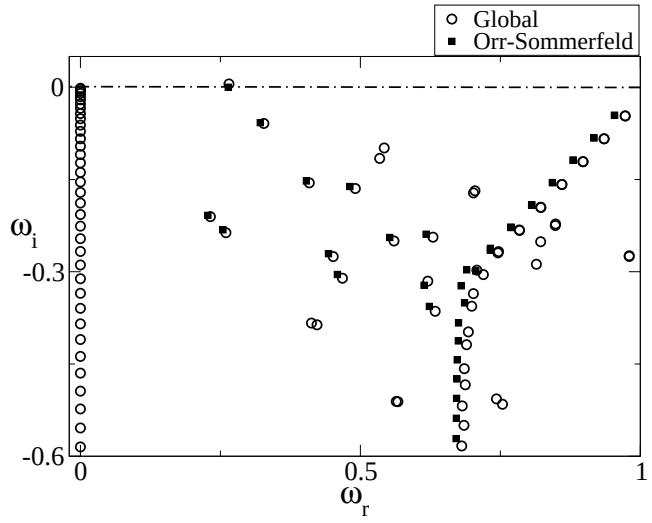

Figure 2.8: Comparison of spectra obtained using the Orr-Sommerfeld equation and the global stability equation for a plane Poiseuille flow at a Reynolds number of 5772, $\alpha = 1.02$. The x boundary conditions in global approach are Robin + periodic.

as shown in figure 2.9. We also get a value of critical Reynolds number (Re_{crit}) of 5772 for an α of 1.02, as shown in figure 2.10. Plotted here is the growth rate (ω_i) of the least stable mode versus the Reynolds number.

In addition to the above checks, the following checks were also done. Since each chapter deals with a different geometry, stretching function and co-ordinate transformation, the final differentiation matrices obtained are checked as follows: A known function of x or y is defined and the derivatives of the function are checked with the analytical values. For example, the fourth derivative of a function defined as y^4 is checked to be 24. Similar checks were done for x derivative too. In the cases where a similarity solution does not exist, the derivatives of the base flow obtained numerically and that obtained by the operation of the derivative matrices on the base flow are cross-checked.

This validates the code and the approach to the extent possible. In addition, we have also made sure that the results obtained are insensitive to the compiler used (f77, f95, gfortran, ifort) and the processor configuration (like precision, accuracy, processor speed, RAM, etc).

The reader will find certain sections of this thesis containing a lot of detail, for example the section on numerics. The objective is that a new student may use this thesis as an aid.

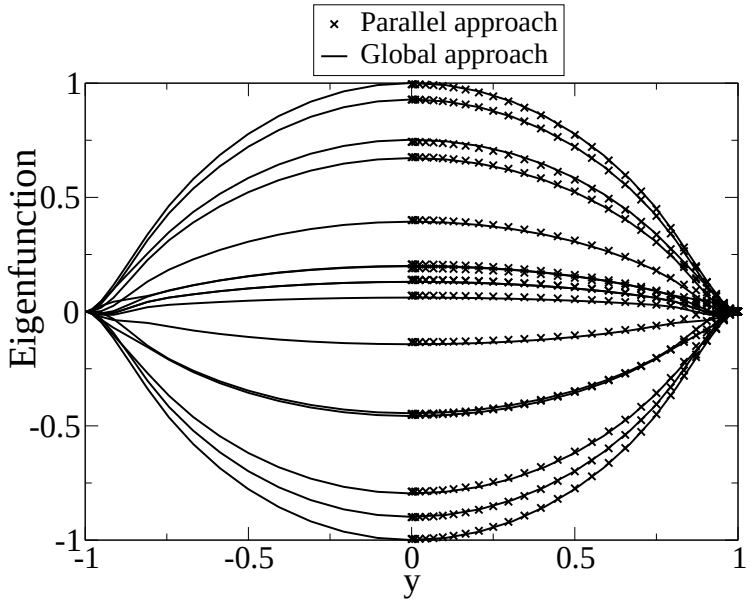

Figure 2.9: Comparison of the least stable eigenfunction shown in figure 2.8. Plotted here is the eigenfunction versus the wall-normal co-ordinate. The global equation is solved for full channel and parallel equation is solved for half channel. Each curve represents different x locations spanning over a wavelength of the wave.

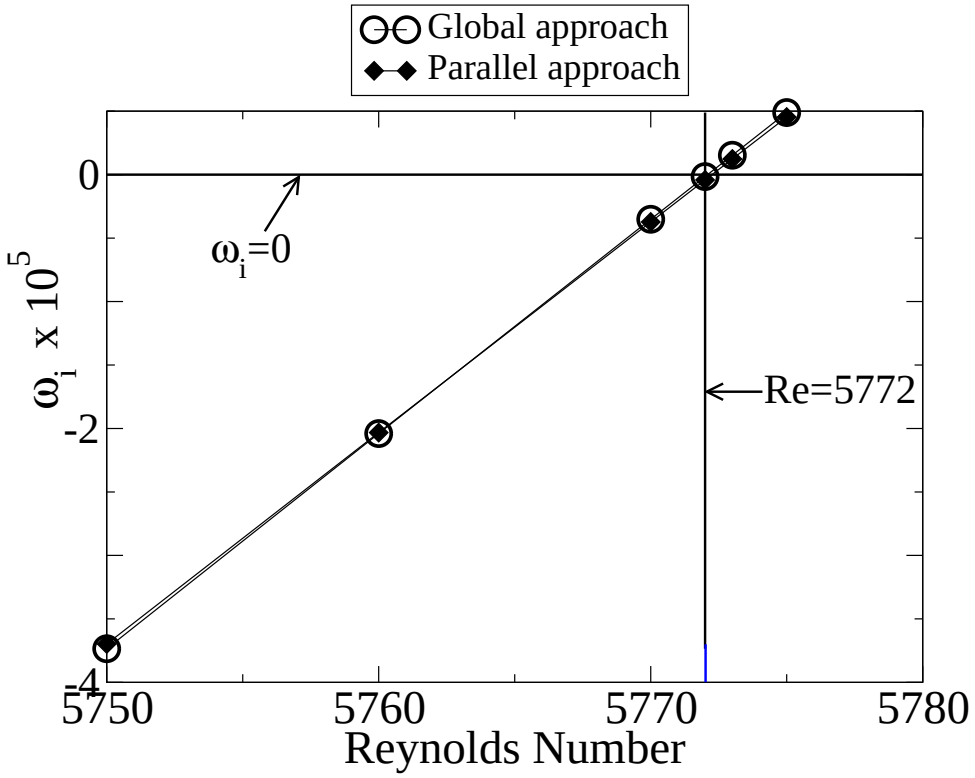

Figure 2.10: Graph of Reynolds number versus ω_i for plane Channel flow obtained from the global stability code with Robin boundary conditions. $\alpha = 1.02$. Only the least stable mode is shown, which is seen to cross the imaginary axis at a Reynolds number of 5772. The results obtained from the Orr-Sommerfeld equation are also shown for comparison.

CHAPTER 3

DIVERGING CHANNELS

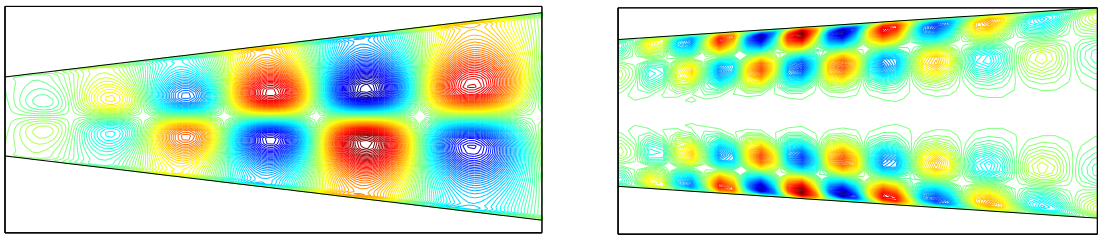

3.1 Introduction

In the previous chapter we saw that a plane Poiseuille flow is linearly stable upto a Reynolds number of 5772. But in a real life situation this flow becomes transitional at a Reynolds much lower than the critical Reynolds number. This is called subcritical transition. Many shear flows exhibit subcritical instability, classical examples being the Poiseuille flow through a circular pipe and plane Couette flow. These flows are linearly stable for all Reynolds numbers. The discrepancy between linear theory and experiments was attributed to the failure of LST, and several attempts to explain this discrepancy using non-linearity were made, see Stuart (1971) for a review on non-linear stability theory. In an attempt to reduce nonlinear effects, experiments in channels and pipes were conducted in cleaner (reduced disturbance) environments. It was then possible to maintain the flow in a laminar state for very high Reynolds numbers of the order of 10^4 in channels, Nishioka *et al.* (1975) and 10^5 in pipes, see Hof *et al.* (2004). This ability was enhanced further by making the walls of the channel/pipe smoother. This shows the sensitivity of these flows to free-stream disturbances and the surface roughness at the wall. Hof *et al.* (2003) have shown experimentally that the amplitude of disturbance required to trigger transition in a pipe flow scales inversely with the Reynolds number. There is also a huge volume of work dedicated to study the effect of surface roughness in pipes and channels, see for example Herwig *et al.* (2008), an dG J Kunkel & Smits (2008). Subcritical transition in channels was also explained on the basis of the non-normality

of the operator, see Criminale *et al.* (1997). There has been a lot of debate about the reason for subcritical transition in many shear flows, as to non-normality or non-linearity, see for example Reddy & Henningson (1993), Reddy & Henningson (1994), Waleffe (1995), Henningson (1996), Reddy *et al.* (1998). The balance is now tipped in favor of non-normality occurring first, and enabling linear disturbances to become large enough to go non-linear. Moreover, Henningson (1996) showed that since the non-linear terms are energy conserving, energy growth of the disturbances has to be enhanced by a linear mechanism and thus explains the subcritical transition of channels using non-normality. Note however that this argument for energy growth requires perturbation to be spatially localized or periodic, and this is not necessarily true for non-parallel flows.

A large amount of work has been done to study the effect of many other parameters like wall porosity, wall heating, viscosity variations, wall flexibility, etc on the stability of channel and pipe flows. Given below is a very limited, representative survey related to channels (except the first reference which relates to a tube). Shankar & Kumuran (2000) in a series of studies have shown that flow through a flexible tube is destabilized at higher Reynolds numbers as against its rigid wall counterpart. Govindarajan *et al.* (2001), Govindarajan *et al.* (2003) have shown that a channel flow can be stabilized by having small viscosity variations near the critical layer. Tilton & Cortelezzi (2006), Tilton & Cortelezzi (2008) studied flow through channels with one or two porous walls and found that even very small amounts of wall permeability decrease the stability of the flow. Govindarajan (2004) studied the effects of miscibility of two fluids in a channel flow. The effect of wall heating in a channel flow is studied by Wall & Wilson (1996), Sameen & Govindarajan (2007) discuss the separate effects of viscosity, buoyancy and heat diffusivity. Sahu *et al.* (2008) show that wall slip, which hugely stabilizes flow through a straight channel, actually has a minor destabilizing effect in a divergent channel. The transient growth obtained by a parallel stability study is unaffected by either slip or divergence. Sahu *et al.* (2007) studied the stability characteristics of a two-layer fluid in a channel, with one layer as non-Newtonian fluid. Apart from all the above mentioned parameters affecting the stability of flow through a channel, wall divergence has a large effect. This alone is studied here and is discussed in detail below.

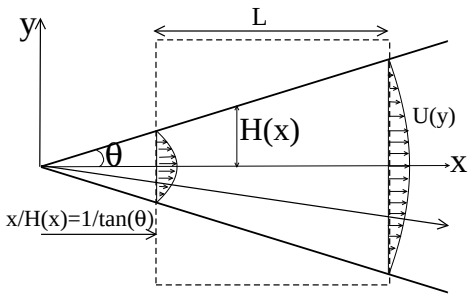

Figure 3.1: Schematic of Jeffery-Hamel flow originating from a point source at the origin. θ is the semi-divergence angle in degree and x is the streamwise co-ordinate. Note that the axes are non-orthogonal. For global stability computations, the inlet of the two-dimensional domain is fixed at a distance of $1/\tan(\theta)$, as the length-scale of the problem is the inlet half-width. The two-dimensional domain over which the global stability computations are made is shown by the rectangular box.

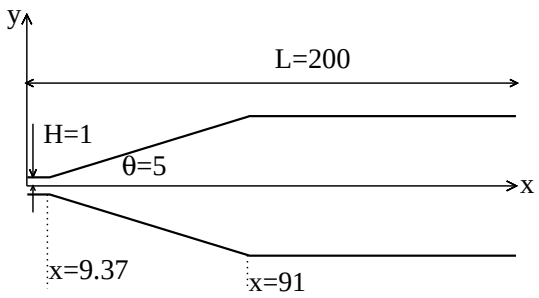

Figure 3.2: Schematic of the channel with the finite divergent section, referred to here as SDS for straight-divergent-straight. The exit straight region is kept sufficiently long to achieve parabolic velocity profile at the exit.

3.2 Diverging channel

The steady laminar two-dimensional flow of incompressible fluid within an infinite wedge driven by a line source/ sink situated at the intersection of the rigid planes that form the wedge (figure 3.1) was first described by Jeffery (1915) and Hamel (1916) (see e.g. Schlichting (2000)). Such a flow is called Jeffery-Hamel (JH hereafter) flow. Stability of JH flows was first studied by Eagles (1966) who showed that divergence has a destabilizing effect. He calculated the critical Reynolds number, Re_{crit}, as a function of the divergence angle using the Orr-Sommerfeld equation and showed that Re_{crit} falls rapidly with wall divergence.

The stability of JH flows was also studied by many other researchers. Nakaya &

Hasegawa (1970) studied the flow through diverging plates by analytic expansions and found critical values for the onset of instability. The base flow considered here is not the JH solution, but derived analytically as a function of the diverging angle. Eagles & Weissman (1975) studied the flow through straight walled diverging channels using WKB method. The base flow considered here is the JH profile. Eagles & Smith (1980) studied the flow through a channel with a finite diverging curved wall region confined between straight regions using the WKB method. The base flow considered here is solved numerically. Allmen & Eagles (1984) solved the above mentioned two problems numerically and obtained a very good match with the earlier predictions. Georgiou & Eagles (1985) studied the stability of flow through curved walled channels using WKB method. The base flow for this is calculated as a perturbation for the JH flows. The parameters governing the stability characteristics of channels with straight walls, curved walls, and walls changing the angle of divergence are discussed and compared in this paper. Banks *et al.* (1988) studied linear and weakly non-linear perturbations to the JH solutions and obtained critical angles necessary for disturbance growth. Hamadiche *et al.* (1994) showed that the critical Reynolds numbers for JH flows based on both the volume flux and the axial velocity decrease rapidly with diverging angle (θ), and a quantity defined as a product of these Reynolds numbers with (θ) stay constant or scale linearly with (θ). Uribe *et al.* (1997) studied the stability of JH flows using finite element method and obtained critical parameters for the stability of uni-directional and bi-directional flows. Dennis *et al.* (1997) studied numerically the flow in a diverging channel enclosed between two arcs and found that the inlet and outlet conditions have a very strong influence on the non-linear development of the flow. Drazin (1999) has a brief review on the instability of flow through diverging channels. To mention a related work, Sahu & Govindarajan (2005) studied the stability of flow through a slowly diverging pipe and showed the destabilizing effect of divergence too. This result is very special because according to linear stability theory, flow through a pipe is linearly stable for all Reynolds number. The fact that even a small amount of divergence in the pipe makes the critical Reynolds number ‘finite is very interesting. Banks *et al.* (1988) and McAlpine & Drazin (1998) showed that while divergence drastically destabilizes the flow, convergence causes a huge stabilization. Putkaradze & Vorobieff (2006) studied JH flows experimentally and demonstrated that a symmetric unidirectional outflow JH solution, if it exists, is always stable. This seems to contradict the results of Uribe *et al.* (1997). Kerswell *et al.* (2004) studied, using a theoretical model, the non-linear

evolution of two-dimensional spatial waves in JH flows. In all of the numerical work mentioned above, the researchers have made the assumption of locally parallel flow and the dramatic dependence of Re_{crit} on wall divergence angle has been captured to a great extent. The papers are all, however, silent on why the dependence should be so dramatic. We provide a mathematical explanation in section 3.5.

In the theoretical JH flow, the velocity profile is self-similar and the velocity scales inversely with distance x, while the channel width scales linearly with x as shown in figure 3.1, see Schlichting (2000). Hence the Reynolds number, defined based on the centerline velocity and half channel width, does not vary downstream. One would therefore expect a disturbance of constant dimensionless wavelength, combined with a self-similar amplitude function $\phi(y)$, to satisfy the stability equations. Given the large amount of work on the stability of JH flows using local stability approaches, why do we need to study this geometry as a global stability problem? We study it here to show how a global analysis can reveal fundamental characteristics of the instability which are not accessible to the parallel or WNP approaches. In fact none of the global instability modes resemble parallel or WNP modes. The point is that if the geometry, the pressure, or other relevant parameters were varying in a complicated fashion with x, one would not be surprised that global stability studies give results very different from the parallel. The fact that global modes can look qualitatively different in this, perhaps the simplest of non-parallel flows one could construct, is more interesting. This finding in JH flows may be contrasted with recent studies on boundary layers e.g. Ehrenstein & Gallaire (2005). There it is seen that global stability results do differ from WNP quantitatively by a small percentage, but a given mode is still described by a basic WKB structure, of a wave with a slowly changing wavelength streamwise. We highlight here only a few important aspects of the effect of two-dimensionality on the disturbance eigenfunction. In addition to the JH, we consider a more realistic geometry as shown in figure 3.2, where the mean flow is obtained numerically. This flow is referred to as SDS hereafter, for a channel with Straight-Diverging-Straight geometry. Similar geometries were studied before by Eagles & Smith (1980), Nakayama (see in Drazin (1999)), Tutty (1996). The reasons for choosing such a geometry is two-fold: (1) It is easily realizable in real-life and hence experimental validation is possible (2) Streamwise boundary conditions will become straightforward; Neumann boundary conditions are applicable at the inlet and exit straight regions.

Many shear flows are spatially developing, where, as we proceed with the flow in x,

there are changes in the local Reynolds number as well as the local flow profile. JH flows are unique in this aspect as they evolve spatially but (i) the local Reynolds number does not change with x and (ii) the mean flow is self-similar. This feature of JH flows makes it a good candidate for a global stability study as it would give information about the effect of spatial development alone and not of streamwise changes in Reynolds number. One reason for the global approach displaying a much richer variety of modes than the parallel is that the disturbance eigenfunction obtained from solving the Orr-Sommerfeld equation can be multiplied by an arbitrary function of x and still satisfy the equation. In the case of global stability, the prefactor function of x is well defined and it is expressed in the eigenfunction solution.

3.3 Base flow

As mentioned before, we consider both the infinitely diverging JH flow and the finite diverging SDS flow. The base flow considered for both these cases are explained separately below. The JH base flow is self-similar while the base flow for SDS is obtained numerically.

3.3.1 JH base flow

The steady laminar two-dimensional flow of incompressible fluid within an infinite wedge driven by a line source/ sink situated at the intersection of the rigid planes that form the wedge (figure 3.1) was first described by Jeffery (1915) and Hamel (1916) (see e.g. Schlichting (2000)), by the similarity equation

$$U''' + 2SUU' + 4\theta^2 U' = 0, \tag{3.1}$$

$U(+1) = U(-1) = 0; U(0) = 1$. Here U is the mean velocity in the similarity co-ordinate $\eta = y/H(x)$, θ is the semi-divergence angle as shown in figure 3.1, H is the channel half-width, the primes stand for differentiation with respect to η, $S \equiv \theta Re$, x is the streamwise co-ordinate and y is the wall-normal co-ordinate. As mentioned before, the Reynolds number (defined as $Re \equiv U_c(x)H(x)/\nu$, where the subscript 'c' stands for the channel centerline and ν for kinematic viscosity), is constant downstream, in contrast to most other developing shear flows. The flow displays a separated region for S greater

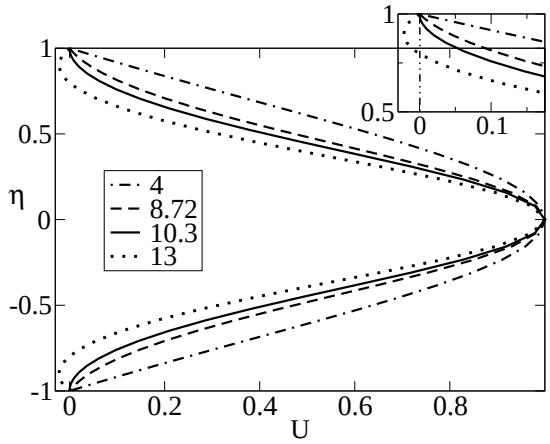

Figure 3.3: The self-similar JH equation 3.1, plotted for different values of $S \equiv \theta Re$. As can be seen clearly from the inset, this flow becomes separated for values of S greater than 10.3.

than 10.3. A plot of U obtained for different values of S is shown in figure 3.3.

The domain over which global stability computations are performed is shown in figure 3.1. As the half-channel width at the inlet H_i is the length scale, the starting point in the x direction of this domain obeys the relation $x_{start}/H_1 = 1/\tan(\theta)$. The domain extends up to $x_{end} = x_{start} + L$, where L is kept sufficiently long. The velocity profile at the inlet is obtained by solving equation 3.1 using a fourth order Runge-Kutta method with 10000 grid points. Velocity profiles at other x locations are obtained using the similarity scaling relation $U \sim x^{-1}$, which is given explicitly as,

$$U(x(i), y) = \frac{U(\eta)}{x(i)} x(1) \qquad (3.2)$$

$$U'(x(i), y) = \frac{U'(\eta)}{x(i)} x(1) \qquad (3.3)$$

$$U''(x(i), y) = \frac{U''(\eta)}{x(i)} x(1) \qquad (3.4)$$

$$V(x(i), y) = H'(i) \frac{x(1)}{x(i)} \left(\eta U(\eta) - \int_0^\eta U(\eta) d\eta \right) + \frac{H(i) x(1) \int_0^\eta U(\eta) d\eta}{x(i)^2} \qquad (3.5)$$

where the wall-normal velocity is obtained from continuity. Here $x(1)$ is the first x location and $x(i)$ corresponds to any x location with $1 \leq i \leq n$, where n is the number of grids in x. As per the scaling relation given in equation 3.2, U decreases with distance. This is schematically shown in figure 3.4. Typical plots of U, V and the streamfunction

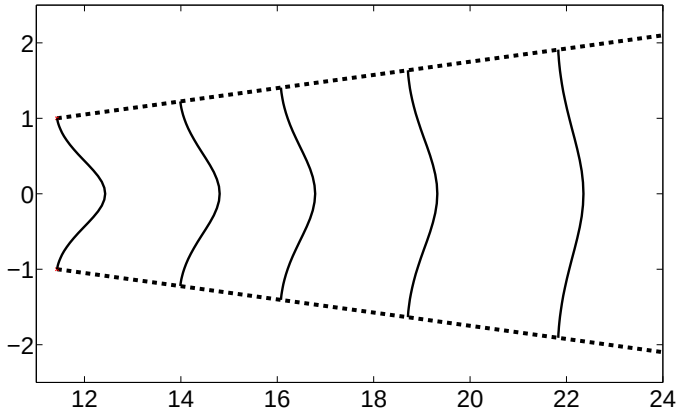

Figure 3.4: Local streamwise velocity profiles of JH flow at Re=100, θ=5. The velocity variation is given in equation 3.2.

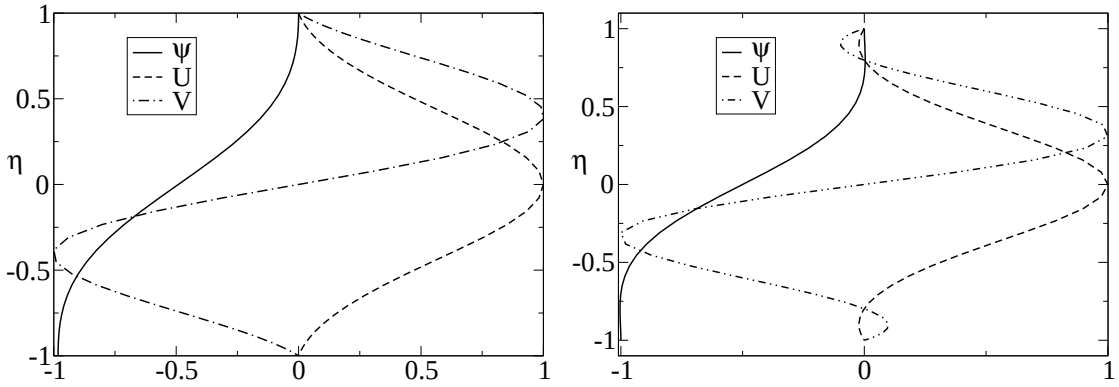

Figure 3.5: (Left) Plots of streamfunction, streamwise velocity and wall-normal velocity of JH flow for Re=100, θ=5. (Right) Same as the left figure, but for Re=150. The flow at this Reynolds number is separated. Note that the values are scaled with their maximum value for ease of viewing.

ψ of JH flow at a particular streamwise station are shown in figure 3.5, for an unseparated case (left) and a separated case (right). Contours of U and V for a Reynolds number of 100 and semi-divergence angle $\theta = 5$ are shown in figure 3.6.

3.3.2 SDS base flow

The mean velocity profile for the channel with the finite divergent section (SDS, figure 3.2) is obtained by a numerical solution of the streamfunction-vorticity formulation of the two-dimensional Navier-Stokes equation on a 512x32 grid. The numerical method

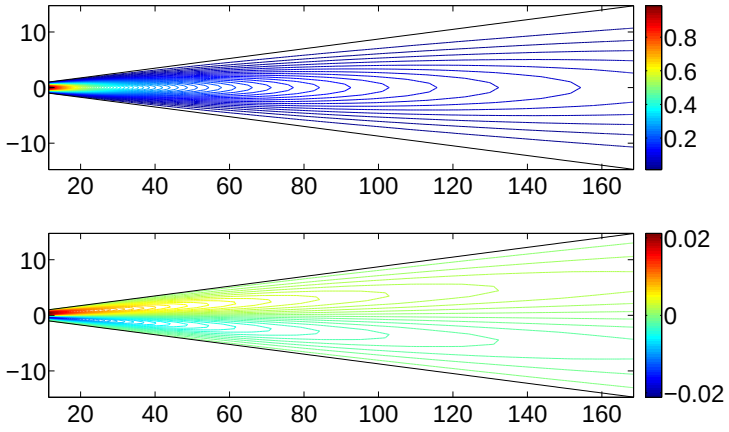

Figure 3.6: Contours of streamwise (U) and wall-normal (V) velocity of JH flow at Re=100, θ=5. This flow has $S = 8.72$ and is not separated.

is explained in section 2.7. At each Re and θ, it is ensured that the final straight section is long enough for the flow to attain a parabolic profile well before the exit. This requirement has to be met in order to apply Neumann boundary conditions at the exit. The length of this exit straight section increases approximately linearly with increasing Reynolds number. In the present computations, the divergence starts at $x = 9.37$ and ends at $x = 91$, as shown in figure 3.2. This flow is solved at the same parametric settings as that of JH flow, detailed comparison given in next section.

3.4 Comparison of base flow - JH and SDS

The computations are conducted at many Reynolds numbers and different angles of divergence. To give a representative comparison of the base flow of JH and SDS flows, we consider the flow for a half-angle of divergence of 5 degrees, and a Reynolds number of 100. The base flow profiles obtained for the JH flow from the similarity equation (3.1) and the SDS channel numerically are compared in figure 3.7. Plotted here is the streamwise velocity U versus the non-dimensional co-ordinate η. The lines shown in the figure are obtained for SDS at three different x locations and the symbols are the solutions of equation (3.1) for $S = Re\theta = 8.72$. We note that the JH profile is not separated at this S value, whereas the SDS profile is separated downstream due to centerline acceleration, caused by the divergent section being finite. A domain length of $L = 200$ is found to be sufficient to get a parabolic flow at the exit. The local velocity profiles obtained for SDS

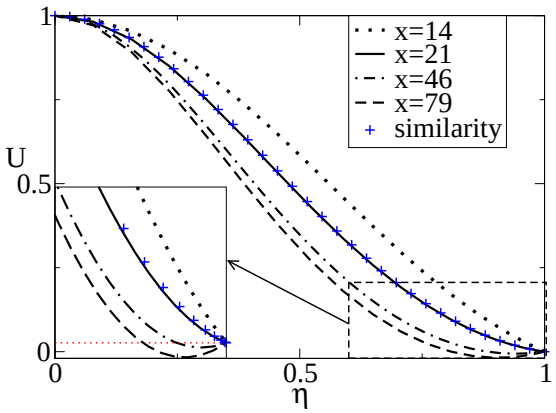

Figure 3.7: Comparison of the mean velocity profiles of JH flow (shown in figure 3.1) with those of SDS flow (figure 3.2) at a few streamwise locations. The symbols are for a similarity solution with $S = 8.72$ (Re=100, $\theta = 5^o$). The lines are for the SDS channel at different x locations. It can be seen that the JH profile matches with the numerical profile for the SDS channel at $x = 21$.

channel in the exit straight region is shown in figure 3.8. It can be seen that the profile matches well with parabolic profile at the exit of the domain. Contours of the mean streamwise velocity distribution are shown in figure 3.9. A region of weak separated flow extending over most of the divergent portion can be discerned in the SDS.

3.5 Sensitivity of the critical Reynolds number to divergence

While it is well known that the critical Reynolds number of this flow is dramatically sensitive to wall divergence, the cause of this sensitivity is not explained in the literature. We begin by asking why this happens and propose a scaling argument, which gives a good approximation for variation in the Re_{cr} with wall divergence. To explain this, we expand the mean flow at small divergence as a perturbation of the Poiseuille solution. At $S << 1$, we may write the solution to equation 3.1 as a small perturbation to the plane Poiseuille flow solution as,

$$U = 1 - y^2 + S(ay^5 + by^4 + cy^3 + dy^2 + ey + f), \tag{3.6}$$

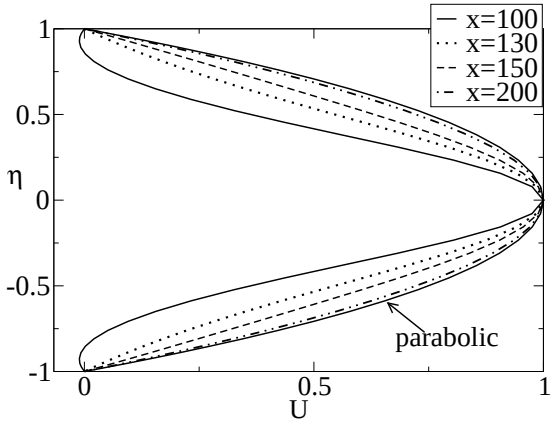

Figure 3.8: Mean velocity profiles of SDS flow (figure 3.2) at a few streamwise locations in the exit straight region of the domain. As can be seen, the velocity profile at the exit of the domain is almost parabolic, corresponding to the fully developed straight channel profile.

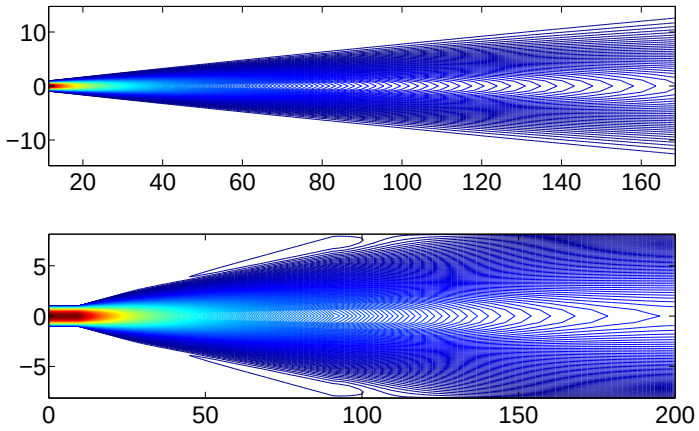

Figure 3.9: Comparison of mean streamwise velocity contours of JH (top) and SDS (bottom) flows, for the case shown in figure 3.7, with $Re = 100$, $\theta = 5^o$. Note the long region of weak separation in the SDS case.

where S is a small parameter. Substituting the above in equation 3.1, we get,

$$U = 1 - y^2 + S(-y^6/30 + y^4/6 + 2/15y^2). \tag{3.7}$$

The full non-parallel stability equation is given in Govindarajan & Narasimha (1995) as,

$$Ra\phi = 1/Re(\text{viscous terms including all non-parallel terms}). \tag{3.8}$$

Here, Ra is the Rayleigh operator. If we write the above equation for a JH flow and that for a plane Poiseuille flow and subtract them, and use ideas from Govindarajan & Narasimha (1997), we can show that the important terms are,

$$Ra_P\phi + 1/Re_{cr}(\phi^{\text{iv}} + \text{higher order terms}) + i\alpha\Delta U''\phi. \tag{3.9}$$

Here Ra_P stands for the Rayleigh operator for Poiseuille flow. The important term in this equation is the change in U'', expressed as $\Delta U''$. To realize the importance of this term, we refer here to two theorems which talk about the necessary conditions for inviscid instability, see Schmid & Henningson (2001). The first is Rayleigh's inflection point theorem, which says that an inflectional profile is always inviscidly unstable. An inflectional profile is one in which the slope changes sign, and hence has the second derivative U'' as zero somewhere. The second is Fjortoft's criterion, which gives a more stringent condition on the stability of inflectional profiles. It states that the vorticity has to reach a maximum at the point of inflection, not minimum, for inviscid instability. Even though these theorems are derived based on inviscid principles for parallel flows, they are used as general guidelines for the stability of viscous non-parallel flows too.

For a plane channel flow, the second derivative U'' is -2 at every wall-normal location, and one associates such a large negative value with increased stability. A channel with small divergence or convergence has, from equation 3.7,

$$U'' = -2 + S(-y^4 + 2y^2 + \frac{4}{15}). \tag{3.10}$$

The departure from plane channel flow is given as,

$$\Delta U'' = S(-y^4 + 2y^2 + \frac{4}{15}). \tag{3.11}$$

Figure 3.10 shows this departure of U'' from -2 for different values of S. The values

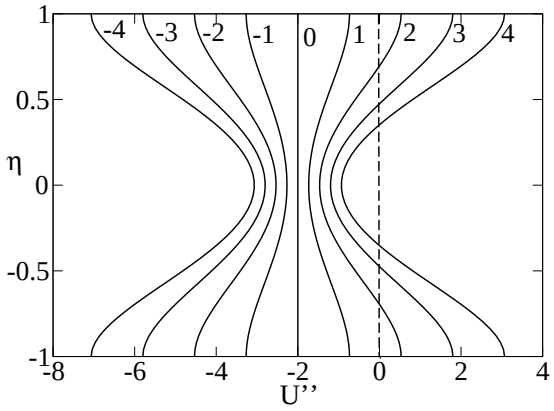

Figure 3.10: Plots of U'', equation 3.10, for different S. The values of S are indicated close to each curve, towards the top of the figure. A positive S takes the curve more towards zero, and a negative S takes the curve away from zero, making the flow close to inflectional or further away from inflectional, respectively.

of S are indicated close to each curve, towards the top of the figure. For positive values of S, i.e. diverging channels, the plot of U'' moves towards zero and for a value of S between 1 and 2 the flow becomes inflectional close to the walls. For negative values of S, i.e. converging channels, the plot moves farther from zero, thus making the flow more stable.

To understand the departure in the stability characteristics of converging/diverging channels caused by this $\Delta U''$ term, consider the critical values for a straight channel, Reynolds number 5772 and wavenumber 1.02. Assuming that the least stable wavenumber and its eigenfunction do not change for a very small change in the angle, and substituting the above values into the non-parallel operator (equation 3.8), we get an approximate equation for the Re_{cr} as a function of the divergence angle θ, as

$$\frac{1}{{Re_{cr}}^2} - \frac{1}{5772 Re_{cr}} = 3 \times 10^{-4}\theta. \tag{3.12}$$

The constant factor on the right hand side comes from solving for the parallel flow with $\theta = 0$, at $Re = 5772$, using equation 3.11, and integrating across the channel. Figure 3.11 shows the comparison of the above equation which is entirely obtained from the Poiseuille flow solution, against the Orr-Sommerfeld equation results for a JH flow. We can see that this equation does reasonably well in explaining why the critical Reynolds number rises at low angles of convergence (negative θ) and drops steeply with divergence (positive θ). The reason, as explained above, is the $\Delta U''$ term, which explains

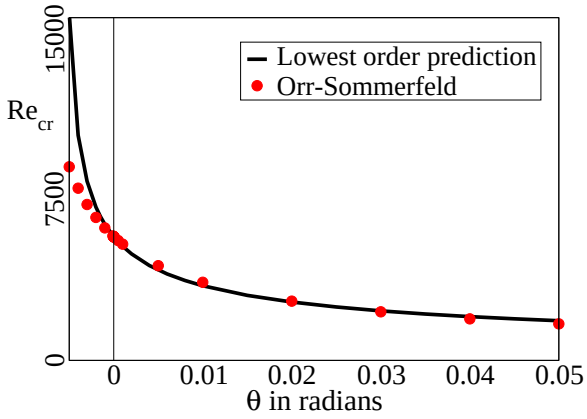

Figure 3.11: Sensitivity of Re_{cr} to the divergence angle θ at very small θ. Equation 3.12 (black line) obtained from perturbing about the Poiseuille solution is reasonable at predicting the sensitivity of Re_{cr} with change in θ. Positive θ is for divergence and negative θ is for convergence.

the 'departure from inflectionality' associated with the profile. Also, it is important to remember that even smallest changes in the U'' values, associated with the smallest angles of convergence/divergence, can cause a huge change in the stability characteristics of these flows. We can see here the drastic change in critical Reynolds number caused by a very small change in the angle. The action of viscosity as a singular perturbation in the stability operator gives rise to the large effect.

3.6 Global stability analysis

The length of the JH domain is fixed equal to 50π, unless otherwise specified, and of the SDS domain is 200 as shown in figure 3.2. The results presented are supported with various sensitivity tests conducted, given in section 3.6.2. The global stability equation is discretized with n and m points in the x and y directions, respectively. As mentioned before, Chebyshev spectral collocation is used in both directions. This clusters the grid points close to the walls in the wall-normal direction (which is desirable), and close to the inlet and exit of the domain (which is not desirable). Hence the grids are stretched in x to give a more or less uniform distribution of points in the streamwise direction using the stretching function specified in section 2.6.4. After several trials for better accuracy,

the values of a and b are fixed to be $a = 0.5, b = 3.0$.

3.6.1 Boundary conditions

No-slip and no-penetration boundary conditions on both the walls are prescribed. The correct streamwise boundary conditions to apply are not obvious, and moreover, can have a strong spurious influence on the results. We aim to minimize this influence. This is one important reason for including a study on an SDS channel, in which the region of disturbance growth may be expected to be localized around the divergent portion, and the flow far upstream and downstream to be stable at the low Reynolds numbers considered in this work. In an SDS channel therefore, especially one with a long straight section at the exit, we have at least two options for streamwise boundary conditions, namely Neumann and extrapolated boundary conditions (EBC), (explained in section 2.31), at both the inlet and the exit. In several global stability studies, Robin boundary conditions are used, see Ehrenstein & Gallaire (2005), where wave-like behavior is prescribed, if necessary with different wavelengths fixed at the inlet and the exit. We note however that since the global mode is not necessarily wave-like, the Robin boundary conditions would be inappropriate (except for the purpose of comparison with local stability approaches, as done in the validation section 2.12). We use EBC, as we see it as being the least prejudicial, both for JH and SDS. It is found that if a sufficiently long domain is considered, the precise form of the boundary conditions does not affect the results. Unless otherwise specified, the above mentioned extrapolated boundary conditions are used for all the results presented.

Computations in this geometry with extrapolated boundary conditions showed a class of modes which propagated upstream. A time evolution of the modes, in the form of a movie, revealed this. Howard's semi-circle theorem does not admit disturbances with negative phase speeds for this flow at this parametric setting. Even though the global modes from the present non-parallel approach need not obey this theorem, we do not have a physical interpretation for these upstream propagating modes. It is possible that reflections from the outer boundary could cause such upstream propagation. Hence to make sure that these modes are not an artifact of the boundary conditions, a sponge is applied at the exit of the domain. A sponged region in a flow is a low Reynolds number region introduced artificially just before the boundary in a smooth manner, such that any spurious reflection from the boundary gets killed in that region due to the low values of

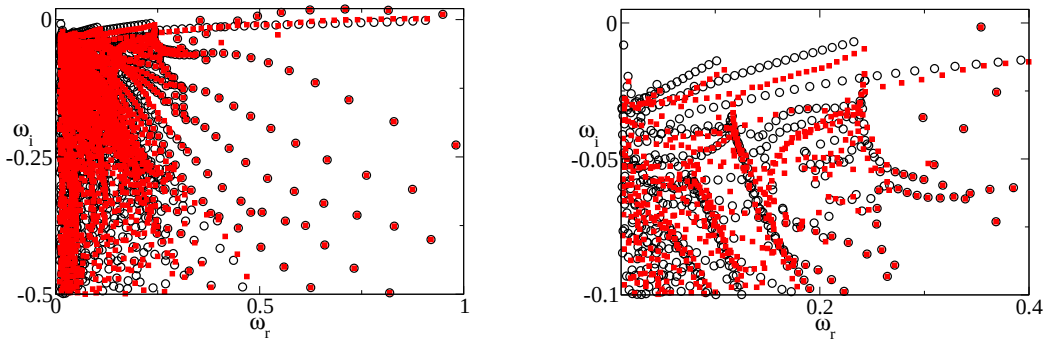

Figure 3.12: (Left) Sponging applied artificially by reducing the local Reynolds number without conserving mass (black circles) and with conserving mass (red squares) for JH flow at $Re = 100$, $\theta = 5$. (Right) Zoomed in portion of a part of the spectrum. The basic structure of the spectrum in terms of the distinct branches is unaffected. Also, the qualitative structure of the modes obtained are similar in the respective branches.

Reynolds number. In the present work, the local Reynolds number in the exit region is reduced using the smooth hyperbolic tangent function. To achieve this, the local velocity U is reduced and V is calculated accordingly. Since this was done by reducing the mean velocity, this region does not conserve mass flux. Computations are also repeated in which mass is conserved in the sponged region. This is done by neither reducing U nor V, but by expressing the Reynolds number in the stability equation as a reducing function of x. No qualitative difference was found in the results obtained with the above mentioned two types of sponging, see figure 3.12. The former method was opted for. Even after application of large levels of sponging, the upstream propagating modes do not disappear. The importance or physical relevance of these modes is discussed in section 3.7.

Sponging strength is defined as the ratio of the decrease in the Reynolds number between the flow and the exit, to the Reynolds number of the flow. Sponging strengths of between 50% to 90% have been used. The sponged length is the fraction of the domain over which the sponging is applied. For the SDS case, it is ensured that the sponging is applied only in a portion of the exit straight region, with sponged lengths ranging from 20% to 40%. Within this range of strengths and lengths, it is seen that the results remain insensitive as discussed below in the section on sensitivity studies, 3.6.3.

3.6.2 Validation

For the purpose of preliminary comparisons of the global stability approach with the parallel or WNP stability, and also to contrast with more realistic computations made later, we begin with a JH flow on a domain whose streamwise length is fixed as the wavelength of the least stable mode in the parallel or WNP stability results. Further, a wave-like nature of the disturbance is forced at the inlet and exit of the channel by using Robin boundary conditions. (see sections 2.8 and 2.12 for detailed discussions). At the inlet we use $(D_{xx}\phi)_1 = -\alpha_1^2\phi_1$ for all y locations, where D_{xx} is the discretized form of $\partial^2/\partial x^2$. The subscript 1 corresponds to the inlet. Similarly we prescribe the fourth derivative in the streamfunction at the inlet, as well as the second and fourth derivatives at the outlet. Even-order derivatives are chosen so as to remain in the real plane and thus speed up computations, as explained in section 2.12. The choice of α at each boundary is not obvious, and we have made this choice in two ways, as described below.

In the parallel and WNP approaches, the definition of critical Reynolds number is a local one. Since the Reynolds number is constant everywhere in this flow, the dimensionless wavenumber and frequency (based on local length and velocity scales) of the least stable mode obtained by the parallel or WNP are constant too. This means that the *dimensional* wavenumber and frequency depend on the streamwise location. Therefore in a global study, we may match the wavenumber α_1 at the entry with the parallel or WNP α. At the exit, we may either match the dimensional wavenumber from the parallel or WNP, or prescribe a wavenumber corresponding to the same dimensional frequency as at the inlet, but cannot match both. The first is done by matching α_1 with the parallel result, and setting α_n/α_1 equal to the ratio of the exit and entry half-widths. This amounts to forcing the same dimensional wavenumber at the inlet and exit. Since the streamwise extent of this domain is limited, grid insensitive results are obtained in this case with only $n = 51$ and $m = 41$. Computations with this set of boundary conditions are performed for various angles of divergence, with the domain size matched each time to the wavelength of the least stable parallel mode specified at the inlet. The Re_{cr} of the global stability computations thus obtained compare reasonably well with parallel results, as seen in the red circles of figure 3.13.

The other option for the choice of inlet and exit wavenumbers for Robin boundary conditions is exercised by setting α_1 to the critical WNP value. To find α_n at the exit corresponding to the same *dimensional* frequency as at the inlet, we iterate the WNP computation at the exit in α until we converge on a least-stable α whose frequency

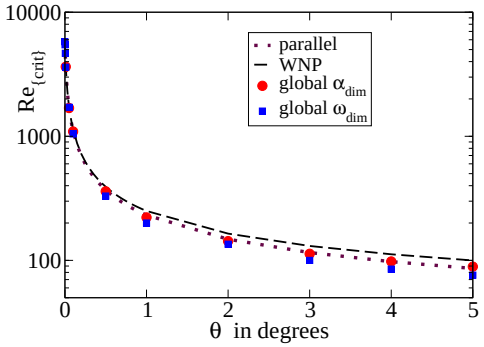

Figure 3.13: Variation of critical Reynolds number with divergence angle in JH flow. The red circles stand for the global analysis results with Robin boundary conditions holding the dimensional wavenumber the same at both inlet and exit. The domain size and inlet wavenumber are matched with parallel results at each angle. The blue squares are obtained by matching inlet conditions and domain size with WNP, and holding the exit wavenumber at the WNP value corresponding to the same dimensional frequency as the inlet.

is equal to $\omega_{nd}(1)(x_n/x_1)^2$. This expression is derived by equating the dimensional frequency ω_d at the inlet and exit, as follows:

$$\omega_d(1) = \omega_{nd}(1)\frac{U(1)}{H(1)} = \omega_d(n) = \omega_{nd}(n)\frac{U(n)}{H(n)}$$

$$\omega_{nd}(n) = \omega_{nd}(1)\frac{U_1}{U_n}\frac{H_n}{H_1}$$

$$\text{Since} \qquad U \sim x^{-1} \qquad \text{and} \qquad H \sim x$$

$$\omega_{nd}(n) = \omega_{nd}(1)\left(\frac{x_n}{x_1}\right)^2$$

where subscript nd stands for non-dimensional, $\omega_{nd}(1)$ is the critical WNP frequency corresponding to $\alpha_{nd}(1)$. This fixation of the exit wavenumber is seen to predict a smaller Re_{cr} at larger θ, as seen by the blue squares of figure 3.13.

The restriction of the domain size and the prescription of a wave-like nature of the perturbations at the entry and exit, that too of a fixed wavelength, mean that the critical Reynolds numbers predicted by the global computations are not likely to be realistic, so the main purpose of this exercise is to validate the global stability approach against simpler approaches as best we can. Later in the results section, we have performed realistic global stability analysis by using the extrapolated boundary conditions.

3.6.3 Sensitivity study

It should be noted that studying a JH flow using the similarity equation as the base flow is, strictly speaking, not realistic. A typical spectrum obtained for JH flow is shown in figure, 3.14. The spectrum has distinct branches and they are named B1 to B4, as shown in the figure. The results obtained might be dependent on the length of the domain chosen, the type of boundary condition given, the amount and extent of sponging given, etc. A similarity solution by itself, is obtainable at far downstream distances where information about the origin are forgotten. Also, JH flow solutions are obtained for a flow between two infinitely-diverging plates. Hence to simulate a self-similar solution by a finite domain in global stability computations is prone to capture some non-realistic modes in the computation. The selection of the domain length is a crucial factor in determining the stability characteristics. To avoid any 'finite domain size' effects, it has to be ensured that a sufficiently long domain is considered. Various sensitivity studies are done both for JH and SDS flows in terms of the sponging strength, length over which the sponging is applied, grid size, etc. and it is ensured that results insensitive to these parameters are discussed. A few modes are found to be sensitive to one of these parameters and they are eliminated as spurious modes by visual examination. Those spurious modes are not discussed in the thesis. Sensitivity studies given here are done for both JH and SDS flows and are given starting from figure 3.15 till figure 3.22. They are discussed in detail in the captions of the figures. It will helpful to remember the definitions of sponging strength and sponging length given in later part of section 3.6.1, as they are often referred to in the captions. For ease of viewing, the figures for JH flow are given in red-black combination, and for SDS flow are given mostly in blue-black combination. Also, in these figures, if the letter L is followed by a number, like $L200$, it denotes length of the domain under consideration. If it is followed by a number with a percentage, like $L30\%$, it means the sponging length. We can see that the major structure of the spectrum obtained is insensitive to the change in parameters, in both JH and SDS cases.

3.6.4 Comparison of JH and SDS spectra

We now compare the spectra obtained for the infinitely diverging (self-similar) JH flows and the SDS flows, using the extrapolated boundary conditions for different combinations of Reynolds numbers, $Re = 50, 100, 200$ and divergence angles, $\theta = 0.001^o, 2^o, 5^o$.

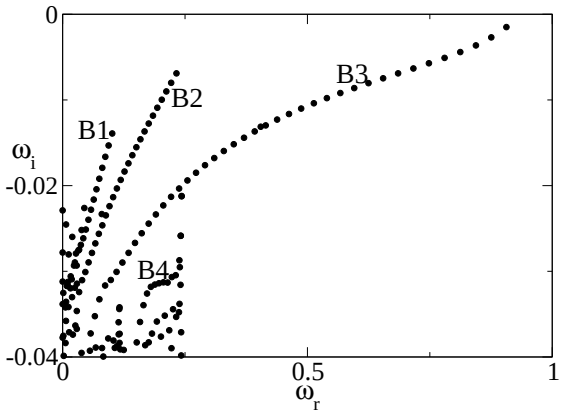

Figure 3.14: A typical spectrum obtained for JH flow. As can be seen, the spectrum has distinct branches and they are named B1 to B4 as indicated. The branches will be discussed later in detail.

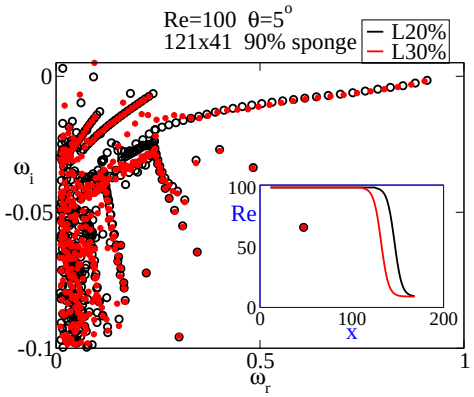

Figure 3.15: Spectra for JH flow at $Re = 100$, $\theta = 5^o$ with a sponging strength of 90% over two different lengths of the domain. $L20\%$ indicates that the flow in the 20% of the domain closer to the exit is sponged. Note that branches from B1 to B4 are insensitive to sponging length. The inset shows the Re variation with streamwise distance. The spectra shown here and in the figures to follow contain a few isolated eigenvalues, which move significantly with changes in these parameters. Their corresponding eigenfunctions were found to be spurious by visual examination.

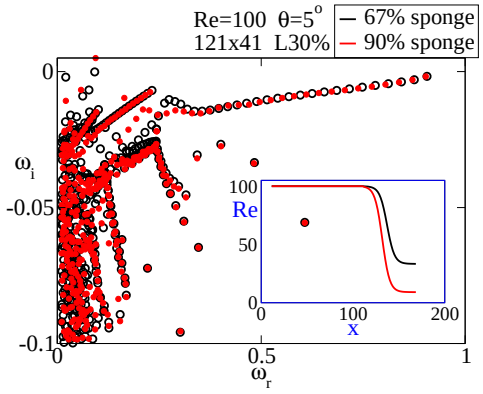

Figure 3.16: Spectra for JH flow at $Re = 100$, $\theta = 5^o$ with two different sponging strengths over the same length of the domain. The inset shows the Re variation with streamwise distance for the two sponge strengths. Note that branches from B1 to B4 are relatively insensitive to sponging strength.

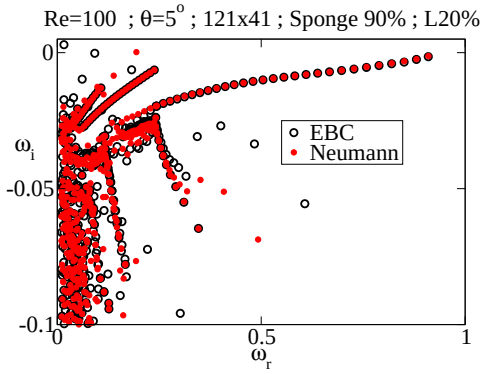

Figure 3.17: Spectra for JH flow at $Re = 100$, $\theta = 5^o$, 90% sponge over 20% length of the domain, with extrapolated boundary condition (EBC) and Neumann boundary condition.

Results presented henceforth use a grid of 221×41. The domain length for JH is $L \sim 157$ and for SDS is 100, 200 and 400 for Reynolds numbers 50, 100 and 200, respectively. Longer domains are used in SDS for larger Reynolds number as the length of the exit straight region required to attain parabolic velocity profile at the exit scales linearly with Reynolds number. The sponged lengths and sponging strengths are mentioned where appropriate. Comparisons of the spectra obtained for JH and SDS flows are shown in figures 3.23 and 3.24, respectively. Increase in θ as seen in figure 3.23, pushes the spectrum towards instability as expected. Increase in the Reynolds number, figure 3.24, increases the frequency of the most unstable modes, i.e. the different branches are stretched in the x axis. The level of instability at this θ is not too sensitive to the Reynolds number within

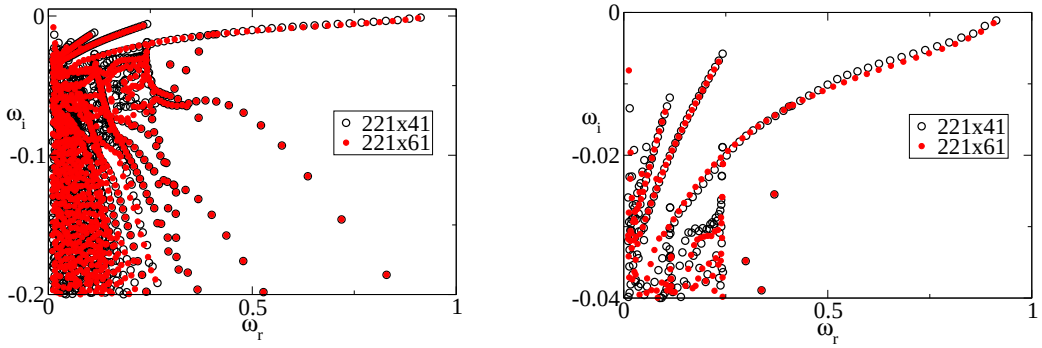

Figure 3.18: (Left) Spectra for JH flow at $Re = 100$, $\theta = 5^o$ with two different grid sizes in y. It can be seen that 41 points in y is sufficient to get reasonably grid-insensitive results. (Right) A zoomed portion of the figure close to the axis, showing the relative insensitivity of the branches B1 - B4.

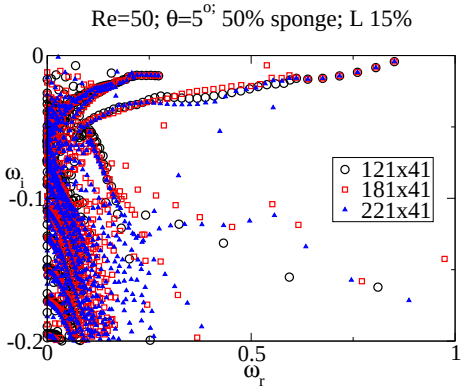

Figure 3.19: Spectra for SDS flow at $Re = 50$, $\theta = 5^o$ with three different grid sizes in x. The sponge strength is 50%, applied over 15% of the domain length.

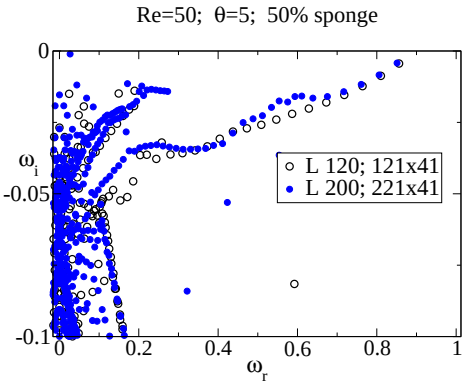

Figure 3.20: Spectra for SDS flow at $Re = 50$, $\theta = 5^o$ with two different domain lengths. Note that there is significant sensitivity to domain length.

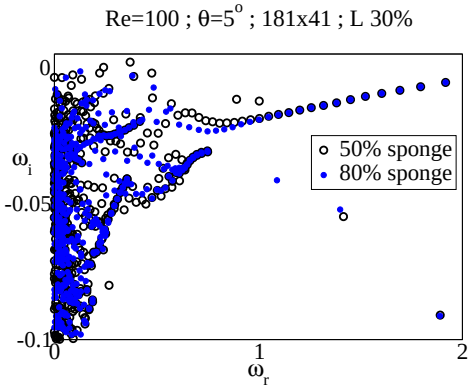

Figure 3.21: Spectra for SDS flow at $Re = 100$, $\theta = 5^o$ with two different sponge strengths applied over 30% of the domain length. Branches from B1 to B4 are relatively insensitive to sponging strengths.

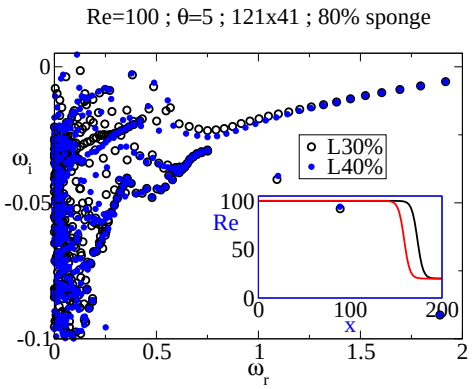

Figure 3.22: Spectra for SDS flow at $Re = 100$, $\theta = 5^o$ with the same sponge strength applied over two different domain lengths. Branches from B1 to B4 are relatively insensitive to sponging length. The two different sponge settings are shown in the inset, which shows the local Reynolds number variation with x.

this range. This subsection is devoted just for the comparison of the spectra obtained for JH and SDS flows. A detailed discussion of the two cases are given below separately.

3.6.5 JH results

We have studied JH flows at many Reynolds numbers and angles but we are interested in understanding the qualitative behavior of these flows. Hence, we consider the JH flow at $Re = 100$ and $\theta = 5$ degree as a representative case, and discuss this combination in detail. According to WNP, the Re_{cr} for this divergence angle is 99.88, and a near-neutral

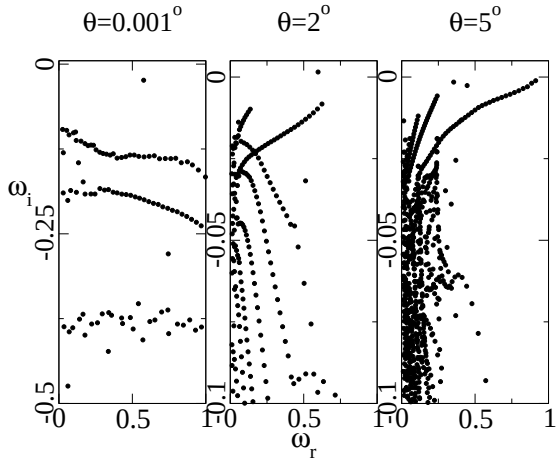

Figure 3.23: Spectra for JH at $Re = 100$ for different θ. There is an overall destabilization with increase in divergence. It is seen that with increase in θ, branches which tended to point downwards at high frequency begin to point upwards, so at higher divergence, it is the higher frequency modes which are less stable.

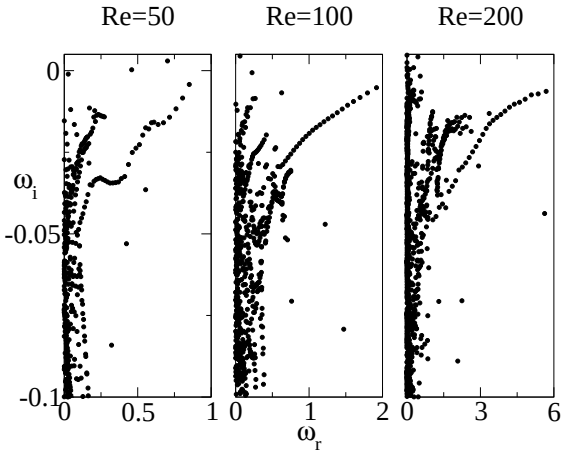

Figure 3.24: Spectra for SDS at $\theta = 5$ for different Reynolds numbers. Again some distinct branches can be discerned. The frequencies of a given branch increase with Reynolds number.

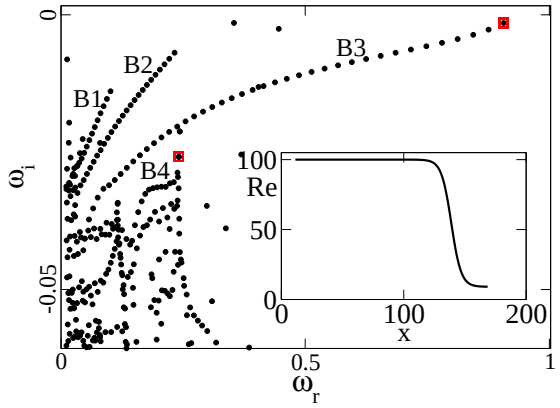

Figure 3.25: Spectrum for JH flow at θ=5 degree, $Re = 100$, $L = 157$, grid size 221×41, with 90% sponge strength, applied over 20% of the domain. The modes in branches B1 to B4 each have characteristic features, as will be seen. The Reynolds number is shown in the inset as a function of the streamwise distance, indicating the sponging applied.

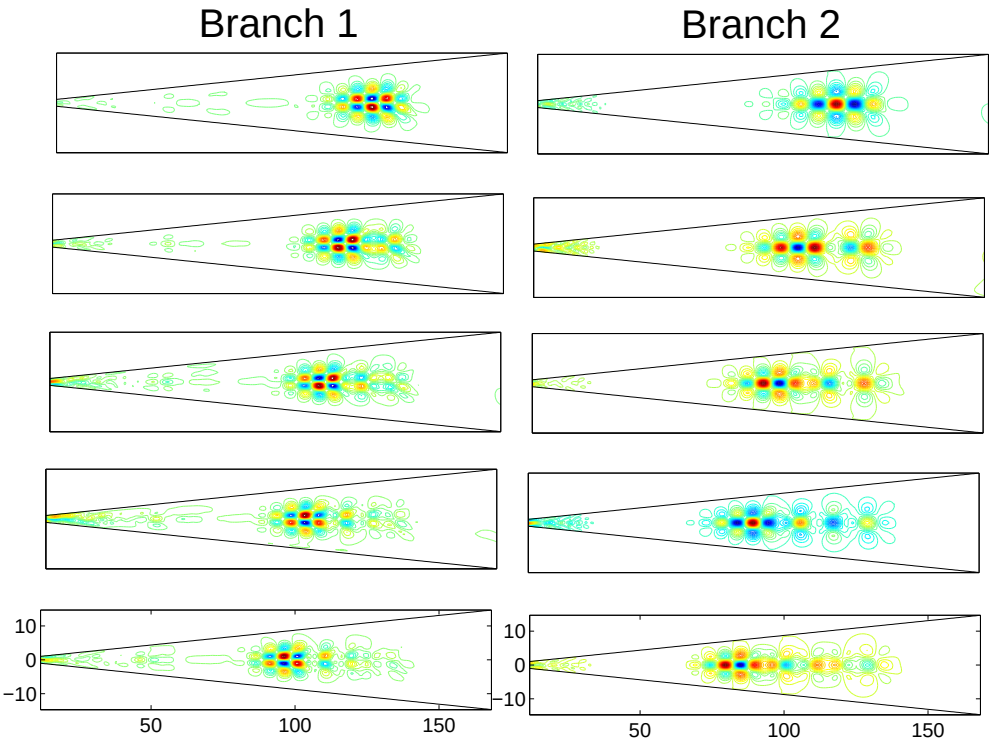

Figure 3.26: Contours of streamwise velocity of typical modes in branches B1 (left column) and B2 (right column) for JH flow at $Re = 100$, θ=5^o shown in figure 3.25.

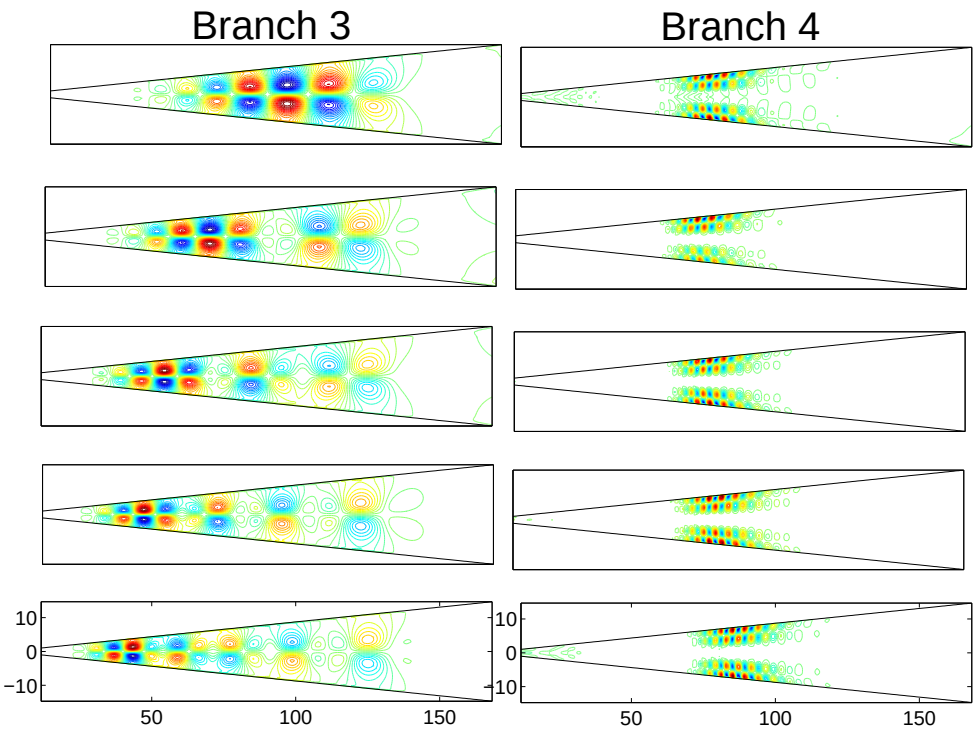

Figure 3.27: Contours of streamwise velocity of typical modes in branches B3 (left column) and B4 (right column) for JH flow at $Re = 100$, θ=5^o shown in figure 3.25. The modes in branch B3 often display multiple positive peaks in succession followed by an equivalent number of negative peaks (like the left bottom-most plot), emphasizing that they are not wave-like.

situation is a good candidate for study. The results presented in this section are qualitatively applicable to other parameters studied in the JH case. The spectrum obtained with a sponged length of 20% and a sponging strength of 90%, is shown in figure 3.25. The two near-neutral discrete modes seen are spurious, as discussed before, and they are not obtained with other grid resolutions. As mentioned before, the spectrum contains several distinct branches, and four of these, marked as B1 to B4, are chosen for further consideration. The modes in each of these branches have a characteristic structure unique to that branch. Typical modes from each branch are shown in figures 3.26 and 3.27. We emphasize that in the range that we are operating within, the eigenvalues and eigenfunctions of these branches remain reasonably insensitive to grid size, sponging and the exact form of boundary condition, as discussed in section 3.6.3. It is because of the sponging that has been applied that the global modes are damped towards the exit of the domain. As

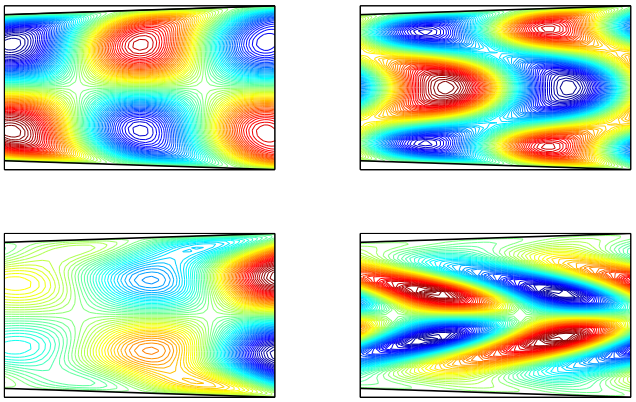

Figure 3.28: Typical 'global modes' obtained for JH flow with $Re = 100$, $\theta = 2^o$, by enforcing Robin boundary condition over a domain whose length is the same as the wavelength of the wave under consideration. Plotted here are the contours of streamwise velocity. These can be contrasted with the variety of global modes obtained from a longer domain with EBC, shown in figures 3.26 and 3.27.

can be seen, all the global modes have very weak amplitude in the sponged region. This effect of sponge is not very clear in branches B1, B2, B4 as the modes themselves are localized in x, but is very evident in the set of modes from the B3 branch, figure 3.27. The nature of all these modes reveals that the employment of Robin boundary conditions, resulting in forcing a wave-like solution, as we did earlier for comparison with parallel studies, and as often adopted in studies of spatially developing flows, is inappropriate. Typical modes obtained from our global study with Robin boundary conditions over a chosen wavelength are shown in figure 3.28. These, when compared with the global modes shown in figures 3.26 and 3.27, immediately demonstrates the richer variety of possible modes which can be revealed by a global stability analysis.

As mentioned before, the production layer of the modes in B1 and B2 are localized in streamwise extent. But modes in B3 have a different character. Contours of stream-function, streamwise and wall-normal velocities of a typical mode from B3 are shown in figure 3.29. It can be seen that the amplitude of these modes extends all over the domain and are dominant close to the centerline. Following trend is observed as we move from high frequency modes towards low frequency modes: the maximum amplitude of the mode shifts upstream in x, as can be seen from top to bottom of column 1 in figure 3.27. Also, it can be seen that the amplitude of the modes from branch 4 are dominant near

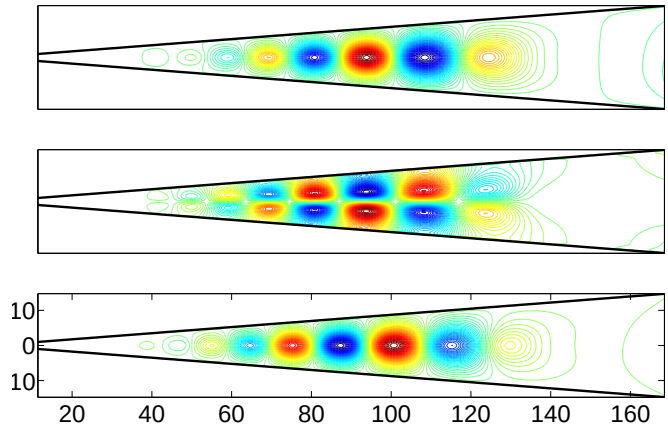

Figure 3.29: Contours of streamfunction (top), streamwise velocity (middle) and wall-normal velocity (bottom) of a typical global mode from branch 3 of figure 3.25.

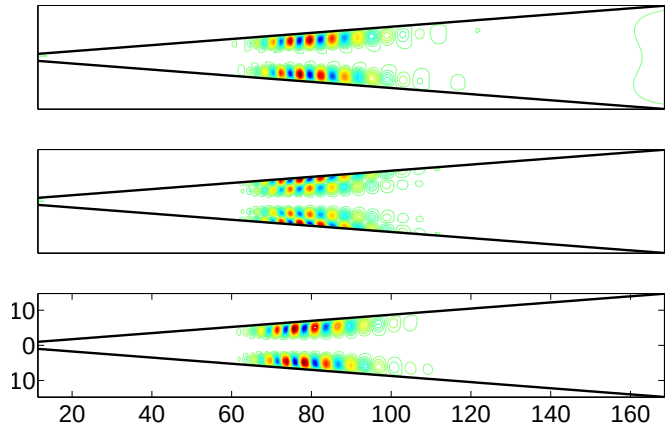

Figure 3.30: Contours of streamfunction (top), streamwise velocity (middle), wall-normal velocity (bottom) of a typical global mode from branch 4 of figure 3.25.

the wall. Contours of a typical mode are shown in figure 3.30.

Wavelet Transform

To understand a non-parallel flow, we believe that wavelet transforms are far more effective than a Fourier transform. The dominant wavelength will vary in the downstream direction for such flows, even if the mode is otherwise wave-like. A spatial Fourier transform would merely show a diffused region consisting of a range of scales, whereas

a wavelet transform would provide much more information, as we shall see.

The wavelet transform of a streamwise varying signal gives information about the dominant lengthscale associated with the signal, at each streamwise station. Wavelets form the basis functions for a wavelet transform and there are different types of wavelets, like Morl wavelet, Haar wavelet, etc. In this work, wavelet transform is performed using the inbuilt MATLAB function cwt. The results obtained from a wavelet transform are checked to be relatively insensitive to the type of wavelet used for the transformation. The brightest spot on a wavelet transform corresponds to the dominant wavenumber at that particular x location. The wavelet code written is first validated by supplying a known function in x and recovering the wavenumber out of it, as shown in figure 3.31. Here, two known functions of x, namely $\cos(2x)$ and $\cos(4x)$ are supplied and wavelet transform is performed to extract their wavenumbers. It is customary to neglect the two ends of the wavelet transform while reading the wavenumber of a particular mode, as they are blurred due to lack of adequate information from both sides. Also to note is the fact that the x axis of a wavelet transform is the grid number and not the x co-ordinate of the signal. For example, in figure 3.31, the signal spans over a length of 30, and the information is contained in 180 equally-spaced points. Thus the relation between the x axes of the signal and the wavelet transform is $181/30 \sim 6$. In this, we considered a signal with a single wavenumber. Now consider a signal, whose wavenumber gradually decreases with x, as shown in the top plot of figure 3.32. Its wavelet transform is shown to reflect this trend. This figure is characteristic of the wavelet transform one would get if we solved the problem locally by a WNP or a parallel approach. This figure may therefore be contrasted with the wavelet transforms we will show later of global modes. Note that each wavelet transform picture we show corresponds to a raw eigenfunction supplied as a function of x, with y held constant. For a WNP result, the wavelet transform at any 'y' would be identical to that at any other y. Also note that the vertical axis of a wavelet transform does not comply with the conventional notation of increasing value upwards.

It is worth comparing a wavelet transform and Fourier transform at this point. Consider a signal similar to the one shown in figure 3.32, whose wavenumber decreases with x. This signal along its Fourier transform is shown in figure 3.33. We can see that the Fourier transform peaks in the region corresponding to the dominant frequencies of the signal. Now we have two methods, namely a wavelet transform and a Fourier transform to find the dominant lengthscales of a given mode. We choose to use a wavelet trans-

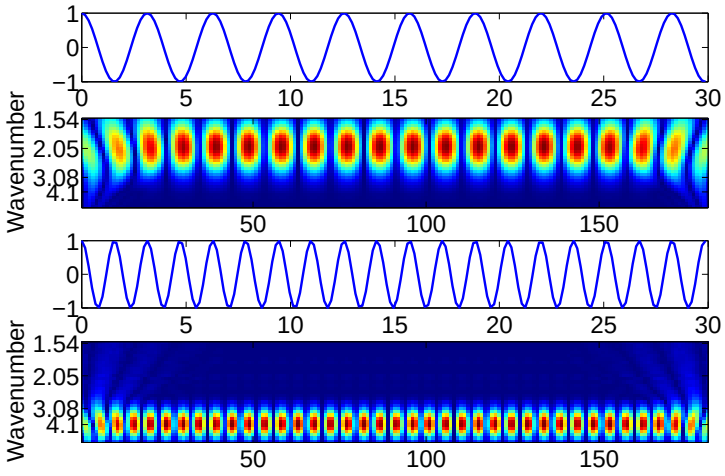

Figure 3.31: From top: Plot 1 - An input wave defined by $\cos(2x)$. Plot 2 - Wavelet transform of the input signal. The brightest spot of the wavelet transform (shown in red) corresponds to the dominant wavenumber at a particular x location. The value of wavenumber can be read from the y axis. We can see that at all the x locations of this figure, the dominant wavenumber is 2, indicating that the input signal is a wave of single wavenumber. Plot 3 - input signal defined by $\cos(4x)$. Plot 4 - wavelet transform of plot 3, indicating a wavenumber of 4.

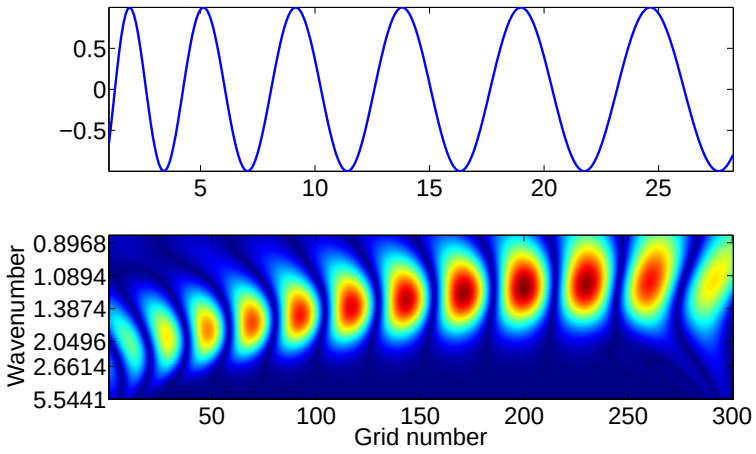

Figure 3.32: Top: A signal whose wavenumber changes with x. Bottom: Wavelet transform of this signal, indicating gradual decrease in wavenumber of the signal. Such a picture is characteristic of a WNP mode in a weakly non-parallel flow. The picture would be identical for any monitoring location wall-normal location η.

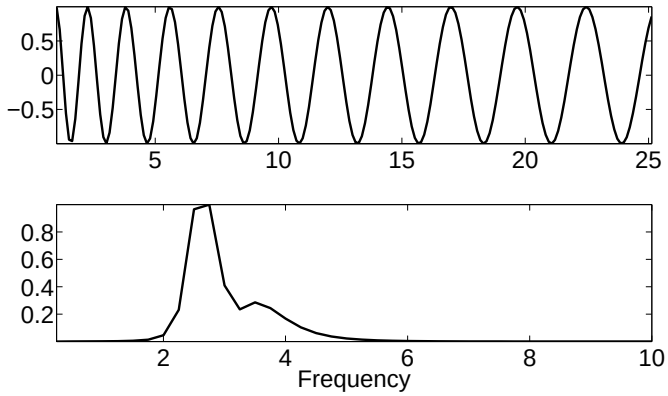

Figure 3.33: Top: A signal defined with varying wavenumber, similar to figure 3.32. Bottom: Fourier transform of this signal. As can be seen that the Fourier transform peaks around a set of frequencies indicating the dominant frequencies present in the signal. The Fourier transform does not give information along the signal, but gives the dominant frequencies of the entire signal.

form for the following reason: while both the methods give the dominant frequencies of a given signal, only a wavelet transform can give quantitative information 'along the signal'. In other words, a Fourier transform just gives information about the dominant frequencies of the entire signal whereas a wavelet transform gives information about the dominant frequency at every point in the signal. For example, see figure 3.32 which tells that the wavenumber/frequency of the signal changes from around 2.66 at the inlet to around 1 at the exit. From a wavelet transform, we can extract information about the local lengthscale/frequency of the signal, whereas it is not possible from a Fourier transform. Since we are interested in getting quantitative information about the 'change in the local wavenumber' of the global modes, we use wavelet transforms henceforth.

To support the fact that Robin boundary conditions forcing a wave-like nature to the disturbances are not appropriate in a global study, we need to quantify 'how wave-like are the global modes'. A wavelet transform is carried out to get quantitative information. At a given wall-normal location, a perturbation quantity such as the streamwise velocity, is a function of x. Wavelet transform is performed on the streamwise velocity distribution of two modes indicated by the red squares in figure 3.25 and are discussed below, with the one from B4 shown in figure 3.34 and the one from B3 shown in figure 3.35.

The B4 mode shown in figure 3.34 has an appearance very similar to its fellow modes from the same branch seen in the right side of figure 3.27. Its wavelet transform shows that the structure of the mode is a strong function of both x and y. Close to the wall,

(plots 2 and 3) there is a region where the perturbation may seem locally wave-like, with a linear increase in wavelength as would be anticipated by a WNP type study. However, this expectation is belied by the wavelet transform of the perturbation closer to the centerline (plot 4). The action at this y is closer to the inlet, with no discernible wave-like pattern. In fact, the wavenumber close to wall decreases with x, and the wavenumber at the centerline is seen to increase with x.

Next, let us discuss the wavelet transform of modes from branch B3. As mentioned in the caption of figure 3.27, as we move from large frequency modes towards smaller frequencies in the B3 branch, the modes often display multiple positive peaks in succession followed by an equal number of negative peaks, indicating the non-wave-like behavior of these modes. Hence a wavelet transform of the small frequency modes would display rich non-wave-like behavior. But we would like to concentrate on the least stable mode of this branch, (shown in the left top-most plot in figure 3.27), which looks practically wave-like and its wavelet transform is given in figure 3.35. As has been discerned by visual examination, the wavelet transform of this mode appears the same at two y locations (plots 2 and 3). Hence, we might be tempted to conclude that this mode is similar to the mode one would obtain from a WNP approach, with slowly varying wavelength. But the resemblance to a WNP wave is merely superficial. First, unlike a WNP mode, the dominant length scale does not vary too much with streamwise location. This statement can be supported by comparing the wavenumber values given in the wavelet transforms in figures 3.34 and 3.35. In the former, the change in scale is far more rapid than in the latter, and neither of these corresponds to the increase in lengthscale in the geometry. This shows that global restructuring is taking place. Second, while all the modes in the other branches evolve in time by moving downstream, the modes in branch B3 move upstream in time. This upstream propagation persists without change even with the application of extreme levels of sponging. This will be further discussed in section 3.7.

3.6.6 SDS results

We now examine a global spectrum of the SDS channel at the same Reynolds number and divergence angle considered for the JH channel ($Re = 100$, $\theta = 5$). The sponging strength is 80% and sponging is applied over 25% of the domain length. A comparison of the spectra of JH and SDS is shown in figure 3.36. The dominant instability is decided by the divergent portion. The length of the divergent portion in the JH flow without

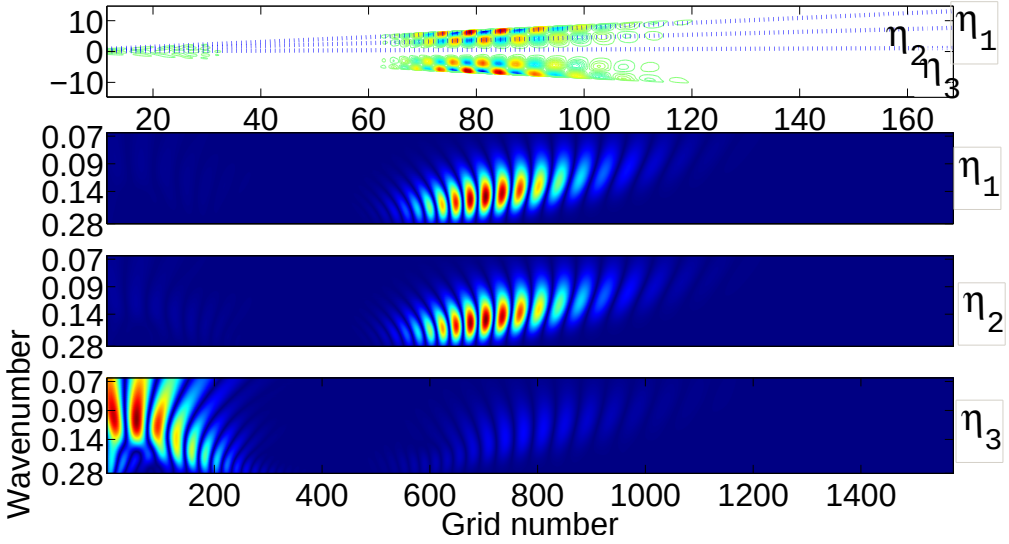

Figure 3.34: From top: Plot 1 - Streamwise velocity contours of the mode shown by the red square in branch B4 in figure 3.25, with $\omega = (0.241297, -0.0258524)$. Plots 2 to 4 - Wavelet transforms of the mode shown on top at the three wall-normal locations indicated by the blue-dashed lines, close to and away from the wall. Please note, figures discussing wavelet transform are not to scale.

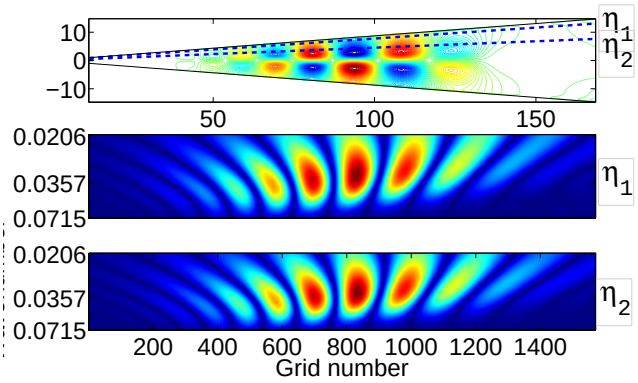

Figure 3.35: From top: Plot 1 - Streamwise velocity contours of the mode shown by the red square in branch B3 in figure 3.25, with $\omega = (0.90640, -0.0014952)$. Plots 2 and 3 - Wavelet transforms of the mode shown on top at the two wall-normal locations indicated by the blue-dashed lines.

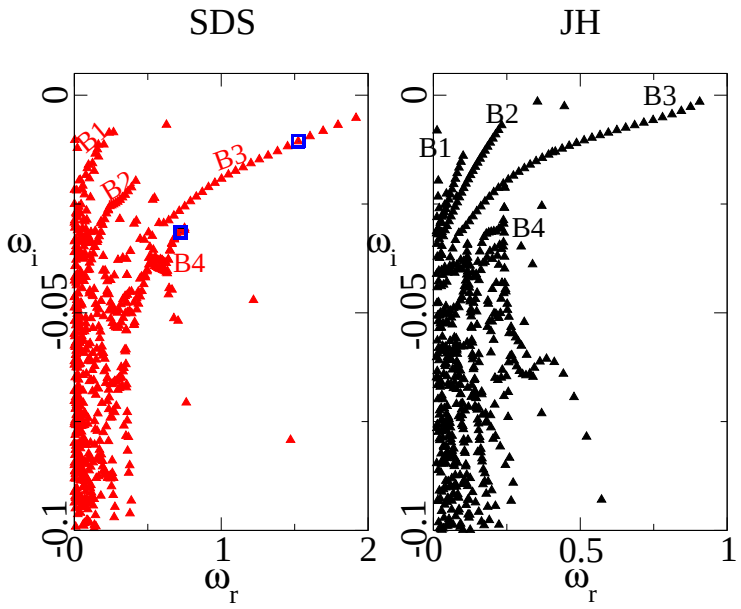

Figure 3.36: Spectra of SDS and JH flows at $Re = 100$ and $\theta = 5$. Modes in the corresponding branches marked as B1, B2, etc., have similar mode structure, but with higher frequency in the SDS case.

sponging is about 125, while in SDS it is about 80. We know from parallel and WNP studies that the frequency of the least stable mode depends strongly on divergence. The straight portion therefore will have a significant effect on the overall frequency of the modes. We may thus expect, and find, a spectrum whose frequencies differ significantly from that of a JH flow. However the mode structure remains qualitatively the same. Also, it is seen that this SDS channel is more stabilized than the JH in the sense that the growth rates of corresponding branches/modes are lower in the SDS case. This may be attributed to the presence of a straight region at the exit. Even though the SDS flow contains a region of separation, we see that the overall de-stabilizing effect of the weak separation region is smaller than the stabilizing effect of the straight region.

The mode structure of the distinct branches of the SDS flow are qualitatively similar to the JH flows. A typical mode from each branch of SDS flow is shown in figure 3.37. We see a striking resemblance with the JH modes. The mode from branch B3 has multiple positive and negative amplitudes in succession, exhibiting a non-wave-like behavior, similar to its fellow-mode in JH flow. Wavelet transform of these modes are similar to JH modes. The wavelet transform of two modes corresponding to branches B3 and B4 and indicated by blue squares in figure 3.36 are plotted in figures 3.38 and 3.39.

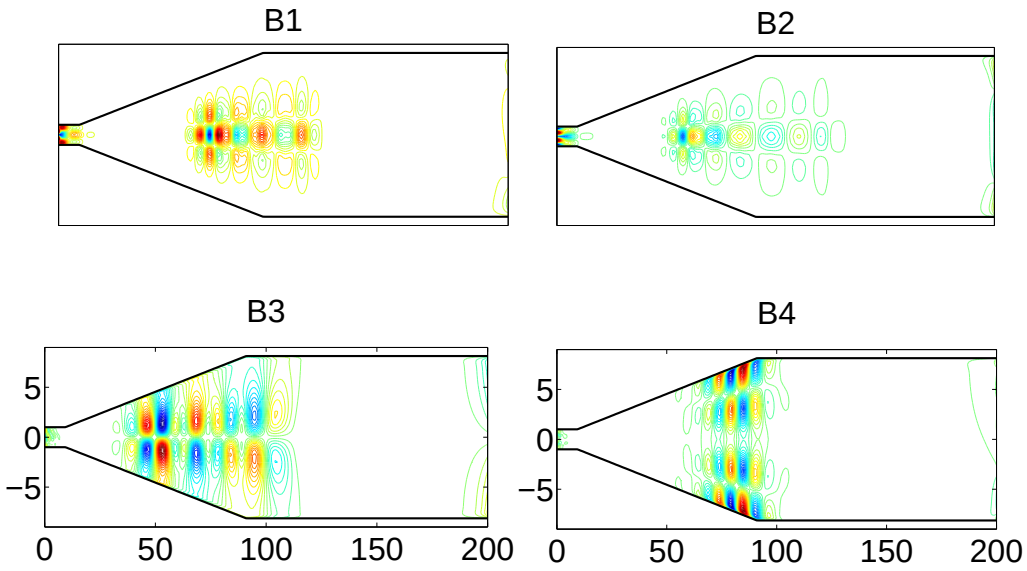

Figure 3.37: Typical modes from branches B1 to B4 of SDS flow at $Re = 100$ and $\theta = 5^o$. The spectrum obtained is shown to the left of figure 3.36. These modes look very similar to the JH flow modes, shown in figures 3.26 and 3.27.

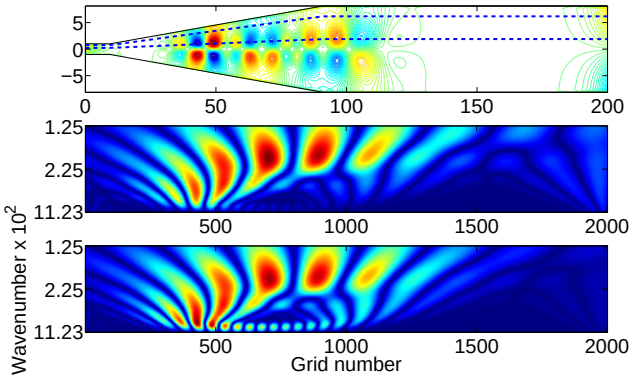

Figure 3.38: From top: Plot 1 - Streamwise velocity contours of the SDS mode shown by the blue square in branch B3 of figure 3.36, with $\omega = (1.524556, -1.059208E - 002)$. Plots 2 and 3 - Wavelet transforms of the mode shown on top at the two wall-normal locations indicated by the blue-dashed lines.

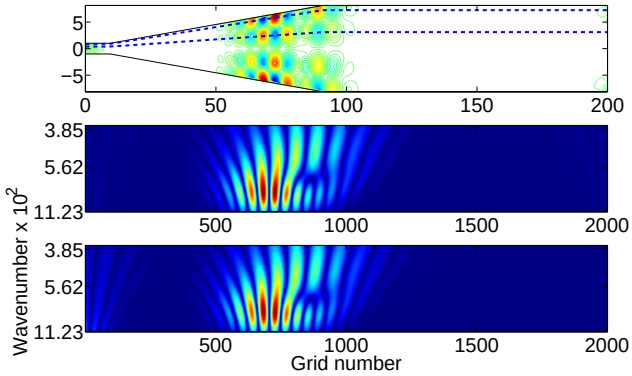

Figure 3.39: From top: Plot 1 - Streamwise velocity contours of the SDS mode shown by the blue square in branch B4 of figure 3.36, with ω=(0.7217860,-3.150661E-002). Plots 2 and 3 - Wavelet transforms of the mode shown on top at the two wall-normal locations indicated by the blue-dashed lines.

The wavelet transform of the above two modes also show similar trends as in the JH case. However note that in both B3 and B4, in addition to one dominant length scale, there is energy contribution at several other sub-dominant length scales at a single streamwise station. A wavelet study has made it possible to arrive at this finding. In SDS flow also, we see that the modes in the branch B3 are upstream propagating while modes in other branches are downstream propagating.

It has been shown that corresponding modes in JH and SDS modes share similar characteristics and mode structure. With this, we can conclude that the instability characteristics are the similar for both JH and SDS channels and that the instability is determined by the diverging portion, finite or infinite.

3.7 Upstream propagation

The source and relevance of the upstream propagating modes is still unclear to us. Initially we thought that use of a self-similar profile in a finite-size domain is the source of these reflections from boundaries and these upstream propagating modes are spurious. That was the reason to incorporate sponging at the domain exit to dampen the reflections. Since the upstream modes did not disappear even with heavy amount of sponging, we believed that these modes need not be spurious artifacts of reflections from the boundaries. We have very recently become aware of the perfectly matched layer (PML) approach of Hein *et al.* (2004), who show how reflections from the boundary can be brought down

to extremely low levels. While we believe that sponging should have an effect similar to PML, we have not been able to put this to test. One purpose of studying flow through SDS channel is to make sure that these modes are not a result of using a self-similar profile as the base flow. Since we get upstream modes in the SDS flow also where the outlet flow is parabolic and thus very stable, the argument of spurious reflections becomes weaker.

Upstream propagating modes are usually talked about in the context of absolute instability, where a disturbance introduced at a streamwise station might grow upstream and downstream, under suitable conditions. There is no immediate connection because an absolute instability talks about a 'wave packet' propagating upstream and not about a single mode having negative phase velocity. What we see here is a single mode with negative phase speed, propagating upstream. No author, to our knowledge, talks about upstream propagating global modes.

Most of the global stability studies, as mentioned before, use Robin boundary conditions in the inlet and exit of the domain. We checked the modes obtained from our global study with Robin boundary conditions. None of the modes obtained exhibited upstream propagation. This could raise doubts about the extrapolated boundary conditions used in the present work, and also on the numerical procedure, or the code itself, as possibly containing mistakes. I have made every attempt to rule such mistakes out, by a variety of checks. Further, the same code has been used for flow through converging-diverging channels and wall jets (to be discussed in the chapters to follow), and no global modes in those flows are found to propagate upstream. This confirms to the extent possible that the upstream propagating modes in this geometry are not numerical artifacts.

A relevant work on this is that of Eagles (1966), who first studied the stability of self-similar JH flows. He found disturbance modes with negative phase velocities for profiles which have a reverse flow. This result is not surprising, as this follows Howard's semi-circle theorem. This theorem states that the disturbance velocity is limited by the maximum and minimum velocities of the base flow. According to this result then, the upstream propagating modes found in the SDS channel are expected, as this flow shows small regions of separation before the exit straight region. But the JH flow discussed here, at a parametric setting of $Re = 100$ and $\theta = 5^o$, which corresponds to $S = 8.72$ is not separated. Given that Howards semicircle theorem is for parallel and inviscid flows, the upstream propagating modes in this flow are surprising, but not completely unbelievable. Probably because of the global approach we are able to see upstream

propagation at a smaller divergence than Eagles did with his Orr-Sommerfeld solution.

Moreover upstream movement in the B3 branch is seen at all Reynolds numbers considered in this work, for $\theta = 5^o$ and $\theta = 2^o$. They are however absent for very small degrees of divergence. This shows that the upstream propagating modes appear beyond a critical parameter. We did a representative study in JH flows, to find the origin of these upstream propagating modes. For a very very small angle of divergence, 10^{-12} degrees, the flow is almost equal to that of a plane Poiseuille flow. For this case, all the modes in the global spectrum are downstream propagating. We find that gradually increasing the divergence angle will lead to the formation of a new branch, which has all modes upstream propagating. For a Reynolds number of 10, this new branch of the spectrum which has upstream propagating modes is seen to arise at a divergence angle of 0.5 degree. This study can be extended for different Reynolds numbers and the parameters corresponding to the origin of the upstream propagating branch can be determined. The comparison of the spectra obtained for increasing angles of divergence at a Reynolds number of 10 is shown in figure 3.40. The spectra obtained for very small angles of divergence are not shown in this figure as they are too stable at this Reynolds number (of 10). The new branch mentioned above is indicated with arrows in the figure and they can be seen clearly in the zoomed portion in the inset.

3.8 Summary

Global stability analysis is conducted on the simplest spatially developing flow one can construct, namely a channel of constant divergence, to show that the disturbances are not wave-like in the streamwise direction even in this similarity flow of constant Reynolds number. Given earlier global stability studies on boundary layers, where there is no qualitative difference between global modes and parallel or WNP modes, this result is unexpected. In fact, although many global studies exist on spatially developing flows, spatially extended but non-wave-like modes are not commonly seen. Not only therefore is a WKB-type approach inadequate to study such flows, the application of Robin boundary conditions, as is common in studies of this type, is inappropriate. More remarkable than the variation in streamwise length scale, which is not as expected from classical approaches, is the fact that energy-carrying scales are a function of the wall-normal direction, and that there can be several relevant length scales at one streamwise location. We hope that this work motivates studies aimed at a theoretical understanding of such

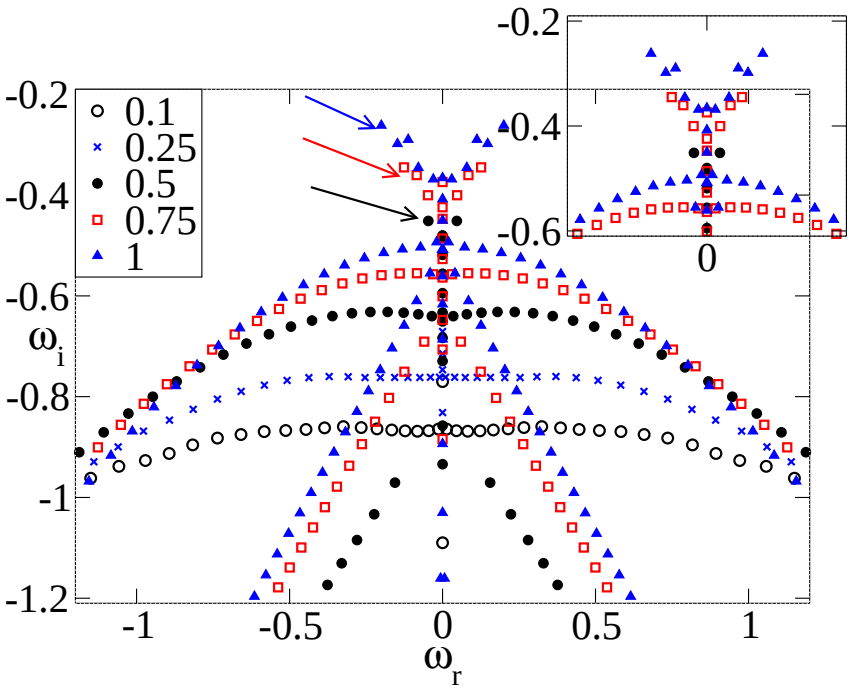

Figure 3.40: Global stability spectrum for increasing angles of divergence for JH flow at a Reynolds number of 10. The value of semi-diverging angles in degrees is given in the legend. A new branch consisting of the upstream propagating modes (indicated by arrows), is seen to appear for angles of divergence greater than (or equal to) 0.5 degrees. This can be seen clearly in the inset.

behavior, and also experiments which check these predictions.

CHAPTER 4

CONVERGING-DIVERGING CHANNELS

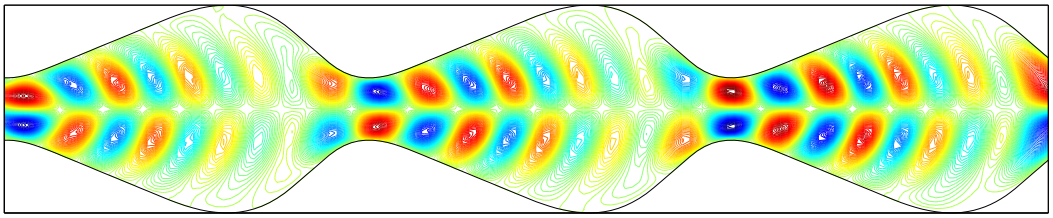

4.1 Introduction

In the previous chapter, we studied the effect of divergence alone in a channel flow. In contrast to the destabilizing effect of divergence, a convergence in a channel is known to stabilize flow through it. As seen in the last chapter the stabilization achieved is far greater than the destabilization of an equivalent divergence, see Banks *et al.* (1988), McAlpine & Drazin (1998). In this chapter, we study the effect of divergence and convergence acting simultaneously in a channel, and this makes it an interesting flow to study for two reasons (i) the net effect of their opposite stability characteristics is not a-priori obvious and (ii) a channel that is straight on an average with repeating coverging-diverging units is easy to construct for an experiment, compared to one that diverges over a long length scale. Such a series of alternating convergences and divergences, maintaining the average width of the channel a constant, is known to decrease the critical Reynolds number, Re_{crit}, significantly compared to a straight channel. These type of channels are studied extensively by many researchers, and the scope is two-fold. Works of the first category study small convergence and divergence amplitudes, with the aim of simulating the surface roughness of channel walls. This is because the wall of a channel, when zoomed down to sufficiently small scales, will typically be rough. The level of roughness will depend on the machining precision, and this roughness can be simulated realistically by an irregular series of local convergence and divergence. (Any man-made channel is rough, if seen from an appropriate scale). A sample is shown in figure 4.1. The second category of studies are on channels with relatively large angles of convergence and divergence with large amplitudes of wall waviness, which usually find large levels of

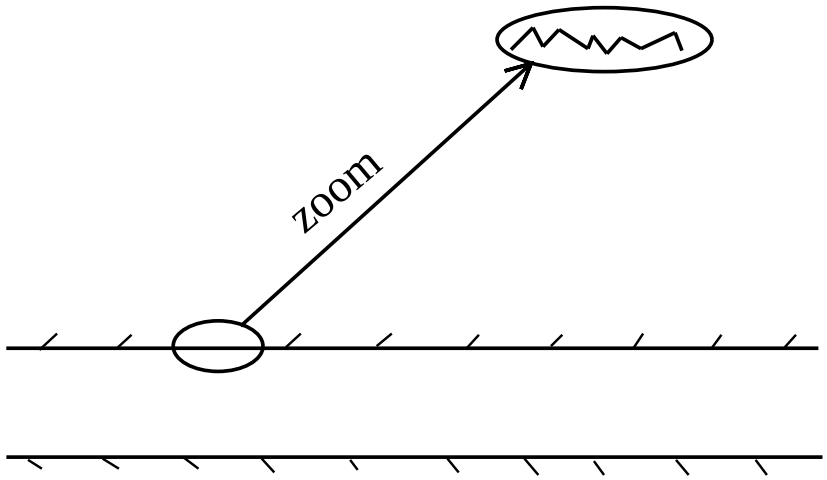

Figure 4.1: A sample real-world channel wall scaled sufficiently to show the surface roughness of the channel, which is determined by the machine precision.

destabilization. Such a situation is desirable when we want improved mixing - heat and mass transfer - e.g. in heat exchangers, chemical reactions, combustors, etc. The present work falls under this category. But the method developed (the generalized results), are not restricted to any range of wall-waviness amplitude. As there is no assumption in the basic derivation and the numerics applied, the present approach can easily be extended to study surface roughness effects. In fact, the results presented in this chapter, if extended to small amplitude converging-diverging channels, will explain in a better way the role played by the roughness of the channel walls in triggering transition. (Any man-made channel is rough, if seen from an appropriate scale).

As mentioned before, channels of constant average width with modulated wall geometry have a destabilizing effect. The geometry of channel wall can be modulated in many ways and there are many parameters involved. For example, consider the walls of two channels modulated using cosine waves, with phase differences of 0^o and 90^o between the top and bottom walls. These channels are called sinuous and varicose channels respectively, and are depicted in figure 4.2. Though the top and bottom walls of these channels have the same wavenumber, the two geometries have been shown to have different stability characteristis, see Blancher *et al.* (1994), Cho *et al.* (1998). Thus for the same wavenumber and amplitude, the stability characteristics of a channel can be modulated by the phase difference between the top and bottom walls. In addition to the wavenumber of the wall geometry, there is one more important parameter, which is the wall waviness amplitude, ϵ. This is defined here as the difference between the

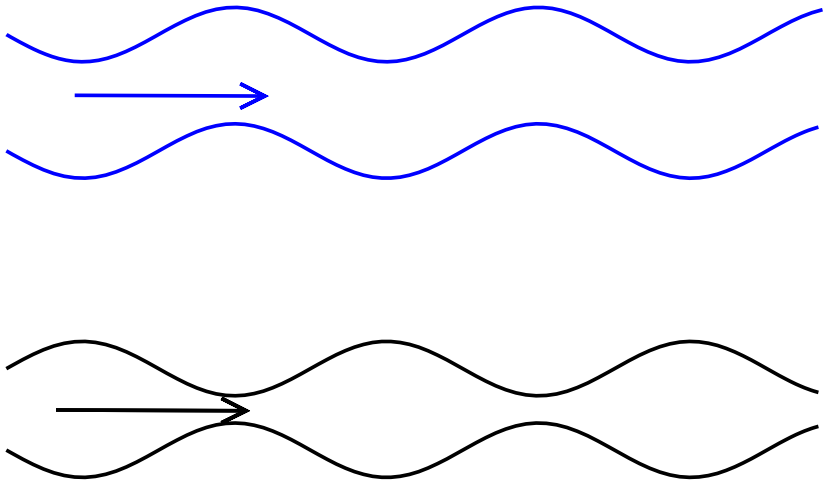

Figure 4.2: Comparison of a sinuous (top) and varicose (bottom) channel.

maximum and minumum half-widths of the channel, scaled by the minimum half-width of the channel. Floryan (2003) has shown, using a Floquet study, that the stability of varicose, fore-aft symmetric channels can be described by using just the two above mentioned parameters. Such a channel has both top-bottom and fore-aft symmetry. Fore-aft symmetry implies that the diverging region is an exact mirror image of the converging region. In the present work, we introduce fore-aft asymmetry in varicose channels and study its effect. The effect of fore-aft asymmetry in the wall goemetry was first studied, to our knowledge, by Sahu (2004). That study was on a pipe using a weakly non-parallel approach. It was shown that flow in one direction through such a geometry is more stable than flow in the reverse direction. Other studies on non-symmetric channels are those where arbitrarily shaped wall roughness is considered, such as in the significant body of work by Floryan and co-workers, discussed below. We study here the effect of fore-aft asymmetry in varicose channel flows using a global stability approach. One reason to choose a varicose channel is that, the base flow for such a channel can be obtained faster by exploiting the top-down symmetry. Details of the base flow calculation are given in section 4.2.

A brief overview of the previous work in converging-diverging channels is given below. The enormous body of work on surface roughness on channel walls are spared, with few a exceptions. In an experimental study at $\epsilon = 2.3$, Nishimura *et al.* (1984) reported a transition Reynolds number of 244. From a linear stability analysis using spectral-Galerkin method, Blancher *et al.* (1994), found that the wavelength of the most

unstable mode in a channel of $\epsilon = 2$ is the same as that of the geometry. They also studied the effect of a phase-difference between the upper and lower walls and showed that the critical Reynolds number Re_{crit} is smaller than that with no phase difference. A large reduction in Re_{crit} with wall waviness was also demonstrated in both varicose and sinuous channels by Cho *et al.* (1998). For two-dimensional disturbances, the finding is in accordance with that of Blancher *et al.*, i.e., the Re_{crit} for a varicose channel is found to be *smaller* than that in a sinuous channel. The reverse is true for three dimensional disturbances. Selvarajan *et al.* (1999) showed that the Re_{crit} reduces with increasing waviness amplitude ϵ, and also that laminar-turbulent transition can be delayed by suitable excitation of the wall. The existence of both traveling-wave instability in the form of Tollmien-Schlichting waves, and centrifugal instability in the form of streamwise vortices has been recognised by many authors, e.g., Cabal *et al.* (2002), Cho *et al.* (1998), Floryan (2003). Which of the two dominates is found to depend on ϵ. In the limit of ϵ tending to zero, i.e., as the geometry approaches a straight channel, traveling waves are the most unstable, consistent with Squire's theorem. Beyond a critical waviness amplitude of $\epsilon \sim 0.1$, instability is dominated by three-dimensional oscillatory modes, especially streamwise vortices, which are driven by centrifugal effects induced by the concavity of the wall. Critical parameters for such instabilities are discussed in detail by Floryan (2003). As ϵ is increased further, beyond $\epsilon \sim 0.3$, two-dimensional traveling waves are the most dominant again. Nishimura *et al.* (2003) studied expermentally the flow through an axisymmetric wavy-walled varicose pipe and made comparisons with that of a channel. They find that turbulent state occurs abruptly in a pipe and the heat and mass transfer characteristics are enhanced in a wavy-walled pipe compared to a channel.

It is shown by Floryan (2005) that a very good estimate of the Re_{crit} for two-dimensional instabilities may be obtained on a channel with distributed roughness on one wall, by representing the roughness geometry by its leading Fourier mode alone. He also shows that any shape of the wall roughness gives a similar level of destabilization, as long as the amplitude of waviness is maintained the same. He then extended this work to three-dimensional instabilities, Floryan (2007), and presented the critical conditions for the occurence of both traveling wave instability and vortex instability. One important aspect to note about the above mentioned two works of Floryan is that he has considered different shapes of corrugations. Here, the wall surface roughness is indicated as a sum of many Fourier modes, not necessarily a 'symmetric' goemetry. Since his study was interested in the effect of surface roughness, the wall waviness amplitude considered by

him is very small. He shows that the critical conditions are well captured by considering just one leading Fourier mode. A comparison of the critical parameters defining the onset of (2D) traveling wave instabilities and (3D) vortex instabilities for channels with both side wall corrugation, for small ϵ, is given recently by Floryan & Floryan (2010). In the above we have not covered work whose emphasis has been on heat and mass transfer characteristics. Out of the huge body of work on surface roughness, we have only mentioned a few as being the most relevant.

A concise representation of the earlier work discussed above is given in table 4.1. In the rows corresponding to Floquet theory, the periodicity length of the channel is indicated by a parameter α. This is the wavenumber of the channel wall geometry considered in the Floquet studies. The length of one periodic unit (L) and waviness the amplitude (ϵ) are scaled with the minimum half-width of the corresponding channels. The aspect ratio (AR) is defined as the ratio of the length of the channel to the maximum width of the channel.

The present work departs from earlier work in the following aspects. First, as already discussed, we allow for fore-aft asymmetry, this asymmetry will be seen to have a significant effect on the results. Second, in earlier studies, the same periodicity has been assumed for the disturbance as for the geometry. Even in the studies which found the disturbance wavenumber to be different from the periodicity wavenumber, the Floquet exponent is assumed to be real. These studies could thus give information about the temporal instability behaviour only and they were not able to reveal spatial growth characteristics. There is no apriori justification for a periodic assumption on the disturbance and we therefore do not make it. Thirdly, earlier work, with a few exceptions, was on small values of ϵ, highlighting the effects of surface roughness on channel flows. We look at large wall waviness, of up to $\epsilon = 2.3$, with the aim of achieving improved mixing at low Reynolds numbers. Finally, earlier work was either by a local stability analysis, a Floquet analysis, or numerical simulations. The appealing and computationally efficient approach of Floryan comes closest to a global stability study. That work however is at low ϵ, and the emphasis is on the progression within one geometric unit. For this purpose, it was sufficient to take the Floquet exponent to be real. The global stability study conducted here reveals features of the flow not easily accessible to the other approaches including that of Floryan, as we shall see. Due to these departures, we are able to reveal some interesting instability characteristics, and also obtain temporal global instability at

Table 4.1: Consolidated list of selected literature on converging-diverging channels
N - Number of periodic units.
L - Length of one periodic unit.
AR - Aspect Ratio.
DNS - Direct Numerical Simulations.

Author	**Year**	**Geometry**	**Method**	**N**	**L**	ϵ	**AR**
Symmetric							
Nishimura *et al.*	1984	Varicose channel	Experiments	9	9.33	2.3	1.4
Blancher *et al.*	1994	Sinuous channel	DNS	2	8	2	1.33
Cho *et al.*	1998	Varicose, Sinuous	DNS	1,2	3 to 4	0.27 to 2.34	0.4 to 1.57
Selvarajan *et al.*	1999	Varicose channel	Floquet	1	α = 0.2	0 to 1.5	6.28 to 15
Floryan	2003	Varicose channel	Floquet	1	α = 1 to 12	0 to 0.04	0.25 to 3.14
Nishimura *et al.*	2003	Varicose pipe	Experiments	13	9.33	2.3	1.4
Blancher & Creff	2004	Developing flow - Varicose channel	DNS	6 to 16	9.33	2.3	1.4
Floryan *et al.*	2010	Varicose channel	Floquet	1	α = 1 to 10	0.02	0.3 to 3
Non-symmetric							
Floryan	1997	Rough walled channel	Floquet	1	-	0.002 to 0.02	-
Cabal *et al.*	2002	Rough walled channel	Floquet	1	α = 1 to 6	0 to 0.06	0.5 to 3.14
Sahu	2004	Varicose pipe	WNP	1	50	0.5	16.6
Floryan	2005	One side rough wall channel	Floquet	1	α = 1 to 10	0 to 0.02	0.3 to 3.14
Floryan	2007	One side rough wall channel	Floquet	1	α = 1 to 16	0 to 0.016	0.2 to 3.14
Present		Varicose channel	Global	1,2,3	5,10	0 to 2.3	0.75 to 1.5

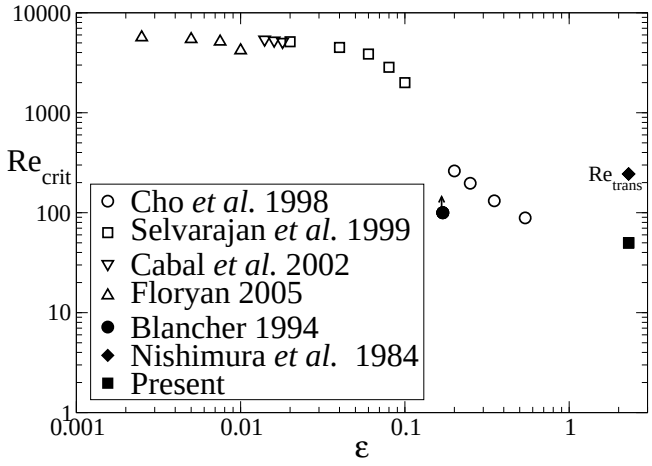

Figure 4.3: Variation of the critical Reynolds number Re_{crit} with the wall waviness amplitude ϵ in selected previous studies. Although different studies have used different aspect ratios and different wall shapes, a trend is observed. The present result shown by the solid square is discussed in section 4.4.

a lower Reynolds number, of about 50, as compared to the smallest critical Reynolds number of 85, based on present scales, quoted by earlier studies.

Before discussing present results, it is useful to compile the Re_{crit} obtained by various studies. The available values are shown in figure 4.3 as a function of the wall waviness amplitude ϵ. A consistent trend is visible among the results, although the geometries differ quite significantly in detail. In particular the aspect ratio, i.e. the length of a given periodic unit as compared to the average width of the channel, ranges from about 0.6 to 600. Different shapes of the walls have also been studied, like a sinusoidal wall, triangular grooved wall, evenly spaced bumps on the wall, etc. A trend is visible, where the Re_{crit} decreases with increase in the waviness amplitude. The present result is indicated but will be discussed later.

To mention a study on a related geometry, Ghaddar *et al.* (1986) performed direct numerical simulations on flow through channels with periodic grooves on one side, and showed that the least stable modes resemble Tollmien-Schlichting waves. These are forced by the shear layer formed between the central flow and the separated region in the grooves. Blancher & Creff (2004) showed through numerical simulations of the entry region of a symmetric wavy channel that beyond a certain Re_{crit} of about 100 for an ϵ of 2.3, the flow becomes spatially convectively unstable. Our study is different in that we study a fully developed periodic base flow and not developing profiles. Several studies have also been done on straight channels with a periodic array of cylinders to

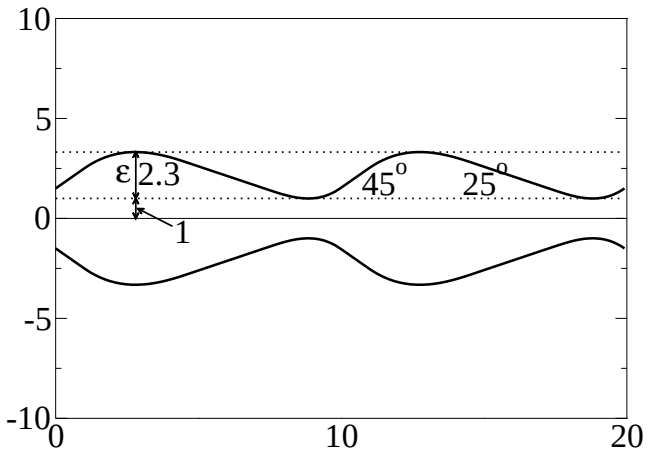

Figure 4.4: One of the non-symmetric channels under study. Divergence angle=$45°$, convergence angle = $-25.6°$. Ratio of diverging length to converging length is 4:6. Flow in this geometry from left to right is referred to as 'forward', as explained in figure 4.5.

achieve enhanced mixing at Reynolds numbers of the order of 100, e.g. by Karniadakis *et al.* (1922), Schatz *et al.* (1995) and Takaoka *et al.* (2009). In these flows, instability is triggered due to the cylinders acting as eddy-generators rather than by changing the geometry of the wall.

In a parallel flow, two-dimensional perturbations would be the most unstable, in accordance with Squire's theorem. This theorem is not valid for a non-parallel flow, but going by Cho *et al.* (1998) which shows that two-dimensional disturbances are dominant beyond $\epsilon = 0.3$, we restrict ourselves to two-dimensional disturbances. Three-dimensional disturbances, a subject of present investigations, may well prove to be faster growing, both exponentially and algebraically, but the proof of principle is already achieved with two-dimenionsional disturbances.

Even in flows where there is an exponential growth of perturbations, transient algebraic growth can sometimes be rapid enough to trigger nonlinearities and therefore to dictate dynamics. Szumbarski & Floryan (2006) studied the transient growth associated with channels with wall corrugations and calculated the maximum growth and optimal perturbations for different corrugations. Perturbations which are optimal for a smooth channel are found to be the most amplified by the wall corrugation. Even at a Reynolds number of 10, we show that random combinations of two-dimensional eigenmodes can give rise to spatially localised pockets of large transient growth, even though the kinetic energy when integrated over the entire domain is monotonically decaying. Since such

pockets of large disturbance growth are sufficient to change the dynamics, it is argued that transient growth in such flows needs to be characterised on a local basis rather than by an integrated quantity such as the commonly used G_{max}.

4.2 Base Flow

4.2.1 Parameters

As mentioned before, we study both symmetric and fore-aft asymmetric varicose channels. The mean flow is calculated numerically for each case. The walls of the symmetric channels are defined by cosine functions. One of the asymmetric channels studied is shown in figure 4.4, where we see two identical diverging-converging units in series. Each unit consists of a straight diverging portion followed by a straight converging portion, with different lengths for the converging and diverging regions. For the case mentioned above, the ratio of the diverging and converging lengths is [4 : 6]. To avoid sharp corners, the two are connected on either side by smooth cubic polynomials over short regions. Unless otherwise specified, the length of each repeating unit of the channel is $L = 9.9585$, which is about 5 times the minimum width of the channel. Besides these choices of length-to-width and divergence-length to convergence-length ratios, we need to make a choice on the amplitude of the wall waviness, ϵ. As shown in the figure 4.4, ϵ is the difference in the maximum and minimum half-widths scaled by the minimum half-width of the channel. We study a range of ϵ, varying between 0.01 and 2.3. The largest waviness among these is termed our 'standard' geometry, which we study in some detail (figure 4.4 with ϵ 2.3). For contrast, we also study a channel with a more accentuated asymmetry, where the ratio of diverging length to converging length is [3.4 : 6.6]. In addition, we study channels whose aspect ratio is halved, i.e., the same waviness shape and amplitude as in the standard case is prescribed over half the streamwise extent, making each unit blunter. Finally we study a channel in which the corruagation is present in only one of the walls, while the other is straight. We prescribe Reynolds numbers in the range of 1 - 100. For comparison, we study channels with one, two and three consecutive converging-diverging units in series, but lay greater emphasis on the two-unit case.

In a non-symmetric channel, the dynamics could depend on the flow direction. The terminology we employ is shown in figure 4.5. When the diverging section is shorter we term it 'forward' flow, and flow in the other direction is termed 'reverse' flow. Thus

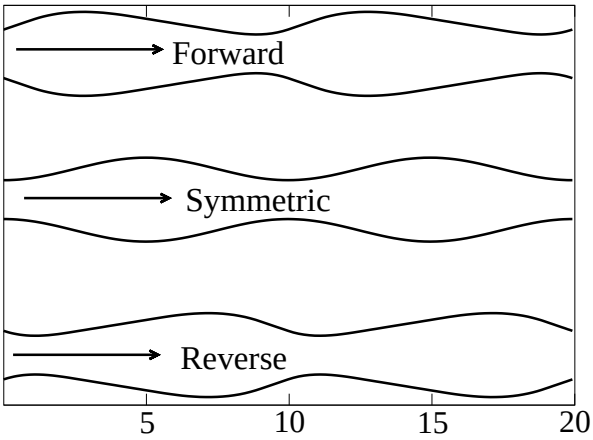

Figure 4.5: The asymmetric and symmetric geometries studied. The diverging length is different from the converging length for an asymmetric channel, whereas the symmetric channel is defined by a cosine function. The flow direction is indicated by the arrow.

for the standard geometry discussed above, the ratio of diverging length to converging length is 4:6 in the forward unit and 6:4 in the reverse unit.

4.2.2 Numerical Scheme

The base flow is computed for a single diverging-converging unit, and repeated over each unit. The steady two-dimensional Navier-Stokes equations are solved in the streamfunction-vorticity formulation. This can become very time consuming, so a full multigrid technique is used to accelerate the convergence, and a fast parallel solver is incorporated, details of which are available in Venkatesh *et al.* (2006). The governing dimensionless equations are

$$\frac{\partial \Omega}{\partial t} + (\vec{U}.\nabla)\Omega = \frac{1}{Re}\nabla^2\Omega \qquad \Omega = -\nabla^2\psi,$$

where $\vec{U}$ is the velocity vector, t is time, and Ω and ψ are the mean vorticity and streamfunction respectively. The Reynolds number Re is based on the minimum half-width of the channel, and the centerline velocity at the minimum half-width. The solution is facilitated by a transformation of coordinate, defined by $d\zeta = dx/H(x)$, and $\eta = y/H(x)$, where H is the local half-width. Symmetry boundary conditions $\psi = \Omega = V = \partial U/\partial y = 0$ are used at the centerline; no-slip and impermeability boundary conditions, $U = V = 0$, are imposed at the wall; and periodic boundary conditions at the

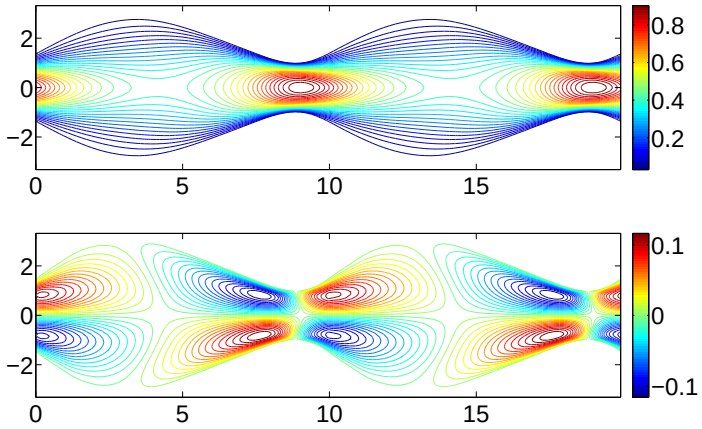

Figure 4.6: Contours of streamwise (top) and wall-normal (bottom) velocities of the base flow obtained from numerical simulations, for the parameter setting shown in figure 4.4, at a Reynolds number of 10.

inlet and the exit. We begin with a guess solution: a parabolic velocity profile at every axial location, and march in psuedo-time until a steady-state solution is obtained. The vorticity distribution at each new time step is calculated adopting first-order accurate forward differencing in time and second-order accurate central differencing in space, on a 66×514 grid. This vorticity distribution is used to solve the Poisson equation for the streamfunction by a Jacobi iterative scheme. Numerical acceleration is achieved by a six level full-multigrid technique. The procedure is repeated until the cumulative change in vorticity reduces to below 10^{-8}. A typical contour of the streamwise and wallnormal velocities of the flow through the domain shown in figure 4.4 at a Reynolds number of 10, is given in figure 4.6. As can be discerned, the flow in this case is close to separation at the turn from diverging to converging. The base flow for this particular parametric setting shows regions of separation for Reynolds numbers greater than 10. The contours of the streamwise and wall-normal velocities for a Reynolds number of 50 are shown in figure 4.7. The local velocity profiles at few x locations are shown in figure 4.8, which clearly shows the regions of separation near the maximum channel width.

4.3 Global Stability Analysis

Since the wall boundary of this geometry is non-uniform, for easy satisfaction of the boundary conditions, the global stability equation (eqn 2.16) is expressed in the x-η

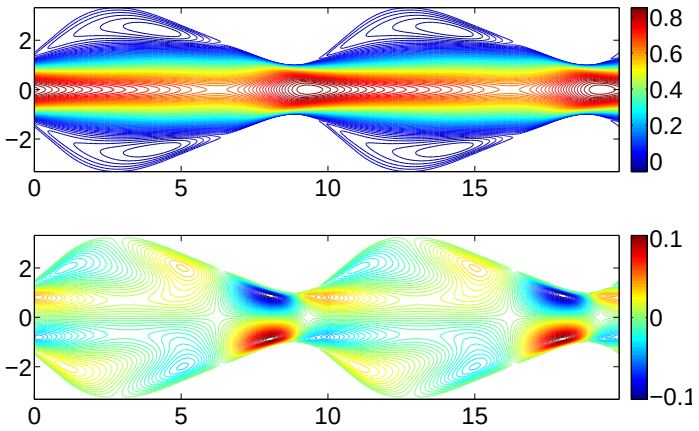

Figure 4.7: Contours of streamwise (top) and wall-normal (bottom) velocities for flow through the standard geometry at a Reynolds number of 50. As can be seen, this flow shows a separated region near the maximum channel width region. The separation is weak as can be seen from the very low negative values of U, shown in the colour-bar of the top figure.

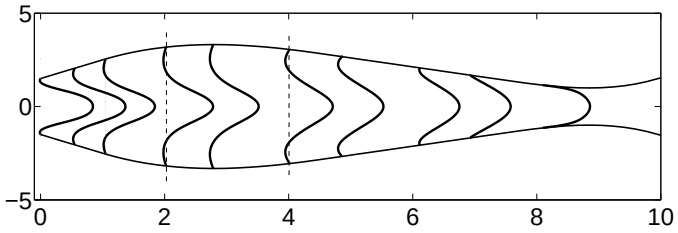

Figure 4.8: Local velocity profiles of the base flow for the standard geometry at a Reynolds number of 50, same as figure 4.7. The weak separation of the profiles can be discerned. Figure not to scale.

plane. The equation is discretized with Chebyshev spectral collocation points in both spatial directions, with n points in the x direction and m points in the y direction. Since this clusters the grid points close to the inlet and exit of the domain, which is undesirable, a suitable stretching function is used in x, which is explained in section 2.6.4. The values of the stretching constans are fixed to be $a = 0.5, b = 3.0$. In the wall-normal direction, it is desirable to have clustering close to the wall, and this comes out naturally using Chebyshev spectral discretization. A typical grid on an asymmetric geometry is shown in figure 4.9. The maximum grid size studied is 121×161. No-slip and no-penetration boundary conditions are used in the wall-normal direction. Extrapolated boundary conditions are used in the streamwise direction. We also study a few cases

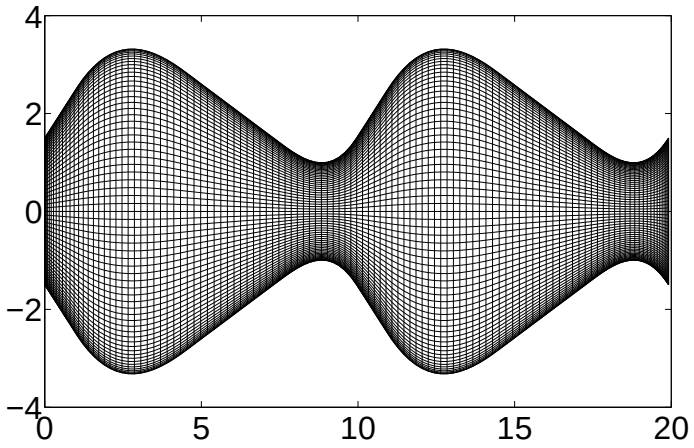

Figure 4.9: A typical grid used for the global stability study; grid size is 119x65.

with periodic boundary conditions in streamwise direction, for the sake of comparison.

4.4 Results

As mentioned before, a variety of parameters are studied and a consolidated list of the different cases studied is given in Table 4.2. Each case has been computed using different grid sizes and in each case it is ensured that a reasonably grid-insensitive result is obtained. A reliable grid size is indicated in the table. In the following three subsections, we discuss results from the asymmetric forward case, asymmetric reverse case and the symmetric case individually and then in the fourth subsection we make a comparison of the three cases.

4.4.1 The 'standard' geometry

Given the number of parameters, it is useful to define one particular geometry as our standard, and make all comparisons with reference to this. Our standard case, as mentioned above, is a non-symmetric geometry, of divergence to convergence ratio $4:6$, $\epsilon = 2.3$ and aspect ratio close to 10, with forward flow. We start with a single standard converging-diverging unit and obtain global modes. Periodic boundary conditions

Table 4.2: Consolidated list of the various parameters studied

The short form Fwd stands for Forward, Rev for Reverse and Symm for Symmetric. The cases described as 'neutral', are in a near-neutral situation, with the growth rate of the least stable eigenmode negative, but within 10^{-3} of zero. Also, in column 2, unit lengths indicated as 10 and 5 respectively are actually of lengths 9.9585 and 4.97925.

Corrugation	Unit Length	No of Units	ϵ	Ratio of Div:Conv [Fwd/Rev/Symm]	Re	Grid Size	Results
Both Sides	10	1	2.3	Fwd [4 : 6]	10	101x65	Stable
				Rev [6 : 4]	10	101x65	Stable
				Symm [5 : 5]	10	101x65	Stable
		2	2.3	Fwd [4 : 6]	1	119x65	Stable
					10	119x65	Stable
					20	161x61	Stable
					30	121x141	Stable
					50	121x161	**Neutral**
					100	121x161	**Unstable**
				Rev [6 : 4]	10	281x61	Stable
					30	91x171	Stable
					50	111x121	**Neutral**
					80	121x121	**Unstable**
					100	121x121	**Unstable**
				Symm [5 : 5]	10	119x65	Stable
					30	119x85	Stable
					50	119x101	Stable
				Fwd [3.4 : 6.6]	10	221x65	Stable
			0.5	Fwd [4.6 : 5.4]	10	119x65	Stable
			0.2	Fwd [4 : 6]	10	115x65	Stable
					50	221x45	Stable
			0, 0.01, 0.1, 0.2, 2.0	Symm [5 : 5]	10	many	Stable
		3	2.3	Fwd [4 : 6]	10	181x65	Stable
				Rev [6 : 4]	10	181x65	Stable
				Symm [5 : 5]	10	181x65	Stable
	5	2	0.1	Symm [2.5 : 2.5]	10	61x51	Stable
					30	61x51	Stable
			0.5	Symm[2.5 : 2.5]	10	61x51	Stable
					50	61x51	Stable
One side	10	2	2.3	Fwd [4 : 6]	30	119x75	Stable
					50	101x91	Stable
					80	81x101	Stable
				Rev [6 : 4]	30	119x65	Stable
					50	111x75	Stable
					80	111x95	**Unstable**

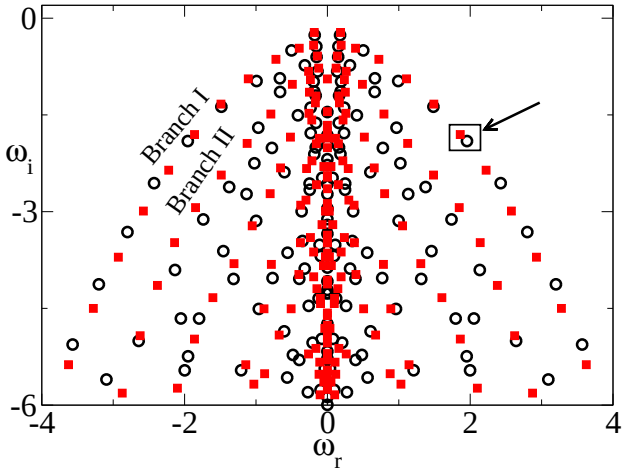

Figure 4.10: Spectra obtained for our standard geometry with a single unit, at a Reynolds number of 10. Hollow symbols - with periodic boundary conditions, filled symbols - with extrapolated boundary conditions.

(PBC) in the streamwise direction are applied in the first computation, since many earlier numerical simulations have done the same. We next apply extrapolated boundary conditions (EBC) in the streamwise direction. A comparison of the spectra obtained in each case at a Reynolds number of 10 is given in figure 4.10. It is immediately apparent that the spectrum has several distinct branches. We term the upper two as branches I and II. Contours of two corresponding modes within a box indicated by the arrow are shown in figure 4.11. Plotted here are the contours of the streamwise disturbance velocity. We see that with either set of streamwise boundary conditions, the spectra are qualitatively the same, with the main branches showing similar eigenstructure.

Based on the periodicity of the geometry, one might intuitively expect the same eigenstructure to repeat itself in each unit if we had many converging-diverging units in series. Instead, if we do not make this assumption, and conduct a global stability study spanning several units, there is a qualitative change in the results. In particular, we find that instability ratchets are possible, where a given mode becomes sequentially stronger or weaker in every subsequent periodic unit. As often done in recent times, the term ratchet is used here in analogy with a mechanical ratchet. In a mechanical ratchet, for example in a hand pump, a periodic motion of the arm results in sequential increase in the water level. Similarly in our flow, a periodic geometry results in sequential increase in the amplitude of the disturbance energy. Note that the spatial growth is displayed by a single global eigenmode. This is not a transient growth phenomenon. Going by

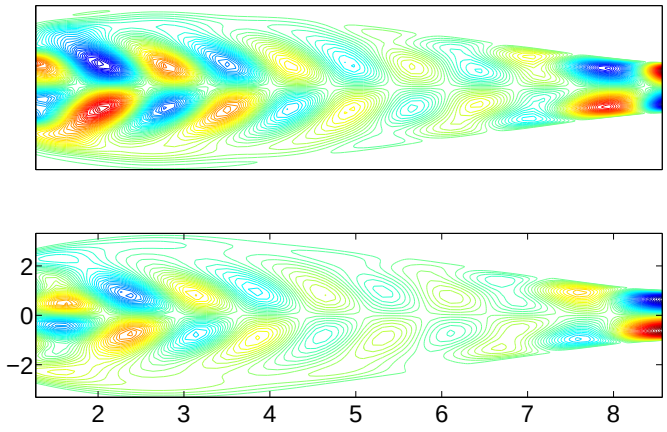

Figure 4.11: Contours of streamwise disturbance velocity of a typical mode chosen from Branch I (shown with an arrow in figure 4.10). Top - periodic boundary condition; bottom - extrapolated boundary condition.

parallel stability results, a given convergence is far more stabilizing than a divergence of the same angle. So a progressive decrease in amplitude over successive units is not surprising, whereas a sequential growth is non-intuitive. As explained above, we term this progressive growth an instability ratchet. To obtain modes displaying such behaviour, we use periodic boundary conditions no further and use only the EBC hereafter. While the EBC may not be completely faithful to reality, they are probably the least likely to bring in extraneous physics. This statement is supported by figure 4.12, where the entire spectrum obtained for the PBC and EBC cases shown in figure 4.10 are shown. We can see that the imposition of PBC gives rise to many modes which are spurious artifacts of an unphysically stringent boundary condition. On the other hand, the spectrum obtained with EBC looks very clean.

In a few of the figures to follow, the regions immediately close to the inlet and exit of the domain are not shown. This is because the disturbance amplitude is extremely high at these locations, probably an artefact of the EBC. To ensure that these boundary conditions do not in fact colour the results, ideally one would like to use a geometry in which a large number of repeating units are connected in series, but due to computational time and memory constraints, we consider only two or three repeating geometrical units. Multiple units play a more crucial role in this study than merely checking the goodness of the boundary conditions: we need to use more than one unit since we are interested in obtaining sequential spatial growth. A comparison of the spectra of the standard

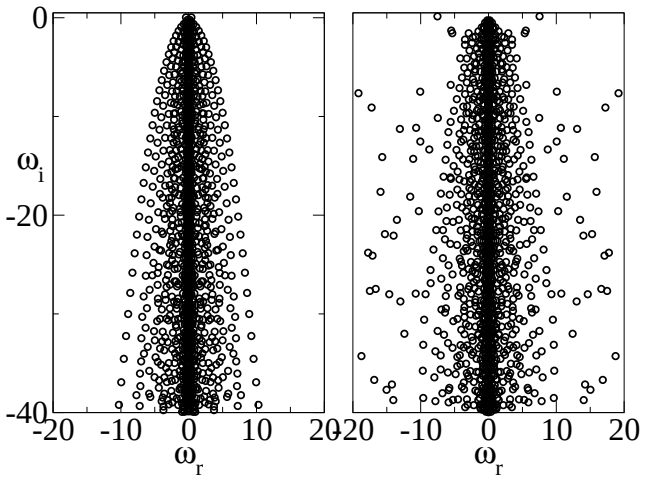

Figure 4.12: Eigenspectrum obtained for the cases shown in figure 4.10; left: with EBC and right: with periodic boundary conditions. We can see that the main structure of the spectrum is identical with periodic boundary conditions. However, the PBC produces many spurious modes in addition.

geometry using one, two and three units is shown in figure 4.13. The main branches of eigenvalues are insensitive to the number of units employed. However, an interesting pattern is seen, for example in branch I, as shown in the zoomed portion of the spectrum in the inset of figure 4.13. Each eigenvalue in the single unit case is replaced by two and three eigenvalues in the two and three unit cases respectively. Each set shown thus contains six modes. This trend is seen in all the branches of the spectrum.

We choose two sets of modes, one each from branches I and II, to discuss further. For reference, the modes are numbered 1-6 within each set. In figure 4.14 we examine the streamwise velocity structure of a set of modes from Branch I. The structure within one unit appears similar qualitatively in all modes of the set, and its notable feature is the spatial variation in amplitude within it. A traditional stability analysis assuming the flow to be locally parallel, or weakly non-parallel predicts that while the diverging region is destabilising, the converging region stabilises the disturbances to a far greater degree, so the maximum in amplitude would be close to the widest portion. The global stability makes a different prediction. Figure 4.14 shows that the amplitude of this set of modes peaks within the converging region. There also exist modes whose maximum energy is either in the minimum width region or in the diverging region (shown later in figure 4.23). This is one example of the physics revealed by global stability studies.

We now discuss the variation between units. If we were to extend the parallel or

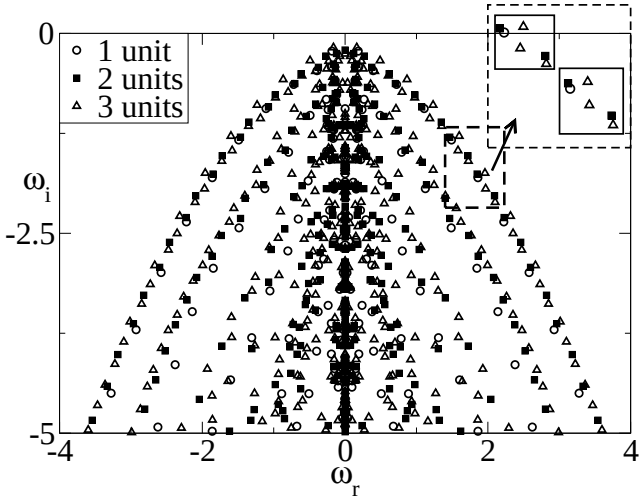

Figure 4.13: Eigenspectra of flow through the standard geometry at a Reynolds number of 10, with one, two and three periodic units. The inset zooms in on a part of branch I, revealing that each mode in the single unit case is replaced by 2 and 3 modes in the 2 and 3 units cases, respectively.

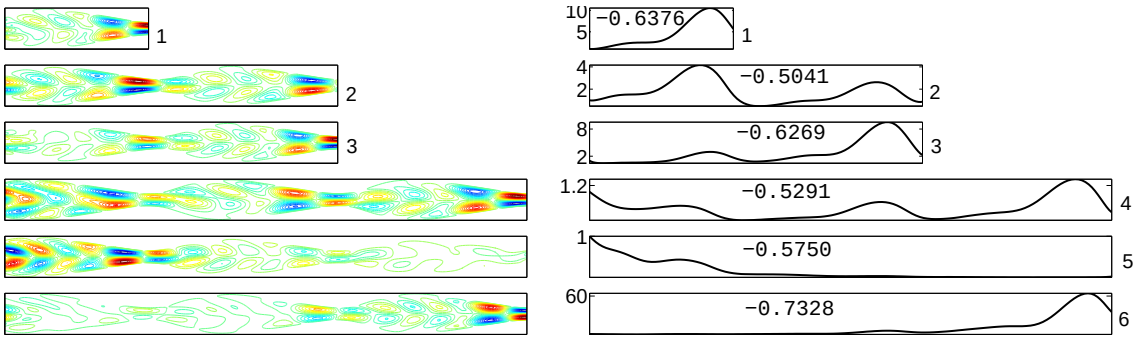

Figure 4.14: (Left) Contours of streamwise velocity of a set of modes from branch I, shown in figure 4.13. (Right) Energy of the modes. The numbers within each figure indicate the temporal decay rate (ω_i) of the mode.

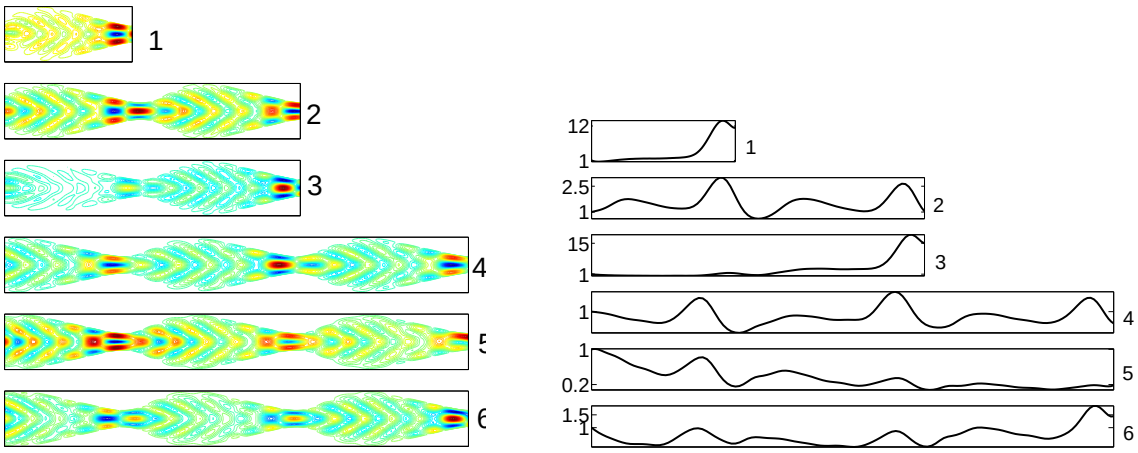

Figure 4.15: (Left) Contours of streamwise velocity of a set of modes from branch II, shown in figure 4.13. (Right) Energy of the modes.

weakly non-parallel analysis over multiple units, the fact that convergence is far more stabilising under that assumption than divergence is destabilising, means that at the exit of one periodic unit of the geometry, all disturbances would have decayed relative to their amplitude at the entrance of that unit. Thus over successive units all disturbances would die out. This is the case for a variety of shapes of channels (Sahu, private communication) for much higher Reynolds numbers than considered here. Revealed by the global analysis, however, are several disturbance modes which are stronger in each unit than in the previous one. There are several possibilities apparent for spatial development. Broadly, each mode from the single unit case is replaced, in the multiple unit cases, by modes displaying sequential spatial decay (modes 2 and 5), spatial growth (modes 3 and 6), or even nonmonotonic behaviour (mode 4). The spatial growth or decay of these modes is quantified by plotting the energy of these modes, shown to the right of figure 4.14. Each of the energy plots is scaled by its inlet energy. Modes 3 and 6 are seen to exhibit an instability ratchet in space. We can see that the streamwise velocity contours give a good idea of the growing or decaying trend of the kinetic energy of the modes. Noticing that the spatial growth is rather accentuated in the three unit case as compared to the two-unit, we surmise that geometries with many units in series hold the possibility of large spatial growth. Another example of such spatial variety is evident in figure 4.15 which shows a set of sample modes from Branch II (left) and their energy (right). In all our computations, modes in the lower branches have a much finer structure than in the higher ones. One consequence of this comparison is that we realise that qualitative

stability characteristics are reasonably well captured by just two units in series.

4.4.2 The instability ratchet

In this subsection, we discuss the instability ratchet in detail. The first question which arises is, why did previous studies not report the existence of instability ratchets in these channels? The answer is two-fold, (i) many works were limited to just one periodic unit and hence were not able to capture this growth 'across units'. (ii) the Floquet analysis conducted by Floryan and other workers prescribed the Floquet exponent to be a real quantity. This in effect ensured that the disturbance would be periodic over successive units. and hence assumed. If the Floquet exponent is complex, then the imaginary part of it contains the ratchet growth/decay (as has been explained in the next paragraph). Floquet theory is generally used for time-periodic flows. Here we use it to study the space-periodic base flow.

Consider the advective terms of the global stability of a model 1D flow,

$$\hat{u}\frac{\partial U}{\partial x} + U\frac{\partial \hat{u}}{\partial x}. \tag{4.1}$$

These terms represent the interaction of the perturbations with the base flow. Let the space-periodic base flow be assumed to have a periodicity of β as, $U = Re\{be^{i\beta x}\}$. If the disturbance is wave-like, it can be represented as, $\hat{u} = Re\{ae^{i\alpha x}\}$. Re means real part, a and b are complex magnitude functions, β is real, and α is assumed complex, so that α_i gives the spatial growth/decay rate of the disturbance. If we put $\alpha = n\beta$, then equation 4.1 becomes,

$$\begin{aligned}\hat{u}\frac{\partial U}{\partial x} + U\frac{\partial \hat{u}}{\partial x} = e^{\alpha_i x}\big\{&(n+1)i\beta[abe^{i(n+1)\beta x} - a^*b^*e^{-i(n+1)\beta x}]+\\ &(n-1)i\beta[ab^*e^{i(n-1)\beta x} - a^*be^{i(-n+1)\beta x}]-\\ &\alpha_i[abe^{i(n+1)\beta x} + a^*b^*e^{-i(n+1)\beta x} + ab^*e^{i(n-1)\beta x} + a^*be^{i(-n+1)\beta x}]\big\}.\end{aligned}$$

Integrating over an integer multiple length of $2\pi/\beta$, we get a contribution for α_i as,

$$\alpha_i = \frac{C}{e^{\alpha_i x}[a^*b + ab^*]} \qquad n = 1 \tag{4.2}$$

$$\alpha_i = 0 \qquad n \neq 1 \tag{4.3}$$

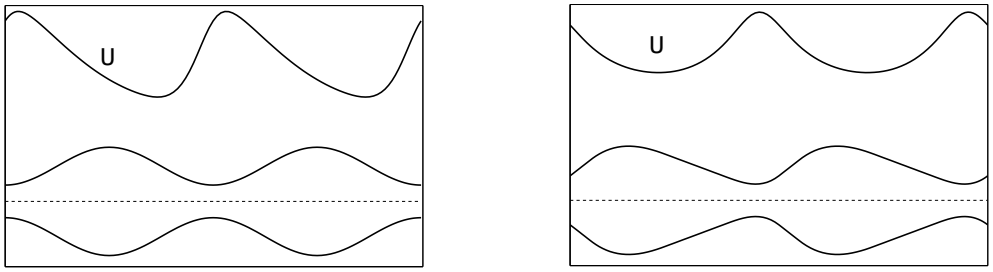

Figure 4.16: (Left) Variation of centerline velocity (solid line on top) for a symmetric geometry (shown below) at a Reynolds number 10. Even though the geometry is defined by a cosine wave, the base velocity variation is not a simple wave. (Right) Same as the left figure, but for the standard geometry. Note that these figures are not to scale.

Here C includes all the terms of the stability equation other than the terms in equation 4.1. Equations 4.2 and 4.3 state that there can be either growth or decay over successive units, if the disturbance wavenumber matches with the base flow's wavenumber (n=1). The variation of the centerline velocity at a Reynolds number of 10, both for symmetric and asymmetric channels are shown in figure 4.16. The boundaries of the geometry are also shown for comparison. In the symmetric geometry studied, even though the geometry is defined by a cosine function, the base flow (computed from numerical simulations) is not a pure sinusoid, as seen in the left of figure 4.16. But since it is periodic, it can be written as a combination of many Fourier modes. Thus, according to equation 4.2, if the wavenumber of the disturbance mode is equal to any one of these Fourier modes, there is a possibility for ratchet growth or decay. The same holds good for the asymmetric channels also, shown on the right of figure 4.16.

The ratchet mechanism must be interpreted with caution. In most of the modes, when integrated over the entire domain there is no, or only negative, energy input from the basic flow to the disturbance. In fact a given mode can be made to re-appear as another one with a greater temporal decay compensated by a greater spatial growth. This aspect is just discussed above. However, the spatial growth is still significant, from the point of view of the higher possibility of triggering nonlinearities in the downstream units compared to upstream ones, and also the increased transient growth possible downstream.

4.4.3 Spatio-temporal interplay

The global approach allows for a rich range of apportionment of growth and decay into the spatial and the temporal. By the term spatial growth, we refer here to the growth from one unit as a whole to the next. A given mode can manifest itself in many ways, since a decrease in temporal growth rate, for example, can be compensated by an increase in spatial growth rate. By increasing the number of computational repeating units from 1 to 3, we obtain three manifestations of a given mode in the place of 1. This can be verified from figure 4.14, where corresponding temporal decay rates are also given. It can be seen that temporally less stable modes exhibit sequential decay and temporally more stable modes exhibit sequential growth. Another manifestation of the possibilities in spatio-temporal apportionment is evident in figure 4.17, where the spectra obtained for different Reynolds numbers of our standard geometry with two repeating units are shown. For clarity, only the outer-most branch is shown. It can be noticed that the branch bifurcates into two sub-branches near the imaginary axis, and this division is more pronounced for higher Reynolds numbers. Of the two sub-branches, the higher one, being of less negative ω_i, decays more slowly temporally compared to the lower one. But their spatial stability characteristics are interchanged, such that the upper sub-branch modes are spatially decaying and the lower sub-branch modes are spatially growing. Two typical pairs of modes from the upper and lower sub-branches for a Reynolds number of 10 which display this interchange are shown in figure 4.18. Another interesting feature: in contrast to straight channel flows, where usually an individual mode becomes more unstable with increase in Reynolds number, in converging-diverging channel flows, we see an entire branch of the spectrum becoming flatter and closer to neutrality. This could provide scope for high transient growth, as discussed later.

4.4.4 Numerical Floquet study and its limitations

Since the base flow has the same periodicity as that of one geometric unit, a simpler model study has been be conducted where the spatial growth achieved in each unit is expressed by a Floquet multiplier. The wavelet analysis below will demonstrate why this description is only a simplified model, since the real disturbance growth or decay is far from completely described by one scalar multiplier. To confirm that there is an interplay between the temporal and spatial stability characteristics of the global modes, we perform the following computation on the standard geometry with one geometric

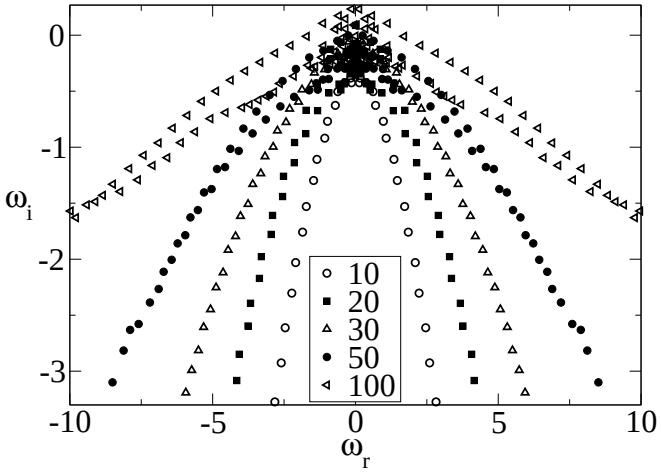

Figure 4.17: Spectra obtained at different Reynolds numbers for the standard geometry with two periodic units. Many modes become near-neutral with increase in Reynolds number, which could lead to interesting transient growth behaviour. For clarity, only the least stable branch of the spectrum is shown.

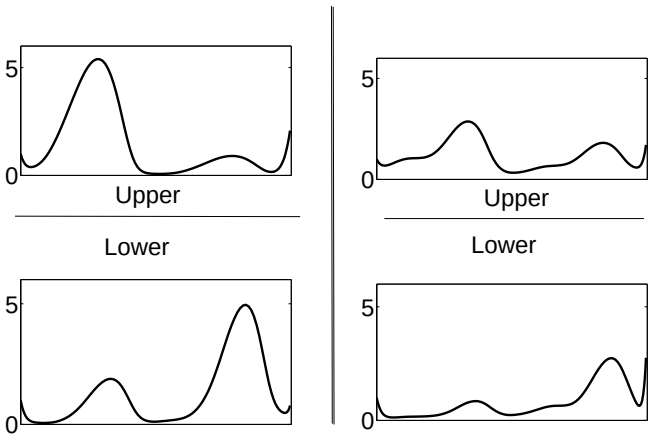

Figure 4.18: Energies of two typical pairs of modes from branch I which splits into two sub-branches. The modes from the upper sub-branch are temporally more unstable but spatially more stable than those from the lower sub-branch.

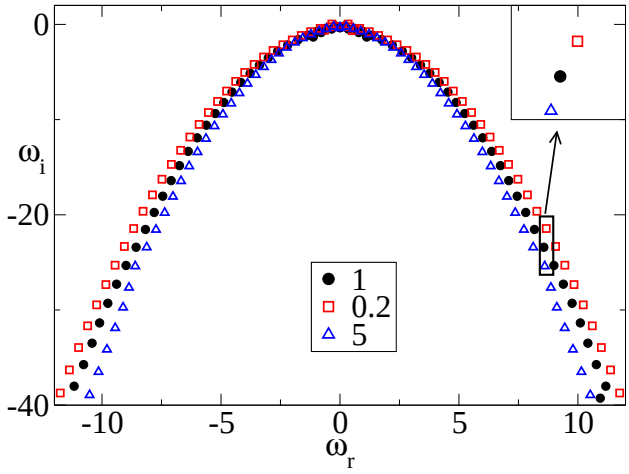

Figure 4.19: Spectra with boundary conditions simulating a desired Floquet multiplier, in a single unit standard geometry at a Reynolds number of 10. The exit boundary values are specified as a constant multiple of the inlet values, and the values of the constant are given in the inset. A constant less than, greater than and equal to one implies a spatial decay, spatial growth and periodic boundary conditions, respectively.

unit. We enforce a desired Floquet exponent by specifying the exit values as a given multiple of the inlet values, and see the change in ω_i. For a sequential spatial growth, the Floquet exponent must be greater than 1, and vice-versa. A value of 1 implies periodic boundary conditions. The comparison of the spectra obtained for different exponents at a Reynolds number of 10 are shown in figure 4.19. Here again, only the least stable branches of the spectra are shown for ease of viewing. It can be seen that when the modes are forced to exhibit a spatial decay, they become temporally less stable than when there is forced spatial growth. This is more evident in the inset shown in the figure, which shows the change in the temporal growth rate (ω_i) of the modes for a given frequency.

In local stability studies, the mode is always assumed to sustain a wave-like structure in the streamwise direction. We now ask the question, how wave-like are the global modes? A visual examination seems to suggest a wave-like structure in some regions, but with an effective wavenumber that seems to vary in both streamwise and normal directions. A quantitative estimate of the local length scale can be obtained by performing a wavelet transform of the amplitude of a mode plotted along a prescribed path. Wavelet transform has been performed on the global modes of diverging channels in the previous chapter and they are explained in detail in section 3.6.5 of chapter 3. Here we choose to study the x-variation of a mode at a given fraction of the channel width. The amplitude of the wavelet transform indicates the contribution to each length scale of a mode at a

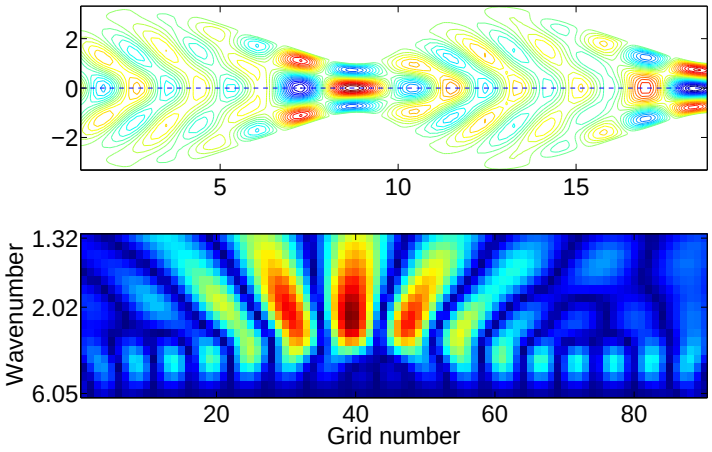

Figure 4.20: Top: Streamwise velocity contours of a typcial mode; Bottom: Wavelet transform at the wall-normal location indicated by the blue-dashed line. As visible, the modes have larger lengthscales near the converging region of the channel.

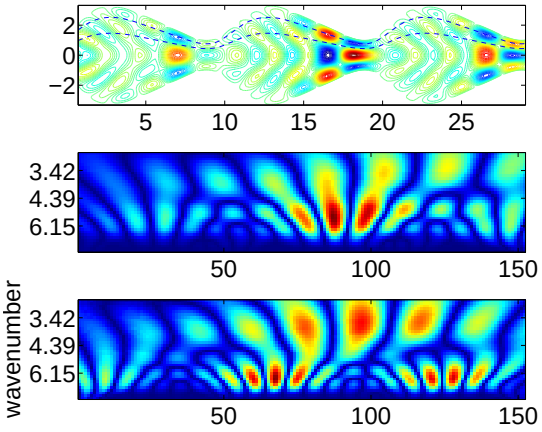

Figure 4.21: Similar to figure 4.20, but the wavelet transform is presented at two different wall-normal locations. The middle figure shows that close to the wall, the dominant lengthscale changes weakly from unit to unit. The bottom figure shows that closer to the centerline, at a given streamwise station, in addition to the dominant lengthscale, we may have sub-sominant lengthscales. The dominant scales in the two figures are different.

given location within the channel, so that the brightest spot at a given streamwise station indicates the dominant 'wavenumber' at that location. In the context of wavelets, we use the term wavenumber to indicate the inverse of the dominant length scale. Morl wavelet has been used in the results presented here, but the answers are not sensitive to the specific choice. A wavelet transform of a typical mode is shown in figure 4.20. The reader is reminded that in all plots of wavelets, it is useful to focus our attention on the central part of the figure, since a small region at each side of a wavelet transform plot is known not to be accurate. Plotted at the top are the contours of streamwise velocity of a typical mode of our standard geometry. Below this is plotted the wavelet transform of the mode along the blue-dashed line. Even by visual examination, we can say that the mode displays larger lengthscales towards the converging region. The corresponding region in the wavelet transform thus shows a smaller wavenumber. This shows that the wavenumber of a mode changes with streamwise distance. Next, we perform wavelet transform of a typical mode from the three-unit case at two different wall-normal locations, shown in figure 4.21. Here, wavelet transform is performed at two different wall-normal locations, indicated by the blue-dashed lines. It can be seen from the middle plot that the wavenumber changes weakly from unit to unit. From the bottom plot, it is evident that closer to the centerline, there can exist more than one dominant lengthscale at a given streamwise station. By examining the spatial behaviour in these plots, we may conclude that the wavelength is a function of both x and y. Such behaviour is also seen in wall jets to a limited extent and in divergeing channels. Moreover in the present flow, the growth behaviour too can differ for different wall normal locations, and even at a given wall normal location, can differ for different length scales. This shows that a simplified treatment by Floquet theory would not afford a complete description of the physics. In effect, the Floquet multiplier can be a function of y, and also be different for the different dominant scales even at a given y! Thus the kinetic energy, integrated across the channel, can vary in interesting ways from one unit to another and not be described by a single Floquet exponent.

The interchange of the spatial and temporal stability characteristics of these global modes reminds us of Gaster (1962)'s transformation between temporal and spatial growth. But the spatio-temporal interplay cannot be explained using Gaster's transformation because of the following two reasons: First, as just explained, the spatial growth behaviour of these modes cannot be described by a single Floquet exponent. And hence the spatial stability characteristics cannot be transformed into temporal stability characteristics.

Second, the spatial growth that we discuss here is not the local spatial growth but the growth of the modes 'across units'. A Gaster's transformation can explain the interchange of local spatial growth behaviour with the temporal behaviour.

4.4.5 Reverse geometry

The computations done above for the asymmetric forward geometry are repeated for the same geometry, but with the direction of the flow reversed. This flow is termed as 'reverse' flow, as shown in figure 4.5. Similar to the forward case, each eigenvalue of the one unit case is replaced by two and three eigenvalues for the two and three unit cases, respectively, see figure 4.22. The comparison along with the energy of a set of modes from Branch I is shown in figure 4.23. All the modes of this particular set exhibit spatial instability. For example, the energy of mode 4 has grown to 100 times its value at the inlet. Also, it can be noted that the maximum amplitude of these modes is in the diverging region of the channel, in line with the prediction of parallel studies. This set of modes is chosen from the high frequency part of Branch I, which is relatively more stable than the low frequency near-neutral modes. Modes near the imaginary axis have spatially decaying eigenfunctions, whereas modes far from the imaginary axis show spatially growing eigenfunctions, a trend as reported for the forward flow case. Thus as we move towards high frequencies, there is a gradual shift from temporal to spatial growth. The bifurcation into sub-branches is again more prominent at high Reynolds numbers, figure 4.24, but less so than in the forward case. Again the upper branch modes have less spatial growth than the lower.

4.4.6 Symmetric Geometry

Flow through a symmetric geometry with the same waviness amplitude as our standard geometry ($\epsilon = 2.3$) is studied at different Reynolds numbers with one, two and three units in series. The trends reported so far in the non-symmetric geometries are seen in the symmetric geometry as well, with the notable difference that the branches do not split up into sub-branches in the range of parameters studied. A comparison of the spectra obtained at different Reynolds numbers is shown in figure 4.25. Here too, the branches become flatter with increase in Reynolds number. Also as before, there are one, two and three eigenvalues for flow through one, two and three units connected in

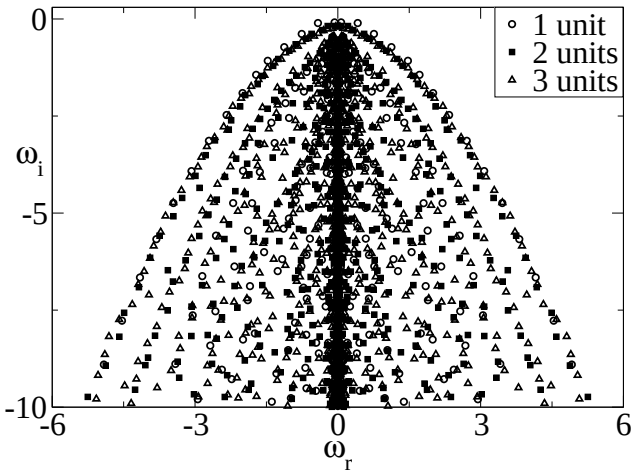

Figure 4.22: Spectra obtained for the standard geometry - reverse case, at a Reynolds number of 10, for one, two and three periodic units connected in series. Similar to the forward case, each eigenvalue of the one unit case is replaced with two and three eigenvalues for the two and three unit cases, respectively.

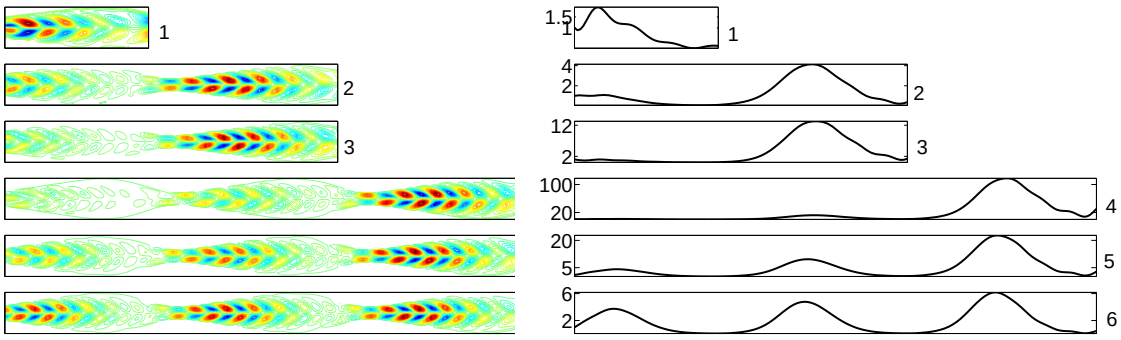

Figure 4.23: (Left) Contours of streamwise velocity of a set of modes from branch I, for reverse case (from figure 4.22). The maximum energy of these modes peak in the diverging region of the channel. (Right) Energy of the modes. In this set all the modes exhibit instability ratchet. To note is that the mode 4 grows upto 100 times the energy at the inlet.

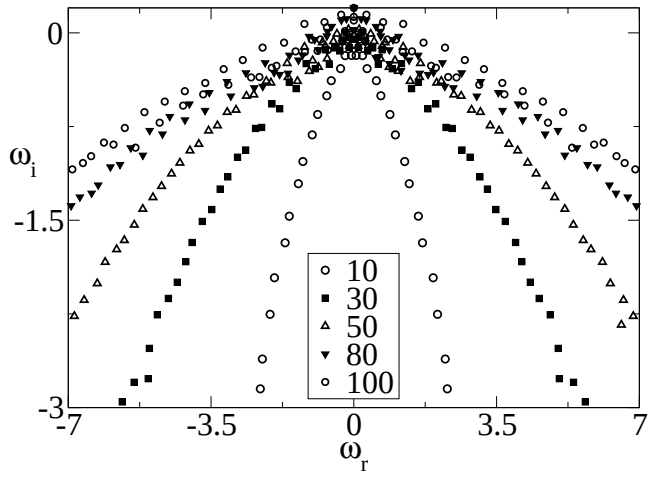

Figure 4.24: Spectra obtained at different Reynolds numbers for the standard geometry in the reverse case. The trend is similar to that seen in the forward case. But the split up of the branch into two sub-branches is less pronounced than the forward case.

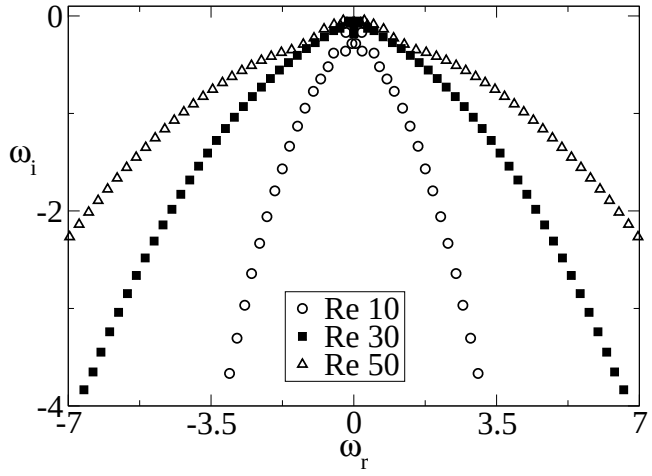

Figure 4.25: Spectra obtained at different Reynolds numbers for a symmetric geometry with $\epsilon = 2.3$. The trend is similar to that seen in the non-symmetric geometries (both forward and reverse). However, there is no splitting of the branch into two sub-branches.

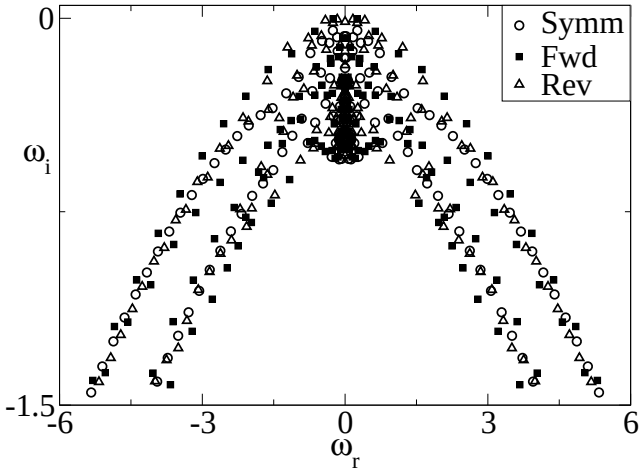

Figure 4.26: Comparison of spectra for the three geometries - forward, reverse and symmetric, at Re=50 and $\epsilon = 2.3$. The three distinct branches of the spectrum are seen in all the cases. Again, only the top two branches are shown here for clarity.

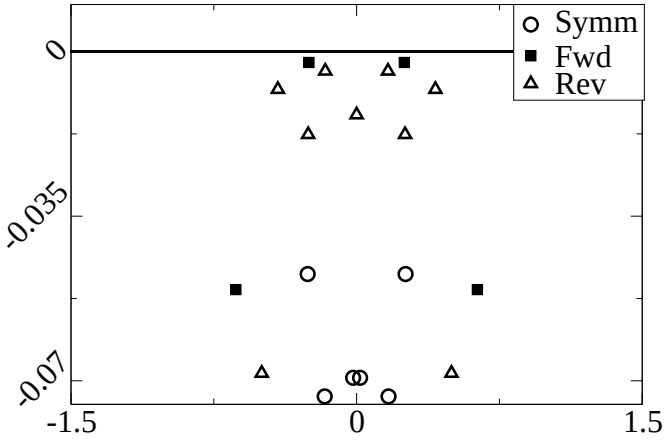

Figure 4.27: The least stable modes of the three cases discussed in figure 4.26. The reverse and forward cases are less stable than the symmetric case.

series. In the following subsection, we make comparisons between the forward, reverse and symmetric cases.

4.4.7 Comparison of forward, reverse and symmetric geometries

We first discuss the temporal instability characteristics of the three goemetries studied so far, followed by spatial instability characteristics and then disucss their relative roles. We start by comparing the spectra obtained at a Reynolds number of 50 for $\epsilon = 2.3$ of

the forward, symmetric and reverse geometries, shown in figure 4.26. Here too, only the top two branches of the spectra are shown for clarity. First, compared to the instability critical Reynolds number of 5772 for a straight channel, this flow, which is on an average a straight channel, is already near-neutral at this relatively low Reynolds number. This trend is consistent with other studies on convergent-divergent channels, but more pronounced because of the high ϵ, and because of the global approach. To compare the temporal instability characteristics, we zoom figure 4.26 near the axis and plot it in figure 4.27. We can see that both the forward and reverse geometries are temporally more unstable than the symmetric geometry. This finding can be further supported by the comparison of the spectra obtained for two forward geometries at a Reynolds number of 10, but with different ratios of divergence and convergence, shown in figure 4.28. The two geometries compared here have a divergence to convergence ratio of [4:6] and [3.4:6.6]. Here we can see that the more accentuated the asymmetry is, the more temporally unstable it is. Also, the branch split-up is more pronounced for the steeper geometry. This tells us that for the same value of ϵ, we can make the flow temporally less stable by increasing the asymmetry of the geometry. The spatial behaviour however, is the reverse, as discussed below.

Also, we can see that the split-up of the branch is stronger in the forward case, less for the reverse case and is zero for the symmetric case. This has been seen for all the Reynolds numbers studied. The bifurcation, where it exists, extends over a large range of frequencies at higher Reynolds numbers.

The spatial stability characteristics of flow through forward, reverse and symmetric goemetries show the following trend: low frequency modes of a branch (close to the imaginary axis) are spatially decaying, while the high frequency modes of the branch are spatially growing. In between these two regions is an intermediate region in which the modes split up into a pair of spatially decaying and spatially growing modes. To estimate the relative amounts of spatial and temporal instability in the forward, reverse and symmetric geometries at the same Reynolds number and same ϵ, we choose a representative case of Reynolds = 30 and $\epsilon = 2.3$ with two periodic units. The comparison of the spectra obtained are shown in figure 4.29, to the left. We choose a pair of modes in the region where the split up exists and make a comparison of their respective energies, shown to the right. The chosen modes are shown in the inset of the spectra. The energies of the modes indicated by the left ellipse in the inset are shown in the middle part of the figure. In this set of modes, the forward mode is temporally less stable than

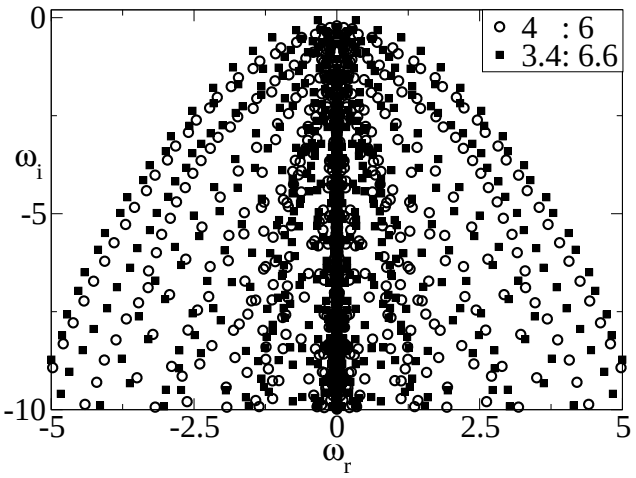

Figure 4.28: Comparison of spectra obtained for the forward geometry, with two units in series, at a Reynolds number of 10, $\epsilon = 2.3$, for two ratios of divergence to convergence. The steeper the asymmetry, the more temporally unstable the flow is.

the symmetric mode, whereas spatially it is more stable. On the contrary, the reverse mode is temporally more stable than the symmetric mode, but it is spatially less stable. A similar trend can be seen in the modes indicated by the right ellipse of the inset. This comparison emphasizes the fact that the net instability contained in a mode remains constant for a given parameter setting, and increase in one type of instability decreases the instability of the other form. Thus, by making the geometry more asymmetric, the modes become temporally more unstable, but spatially more stable. Thus, the apportionment between temporal and spatial growth is not arbitrary, but emerges as a consistent pattern based on geometry, Reynolds number, etc. In a given situation, we may tailor the geometry to increase one relative to the other. We emphasise that the introduction of fore-aft asymmetry has increased the range of possibilities.

4.4.8 Effect of amplitude of wall waviness

A comparison of the spectra obtained for increasing ϵ values for the same Reynolds number of a symmetric geometry is shown in figure 4.30. We can see that the branches in the spectrum become narrower and the low-frequency modes near the axis get more destabilized at higher ϵ. This trend is seen in both symmetric and asymmetric geometries.

Comparing figures 4.17 and 4.30, we see that with increase in Reynolds number the branches become broader and with increase in ϵ the branches become narrower. But the

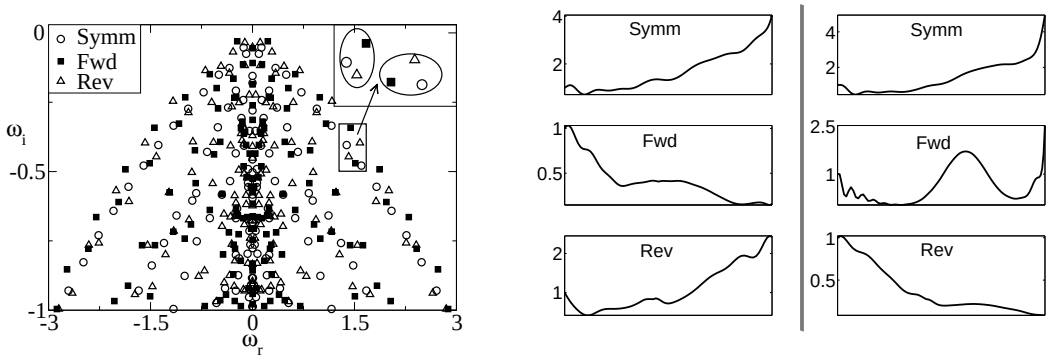

Figure 4.29: Terminology as in Table 4.2. Left: Comparison of spectra of the forward, reverse and symmetric cases at a Reynolds number of 30 with $\epsilon = 2.3$, with two periodic units. Two sets of modes shown in the inset are chosen from the intermediate region where the branch shows a split. Middle and right: energies of the modes shown in the left and right ellipses of the inset, respectively.

low frequency modes are destabilized in both the cases, giving the intuitive result that increasing ϵ and/or Reynolds number would be destabilizing. Further, by increasing ϵ, one can reduce the participation of high frequencies, which could be a useful feature as a passive control option.

We have seen that the temporal decay or growth dictated by the eigenvalue is exponential, while the spatial growth obtained by the ratchet mechanism need not be. Moreover, the classical definition of critical Reynolds number becomes blurred in this case. This is because a mode that is temporally globally unstable may have a decay in space that overcomes this temporal growth. We also have several temporally decaying but near-neutral modes, especially for $Re \geq 50$, in which the spatial instability is stronger than the temporal decay.

4.4.9 Eigenvalue Sensitivity and Pockets of Transient Growth

In this subsection, we discuss the sensitivity of the eigenvalues to (i) the grid size - which gives an indication of the discrete/ continuous form of the spectrum and (ii) the addition of small perturbations to the operator matrix - which gives some indication of the associated non-normality of the operator. Viscous flows in a semi-infinite or infinite domain will generally have a discrete and a continuous spectrum (Schmid & Henningson (2001)). The continuous spectrum arises because of the unboundedness in the domain. For bounded parallel flows, however it was shown by Lin (1961), see Drazin & Reid

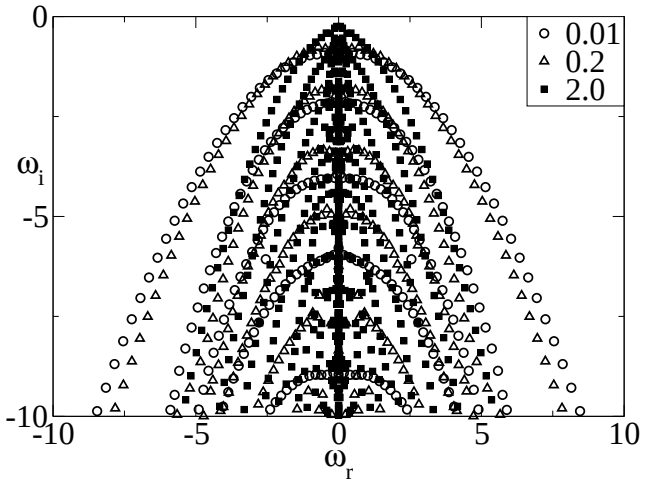

Figure 4.30: Spectra obtained for different ϵ at a Reynolds number of 10 for the symmetric geometry. It can be seen that the low frequency modes become more unstable with increase in ϵ. The branches tend to become narrower with increase in ϵ.

(2004) that the viscous eigen spectrum has to be discrete. Even though the present domain is bounded in y, Lin's proof might not hold good here as the flow is non-parallel and there is unboundedness in the streamwise direction. To check whether the eigenvalue spectrum is discrete, the spectra obtained for the standard geometry at a Reynolds number of 10 for different grid sizes is shown in figure 4.31. We can see that with increasing grid sizes, branch I of the spectrum does not become fuller, but converges to a discrete set of modes. This can be seen clearly in the inset. Even though other branches of the spectrum are sensitive to the grid size, the number of eigenvalues does not increase. This is the signature of a discrete spectrum. We remember from figure 4.13 that the number of eigenvalues increases with the number of units connected in series. For a very long channel of converging-diverging units in series, the branches would become fuller.

Next, we investigate the sensitivity of spectra to the addition of very small amplitude random perturbations to the operator matrices. This gives a measure of the non-normality associated with the matrices. More the sensitivity of the eigenvalues, more is the non-normality associated with the matrices and higher is the transient growth associated with their eigenfunctions, see Schmid & Henningson (2001). A detailed discussion about transient growth and its characteristics can be seen in Farrell (1988), Farrell & Ioannou (1993), Butler & Farrell (1992), Reddy & Henningson (1993) and references therein, and it is briefly explained here for the sake of completeness. Two or more ex-

ponentially decaying 'non-orthogonal' eigenfunctions can exhibit energy growth over short times if they are superposed with suitable initial conditions. This growth is only transient and both eigenfunctions will decay at large times, if the system remains linear. This transient growth could be substantial, increasing to many orders of magnitude of the initial energy of the disturbance. This could trigger non-linear effects, which could then dominate. The non-normality of the operator, and the resulting non-orthogonality of the eigenfunctions is a necessary (but not sufficient) condition for transient growth. We perform a sensitivity analysis by adding random perturbations of maximum amplitude 10^{-5} to the operator matrices. The spectra obtained with these perturbations are too different from the unperturbed spectrum to plot in the same figure. For ease of viewing, we reduce the maximum amplitude of the perturbation to 10^{-8} and find that the eigenvalues are extremely sensitive to very small perturbations of the associated matrices. The spectra obtained for ten different random combinations of perturbations are superposed over the spectra obtained with no perturbation at all, and shown in figure 4.32. We may estimate that modes in branch III (indicated as B3) of the spectrum are likely to participate very little in transient growth. But modes close to the imaginary axis and those in branch II (indicated as B2) show a lot of sensitivity and have a lot of potential to exhibit transient growth, if given suitable initial conditions. More importantly, for a perturbation of the order of 10^{-8}, the near-axis stable modes are pushed into the unstable half-plane. Also, for higher Reynolds numbers, several modes have very small decay rate, which would allow them to interact with each other over a longer time, to lead to interesting transient growth characteristics.

Transient growth in a flow is usually characterized by a quantity G_{max}, defined as the maximum possible disturbace energy growth at a given time, maximized over all initial conditions. This energy growth is scaled with the initial energy of the disturbance (at time t=0) and it is generally integrated over the entire domain, giving a single number. Rather than computing G_{max}, we show hitherto undisclosed opportunities for nonlinearities to pick up, from localised pockets of very large transient growth. To demonstrate this, we merely add two temporally stable modes with random initial amplitudes (whose magnitude lies between +0.5 and -0.5). For such random combinations of two modes, the energy integrated over the two-dimensional domain usually decays monotonically, or may display a small transient growth. This is because we have neither chosen the optimal perturbations nor given them the optimal initial condition. Moreover we are superimposing only two modes at a time. Hence there is no surprise that these modes

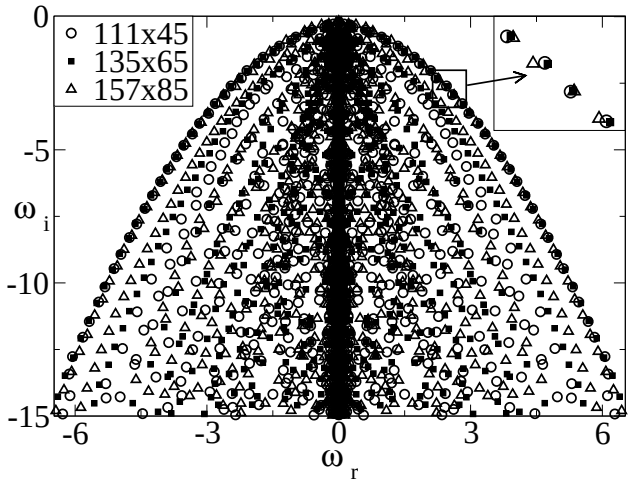

Figure 4.31: Spectrum of the standard geometry obtained with different grid resolutions, at a Reynolds number of 10. The inset indicates that this branch of the spectrum is discrete.

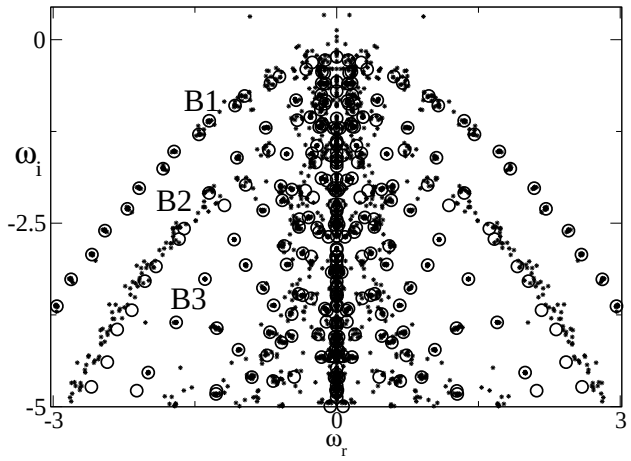

Figure 4.32: Sample pseudospectra obtained by adding random perturbations of maximum amplitude 10^{-8} to the matrix elements. The spectra obtained for ten different random combinations are superposed. The big hollow circles indicate the spectra obtained with no perturbation to the matrices. The three branches are indicated as B1, B2 and B3.

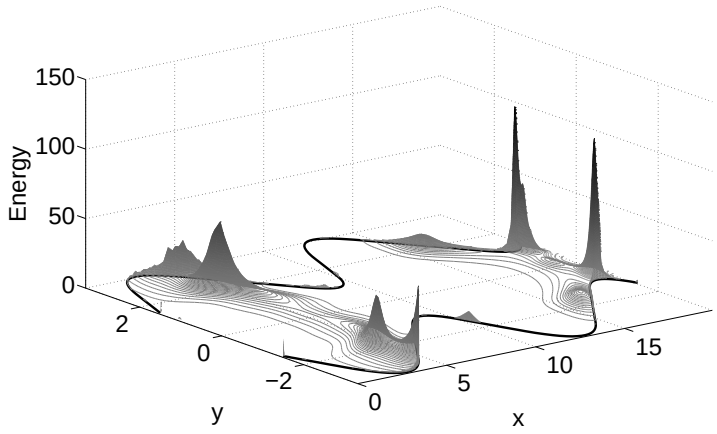

Figure 4.33: Contours of the maximum energy growth obtainable for random combination of two modes with a random initial condition, shown at every grid station. The energy has grown transiently only in some regions.

with this set of random initial conditions do not show any overall transient growth at all. But, for the same pair of modes with the same initial conditions, if we plot the local disturbance kinetic energy everywhere in the two-dimensional domain, we find pockets of transient growth, as large as 1000 times the initial energy even at a Reynolds number of 10. A three-dimensional contour of the maximum energy of two such sets of modes, added up with random initial conditions, are shown in figures 4.33 and 4.34. The modes presented are chosen from the forward case at a Reynolds number of 50. The maximum energy for a given initial amplitude of another pair of decaying modes is shown in figure 4.34. We see a localized transient growth of energy. Such a growth of energy could not be captured by the traditional 'integral energy' approach to transient growth. One thing to remember is that they are obtained for random initial conditions and are not the optimal growth. With three-dimensional perturbations, we expect the growth to be much more, given the streamwise streaks of Butler & Farrell (1992) and other studies, and this aspect is being studied.

4.4.10 Other parameters

As seen, this problem is rich in parameters. We make a few more case studies to get a qualitative idea of the response to some of them, these too are included in Table 4.2. The first case study is to obtain the effect of varying the aspect ratio of a periodic unit by

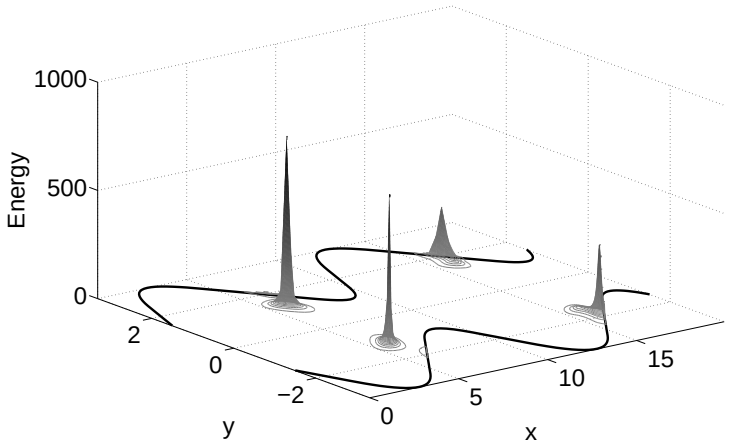

Figure 4.34: Same as figure 4.33 for a different set of modes with random initial conditions. The energy often grows by three orders of magnitude of the initial energy, at localized regions.

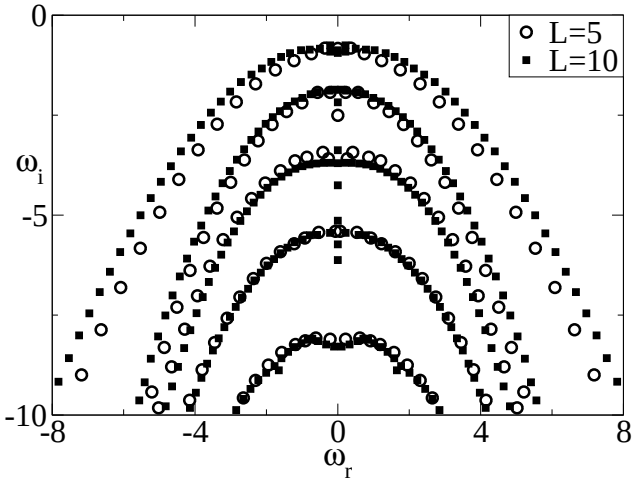

Figure 4.35: Spectra obtained for $\epsilon = 0.1$, Re=10, for symmetric geometry with length of the channel $L \sim 5$ (hollow circles) and $L \sim 10$ (filled squares). It can be seen that a shorter unit is slightly more stable than a longer unit for this combination of parameters.

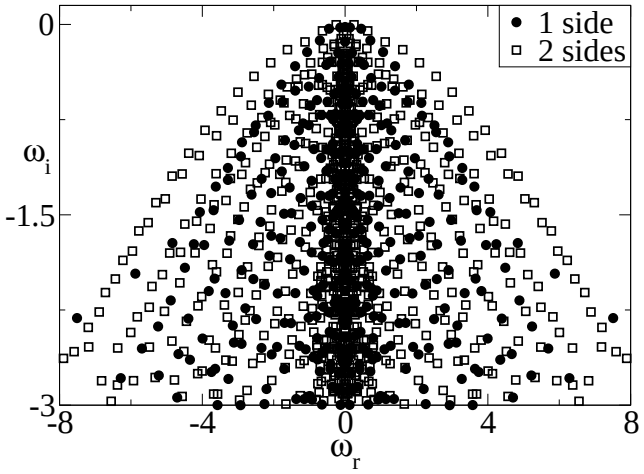

Figure 4.36: Spectra obtained for $\epsilon = 0.1$, Re=10, for the standard geometry with wall waviness present on one side (filled circless) and both sides (hollow squares).

varying L/H, keeping everything else constant. For the same parametric settings, halving the length of the geometric unit stabilizes the flow. A comparison is shown in figure 4.35 where the spectra of two symmetric channels with two different lengths for the same ϵ and Reynolds number are plotted. The divergence and convergence angles are larger for the shorter channel, but the length available for destabilisation is less. Secondly, every pair of eigenmodes in the long channel is replaced by a single eigenmode. On examining the eigenfunctions, it is seen that the pair in the long channel are of similar structure but opposite phase.

We then study a channel with a one-sided wall corrugation and find that this geometry is more stable than one with both walls corrugated. Nevertheless, it exhibits low Reynolds number instability. The eigenfunctions and the spectra obtained display rich characteristics similar to the two-side corrugated case. The branches in the spectra split-up into pairs of spatially decaying and spatially growing eigenfunctions. Also the spectra become flatter with increase in Reynolds number, a trend similar to that seen in both-sided corrugated channels. The results could have been guessed beforehand, but the purpose of computing on this geometry is that it is easier to fabricate for an experiment. This experiment is underway.

Thus, under suitable parametric settings of these converging-diverging channels, we have three equally potential mechanisms operating towards instability, namely, the exponential instability, ratchet growth in space and localised large transient growth in time. This offers us a passive control mechanism to enhance mixing in low Reynolds number

channels.

4.5 Summary

Stability of flow through channels with a series of alternating convergent and divergent sections of significant amplitude has been studied using a global stability approach. Notably, the entire eigenvalue spectrum is obtained for this geometry, for the first time to our knowledge, and the distinct branches of the spectrum are discussed in detail. We show that neither the disturbance amplitude nor the mode structure need obey the periodicity of the base flow, even in a symmetric converging-diverging channel, in contrast to what has often been assumed. An instability ratchet, with sequential amplitude growth over every periodic converging-diverging unit is demonstrated.

Asymmetric geometries are shown to display a richer range of temporal-spatial interplay than the symmetric. This is manifested as a split up of the distinct branches in the spectra into two sub-branches, one of which has higher temporal growth and lower spatial growth than the other. These geometries have not been studied earlier to our knowledge, except by Sahu (2005) in pipes with a weakly non-parallel approach, which did not and could not, yield a ratchet. Temporal instability becomes larger with increasing asymmetry, with globally unstable modes at a Reynolds number of about 50. The maximum amplitude of the disturbances need not necessarily be confined to the neck of the channel. The wavelength of a mode can change significantly within one geometric unit and can be different in different units. Moreover at a given streamwise location, a single mode can sustain different dominant length scales at different wall-normal positions, and sometimes even multiple length scales at a single location. The spatial evolution of each scale can be different, thus a spatial Floquet analysis would not be able to describe the dynamics completely.

As expected from previous wisdom, the presence of convergence and divergence reduces the critical Reynolds number. The critical Reynolds number obtained with th global approach is somewhat lower than the earlier predictions. However, it is to be remembered that the very definition of critical Reynolds number is nebulous given the spatial-temporal interplay. Also, an increase in the wall waviness amplitude destabilizes the flow. Flow through a channel with one wall straight and the other wavy is more stable than the when both walls are wavy. In this study we have focussed less on quantitative effects of these parameters and much more on new instability features that are revealed

by this global approach.

The presence of many near-neutral modes shows potential for transient growth. An elementary transient growth study is carried out here, where the resultant disturbance energy from two randomly chosen modes with randomly chosen initial amplitudes shows localized pockets of large transient growth. Most often, the total energy in these randomly chosen cases is monotonically decreasing. Our study therefore suggests that estimating transient growth locally rather than intergrating over space, can reveal new possibilities for nonlinearities to take over. A complete understanding of transient growth, especially with three-dimensional disturbances, would suggest itself as future work. These distinct instability characteristics of flow through converging-diverging channels, namely the exponential growth in time, ratchet growth in space and large amounts of localized transient growth, can be used as passive control mechanisms to encourage mixing at low Reynolds numbers. The asymmetry can be tuned to enhance mixing further.

CHAPTER 5

WALL JETS

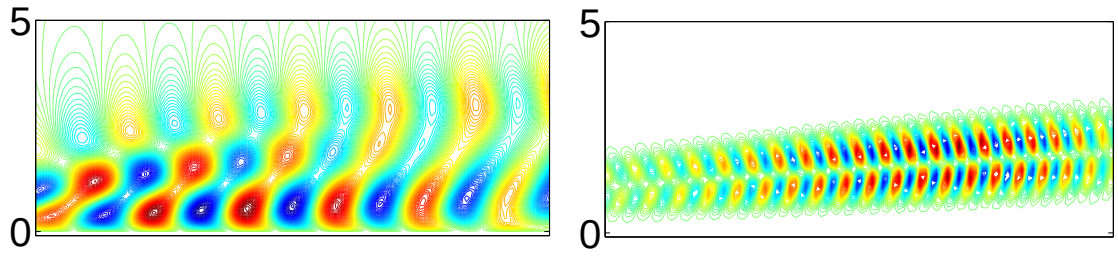

5.1 Introduction

A wall jet is produced when fluid is blown tangentially across a flat surface. A radial wall jet occurs when a jet of fluid hits a wall perpendicularly and spreads radially outwards. Wall jets were first studied by Glauert (1956), who derived the similarity solution which is valid far downstream the jet impingement, both for the planar and radial cases. The jet of fluid can be of the same velocity as the surrounding fluid or of a different velocity, as mentioned in Glauert (1956). If the fluid in the jet is different from the surrounding fluid, then the equations of motion will have to take into account the interface between the two fluids, and such a flow under certain circumstances can form a hydraulic jump. Thus, we can say that hydraulic jumps occur in a special subclass of wall jets with an interface. Wall jets are used for efficient heat transfer like in turbine blades, heat exchangers, etc. More than its applications, there is a special property of a wall jet which has motivated many hydrodynamists to study this interesting flow, as discussed below.

Two common hydrodynamic flows are boundary layers and shear layers. Wall jets are special as they can be seen (roughly) as a combination of these two distinct type of flows, a boundary layer very close to the wall and a free shear layer far away from the wall. The stability characteristics of a boundary layer and a shear layer are independently studied extensively. Important to note are the differences in their stability characteristics. A boundary layer profile on a flat plate is inviscidly stable because there is no inflection point, and instability is caused by the viscous modes. A shear flow is inviscidly unstable as it is inflectional. A wall jet will have dual stability behavior as its velocity profile is

inflectional and it has strong viscous effects close to the wall. This twin-characteristic of wall jets has been recognized by many researchers. The two distinct effects have been possible to glean even by making a parallel flow approximation. It will be interesting to study these characteristics using a global stability approach. We believe (and have shown in the chapters on non-parallel channels, chapters 3, 4) that a global stability study can reveal many important physical characteristics which are not accessible to parallel approaches. Hence we undertake this global study on wall jets.

The first stability calculations on wall jet were done by Chun & Schwarz (1967), who studied the fully-developed similarity profile far downstream under the parallel flow approximation using the Orr-Sommerfeld equation. Their main results are (i) the presence of an additional instability mode together with the least stable mode (ii) the presence of two critical layers (iii) the dominance of the outer region in instability as disturbance production is maximum there. Experimental investigations by Bajura & Szewczyk (1970), Bajura & Catalano (1975) confirmed the presence of the similarity solution predicted by Glauert (1956) and proved the dominance of the outer region in both natural and forced transitions. It was Mele *et al.* (1986) who confirmed the presence of two distinct type of instability modes, an inflectional mode peaking in the outer region and a visous mode which peaks near the wall, while the inflectional mode dominates in the transition process. The co-existence of the two modes was experimentally confirmed by Cohen & Amitay (1992). They also show that the relative roles of the inflectional (outer) and viscous (inner) modes can be controlled by blowing or suction. Scibilia (2003) studied experimentally the effect of heating, roughness and forcing on the transition characteristics of wall jet. Seidel & Fasel (2001) showed numerically that heat transfer due to a wall jet is increased by forcing. Close to its origin, a wall jet may often be approximated by the combination of an inviscid constant velocity layer and a Blasius boundary layer. Levin *et al.* (2005) studied the stability of this developing wall jet using the Parabolized Stability Equations (PSE), in which the non-parallel effects are considered upto $O(1/Re)$. The present work aims at studying the fully developed wall jets using a global stability study. The ultimate aim is to study the stabiltiy characteristics of developing wall jets close to the origin, where self-similarity is not yet achieved. In future it will also be interesting to study the heat transfer characteristics of wall jets using a global study.

5.2 Base Flow

As mentioned before, the similarity equation govering a wall jet flow was first given by Glauert (1956). The equation is given as,

$$f''' + ff'' + 2f'^2 = 0 \tag{5.1}$$

$$f(0) = f'(0) = 0, f'(\infty) = 0 \tag{5.2}$$

Here, f is the streamfunction. The primes are with respect to η, where the wall-normal dimensionless co-ordinate is defined as $\eta = y/\delta(x)$. The lengthscale in the problem is the wall jet thickness $\delta(x)$, defined as the farthest distance from the wall at which the velocity is half the maximum velocity. A wall jet profile is inflectional away from the wall and has two locations at which the velocity is half the maximum velocity. The velocity scale is U_{max}, the maximum streamwise velocity. Thus the Reynolds number will be defined as,

$$Re = U_{max}\delta/\nu \tag{5.3}$$

The following relations hold for U_{max} and δ with the streamwise coordinate x, see Schlichting (2000) or Kundu & Cohen (2004),

$$U_{max} \sim x^{-1/2} \qquad \delta \sim x^{3/4} \tag{5.4}$$

From above, we derive a relation between the dimensionless streamwise distance x/δ and Re as

$$U = a\left(\frac{F}{x\nu}\right)^{\frac{1}{2}} \tag{5.5}$$

$$\delta = b\left(\frac{x^3\nu^3}{F}\right)^{\frac{1}{4}} \tag{5.6}$$

$$\frac{Re}{ab} = \left(\frac{Fx}{\nu^3}\right)^{\frac{1}{4}} \tag{5.7}$$

$$\frac{x}{\delta} = \frac{Re}{ab^2} \tag{5.8}$$

where $a = 0.498$ and $b = 3.23$, F is the wall jet constant introduced by Glauert. See Schlichting (2000) for the definition of F and equations 5.5 and 5.6. Equation 5.8 gives

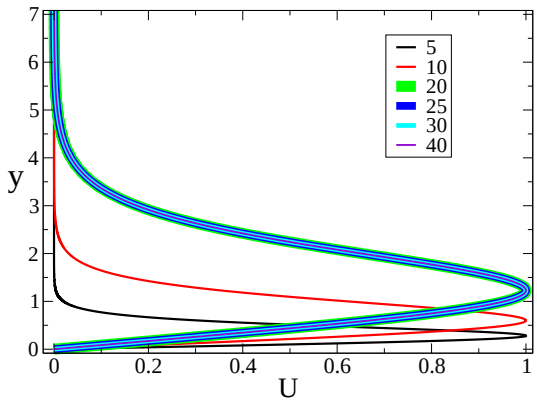

Figure 5.1: Sensitivity of base flow to the height at which the outer boundary is placed. Glauert's profile calculated for different domain heights, y. Plotted here are the stream-wise velocity U versus y. It can be noted that for domains longer than $y = 20$, the profiles coincide and the wall jet thickness δ lies at $y = 2.5$. In terms of the non-dimensional co-ordinate $\eta = y/\delta$, domains longer than 8δ ($20/2.5 = 8$) give practically identical results.

the relation between the non-dimensional x and Re, which fixes the x co-ordinate at which a particular Re is obtained. The mean flow is calculated by discretizing a domain of length of $y/\delta = 8$, into 2000 equi-distant points and solved using the fourth order Runge-Kutta method. Since one of the boundary conditions is required to be satisfied at ∞, a sufficiently large domain height has to be considered. A sensitivity study was conducted to find the minimum height at which the far-stream boundary condition can be imposed without losing accuracy and it was concluded that a height of 8δ and above gives results independent of the domain size, figure 5.1. For all the computations presented henceforth, a height of 8δ is considered to be long enough to apply the free-stream boundary conditions.

This work is done in collaboration with Dr. A Sameen, IIT Madras, India and Dr. Tamer Zaki, Imperial College, London. I first thank Dr. Sameen for proposing such an interesting problem. I also thank Dr. Tamer Zaki for pointing out the mistake in the base flow calculation. The base flow calculated from the similarity equation is validated with the direct numerical simulations of Dr. Tamer Zaki.

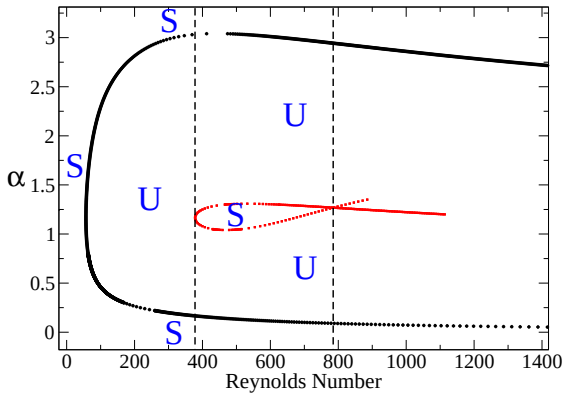

Figure 5.2: Critical Reynolds number obtained from Orr-Sommerfeld equation. This matches with the results of Chun & Schwarz (1967). S stands for stable region and U stands for unstable region. It can be seen that within the unstable region behind the black curve, a small stable region exists (shown by the red curve) which extends between $Re = 378$ and $Re = 785$, indicated by the two vertical dashed lines.

5.3 Local Stability Analysis of Wall Jets

Researchers Chun & Schwarz (1967), Mele *et al.* (1986) have earlier used the parallel flow assumption on the Glauert's profile far downstream, where the non-parallel effects are negligible. We re-computed the the neutral curve reported by Chun & Schwarz (1967) using the Orr-Sommerfeld equation, as shown in figure 5.2. In this figure, S refers to a stable region, U refers to an unstable region. As can be seen, this flow becomes unstable at a Reynolds number of 56.7 for an α of 1.16. Note that the Re_{crit} predicted is very small, i.e. instability occurs close to the origin. At this low x, it is unlikely that a similarity profile is attained as yet, which questions the validity of using the Glauert profile in the stability computations at this x. Also, according to figure 5.2, there is a small stable region starting at $Re = 378$ inside the unstable region of the neutral curve (shown in red) and this extends till $Re = 785$. This stable bubble is confined within wavenumbers 1 and 1.3. This sudden stabilization of the flow for a particular set of wavenumbers is not easy to explain on physical grounds. A second instability mode was considered to be the reason for this by many researchers. The sudden appearance of the second mode in the neutral curve was explained by Tumin & Aizatulin (1997) using a spatio-temporal analysis. They mention that behind the stable bubble, two unstable modes co-exist and there are two neutral boundaries in that region.

Let us discuss this stable bubble in detail. In figure 5.2, there are two neutral boundaries, one shown in black and the other in red. A neutral boundary is defined as the

border between an unstable region and a stable region. Let us consider a disturbance mode with a particular wavenumber, say $\alpha = 1.2$, at different Reynolds numbers. This is indicated by the horizontal green dashed line in figure 5.3. It can be seen from this figure that this mode becomes unstable at a Reynolds number of 57 (at $C1$), as it crosses the first neutral boundary (in black). It remains unstable for a range of Reynolds numbers, until it becomes stable again at a Reynolds number of 378 (at $C2$). As we proceed further downstream, this mode crosses the neutral boundary twice again (at $C3\&C4$), from an unstable region. This means that the region beyond $C4$ has to be stable and hence the red curve has to form a closed loop somewhere down so that this mode becomes unstable again for large Reynolds numbers. We repeated the computations in this region to check if this loop closes behind and computations did not find the second neutral curve closing. We used an alternative approach to understand this region. The decay/growth rate of the mode (ω_i) is plotted against the wavenumber (α) for a given Reynolds number and it is repeated for a range of Reynolds number in the region under consideration. The value of ω_i (positive or negative) tells whether the region in the neutral curve is stable or unstable. The results are shown in figure 5.4, which shows the plots for Reynolds numbers ranging from 100 to 1000 and they are shown in two separate figures for clarity. It can be seen very clearly that the disturbances of wavenumber around 1.2 become unstable for a particular range of Reynolds numbers, and this exactly coincides with the region defined by the stable bubble - 378 to 785 (shown in red in figure 5.2). This can be seen very clearly in right side of figure 5.4, where only the plots corresponding to this transition region are shown. The computations were done for Reynolds number upto 17000 and stable regions (positive ω_i) were not found for very large Reynolds numbers, see figure 5.5. The small unstable region of the large wavenumbers shown at the top left of this figure is due to the crossing of the first neutral curve, which was shown in black in figure 5.2. It can also be seen that the small wavenumber modes are the most destabilized for large Reynolds numbers. Since the modes are not changing the stability characteristics while crossing the 'tail' portion of the stable bubble, it is not clear whether to define this tail portion of the stable bubble as a neutral boundary. A mode is unstable on either side of this tail region and hence it is not clear whether this part of the figure is a neutral curve at all.

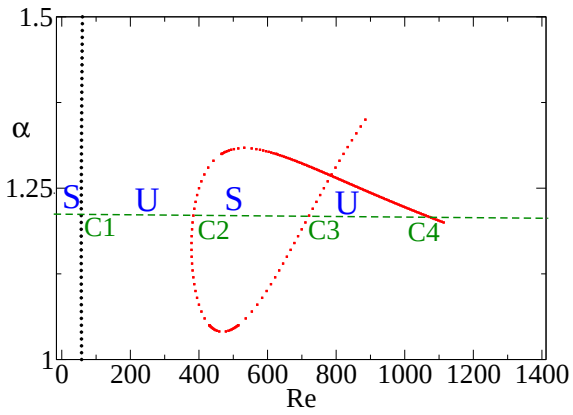

Figure 5.3: Figure 5.2 zoomed to show the stability of a mode with wavenumber 1.2 (shown by the green dashed line) with increasing Reynolds numbers. The vertical black line to the left of the figure is the first neutral curve, corresponding to Reynolds number 57. The crossings of the mode through a neutral boundary are indicated with the letter C. This mode makes 4 crossings in this range of Reynolds number.

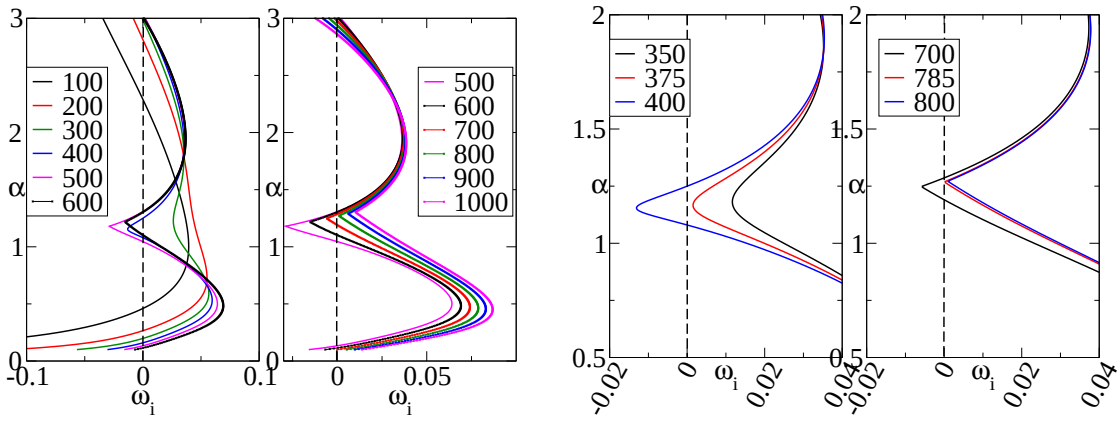

Figure 5.4: (Left) Plot of wavenumber α against the temporal growth rate (ω_i), for a range of Reynolds numbers considered in figure 5.2. (Right) Same as figure 5.4 with few plots in the vicinity of the vertical dashed lines of figure 5.2. It can be seen that a wavenumber of 1.2 becomes unstable (positive to negative ω_i) at a Reynolds number of around 375 corresponding to the first vertical dashed line; it becomes unstable again (negative to positive ω_i) for a Reynolds number of 785, which corresponds to the second vertical dashed line of figure 5.2. This shows that the flow remains stable within the second neutral curve, shown in red in figure 5.2 and unstable on either side of it.

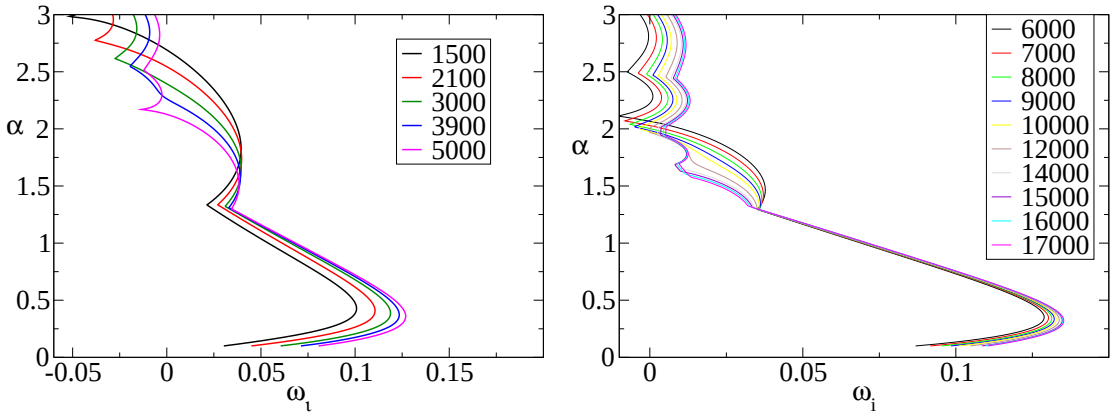

Figure 5.5: Same as figure 5.4 for large Reynolds numbers. It can be seen that the wavenumber 1.2 does not become stable again for Reynolds numbers greater than 785. The instability of the large wavenumbers seen at large Reynolds numbers (shown at the top-left of the figures) corresponds to the crossing of the black neutral curve in figure 5.2.

5.4 Global Stability Analysis of Wall Jets

In real life, since the critical Reynolds number is small, the flow might become unstable before reaching a similarity profile. This is motivation for a future study on the stability characteristics of the developing wall jet flow, well before it reaches the similarity profile. If the flow is still in the developing region, the non-parallel effects are not negligible and it cannot be studied using parallel theory. This developing flow was approximated by a combination of the Blasius boundary layer and a free shear layer away and was studied using PSE by Levin *et al.* (2005) as stated before. We study here the fully developed self-similar wall jet profile. Similar to a global stability study on self-similar JH flows (chapter 3), the 'finite domain size' effects are unavoidable in these flows too. Hence, a detailed sensitivity study has to be undertaken to arrive at reliable results.

5.4.1 Numerical Method

Chebyshev spectral discretization is used in x and y, similar to the previous chapters. Since free stream boundary conditions are used in the top boundary of the domain, a sufficiently long domain is considered in y. Since a lot of activity of the wall jet is close to the wall, the stretching function defined by equation 2.24 is used in y also, to cluster the grid points close to the wall, for which the stretching constant values are fixed to

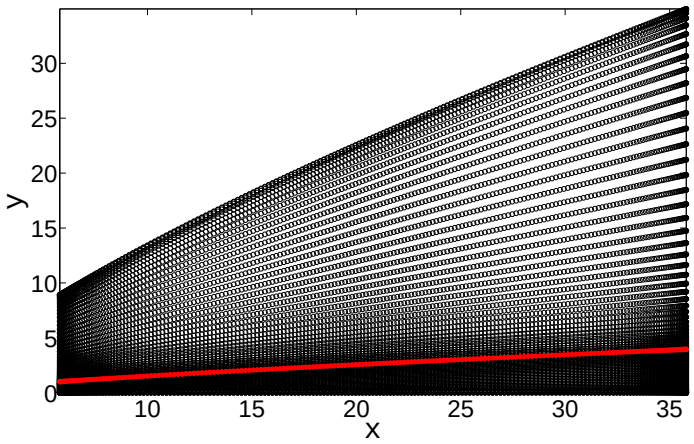

Figure 5.6: A typical distribution of grid points. The red stars indicate the location of the local wall jet thickness, δ. The grids are clusted close to the wall in y and more or less uniformly distributed in x. The grid size shown here is $201x71$.

be $a = 0.1$, $b = 6.0$. The stretching constant values in x remain unchanged from the previous studies. (Refer to section 2.6.4 for the stretching function used and a discussion on grid stretching). A typical grid is shown in Figure 5.6, where the red stars indicate the location of δ. The inflection point lies close to $y = \delta$.

5.4.2 Validation

To compare with the results of Chun & Schwarz (1967), we supply the same self-similar Glauert profile at every x location, along with V=0 in the global stability equation. Note that this is an artificial flow where the wall-jet thickness and therefore the Reynolds number are not allowed to change downstream. The wavenumber at the inlet and the exit of the domain are enforced as explained in chapter 2.12, by using Robin boundary conditions. The spectra obtained using parallel (Orr-Sommerfeld equation) and global stability (with Robin boundary conditions) for a Reynolds number of 80 and α of 2, are compared in figure 5.7. A grid sensitivity study is also conducted, a sample shown in figure 5.8. The Reynolds number indicated as 57 is the Reynolds number at the domain inlet. Since the length of the domain is restricted in x by the wavelength of the wave under consideration, a relatively small number of grids are needed in x. It is seen that 41 points in y are sufficient to capture the most unstable mode. With this small number of grid points, the critical Reynolds number calculated matches with Chun & Schwarz

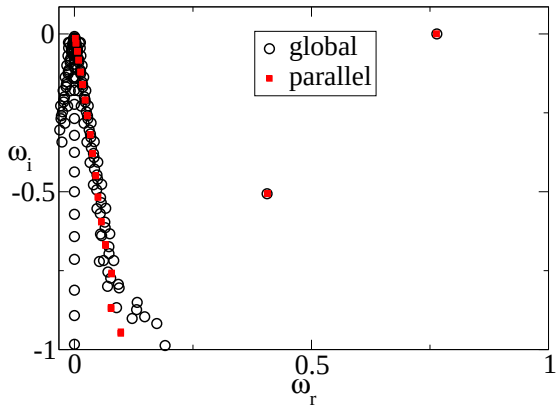

Figure 5.7: Sample spectra obtained from the global approach, imposing Robin boundary conditions (in black circles), and the parallel approach (in red squares). The Reynolds number is 80 and the α is 2. It can be noted that the least stable mode is well captured by the global analysis.

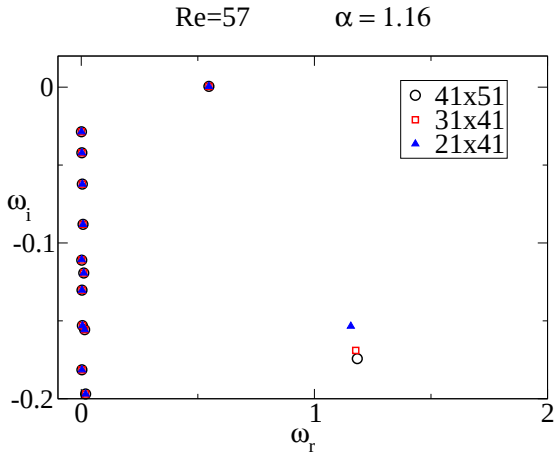

Figure 5.8: Grid sensitivity study. It can be noted that the least stable eigenvalue is quite insensitive to the grid in the range considered.

(1967)'s results, as shown in figure 5.9.

Next, to consider a realistic case, consider the wall-normal velocity and allow for Reynolds number and δ variationa across the domain. The wall-normal velocity is given as,

$$V(x) = \frac{\delta_1 U_1}{4{x_1}^{0.25} x^{0.75}} [-f + 3\eta f_\eta]. \tag{5.9}$$

Here, the subscript 1 corresponds to the value at the inlet x location (x_1). This appears because the lengthscale and velocity scale are chosen as δ and U_{max} at the inlet. f is the streamfunction and η is the non-dimensional y co-ordinate. It can be seen from equations

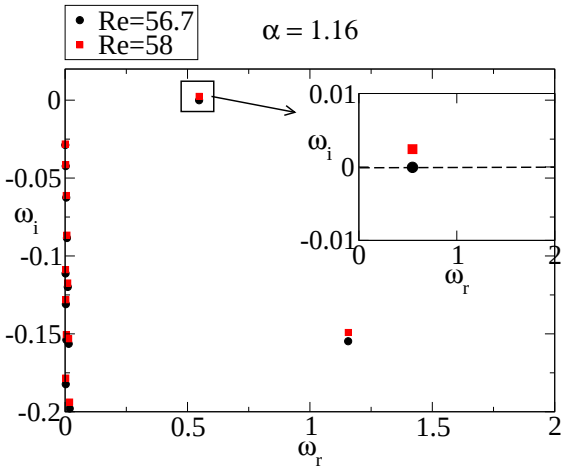

Figure 5.9: Critical Reynolds number calculated for validation.

5.3 and 5.4 that the Reynolds number increases with x as,

$$Re \sim x^{1/4}. \tag{5.10}$$

Consider for example, a case where the inlet Reynolds number is 50, the domain length is 10. Then, from equation 5.8, the domain starts at $x = 9.623$ and ends at $x = 19.623$. The exit Reynolds number for this case will be, according to equation 5.10,

$$\frac{Re_2}{Re_1} = \left(\frac{x_2}{x_1}\right)^{1/4} \tag{5.11}$$

$$Re_2 = 50 * 1.1949 = 59.79 \tag{5.12}$$

For the range of wavenumbers considered, a typical disturbance wavelength varies from 6 to 60. A 'critical Reynolds number' is not a well-defined quantity in this global study. This is because the Reynolds number varies significantly across the domain. A domain starting from a subcritical Reynolds number and ending at a supercritical Reynolds number might not be able to capture the least stable eigenvalue corresponding to the inlet Reynolds number. Secondly the least stable wavenumber at the inlet would be different from the one at the exit. Since the change in Reynolds number and the least stable wavenumber in the domain is too large, with Robin boundary conditions we were not able to converge to a single neutrally stable eigenvalue for the entire domain.

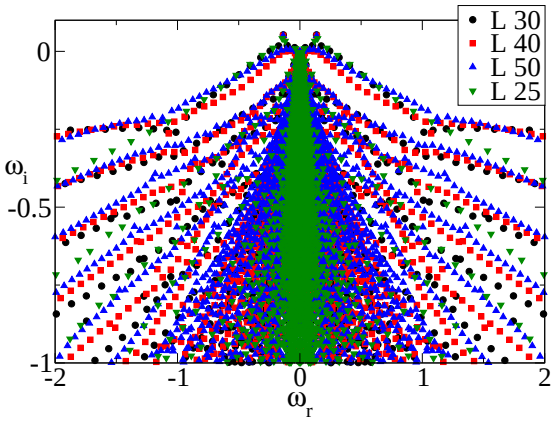

Figure 5.10: Spectra obtained at $Re = 100$ for different lengths of the domain. It can be seen that the qualitative picture of the spectra remains unchanged with change in domain length. In the results shown, it is ensured that the number of grid points considered over a given length is kept the same. Some quantitative effect is of course expected, since the range of Reynolds numbers over which a common global mode is being sought increases with L.

5.4.3 Sensitivity

We next perform a global stability analysis with extrapolated boundary conditions (EBC), as used in the previous chapters. It is however expected that if a considerably long domain is considered, the type of boundary conditions at the inlet/exit will not affect the solutions. The results will change quantitatively depending upon the length of the domain considered since the range of Reynolds number increases with length L, but their qualitative picture remains the same. This is because the lengthscale of the disturbance captured by this analysis will be restricted by the domain length. We perform a series of tests to study the sensitivity of the spectra to the number of grids and length of the domain considered. A few comparisons are given in figures 5.10 to 5.12.

As mentioned before, one of the main purposes of the present study is to understand how different the global modes are from the parallel modes, and how valid a parallel assumption is for wall jets. For this, we first compare the global modes with parallel modes. The global stability computations are done for different inlet Reynolds numbers of 30, 40, 50, 80, 100, and 200, for different lengths of the domain. A comparison of the spectra obtained is given in figure 5.13. As expected, the modes are destabilized with increase in Reynolds number. A portion of this figure near the imaginary axis is shown in figure 5.14. It can be seen from this figure that the flow becomes globally unstable for

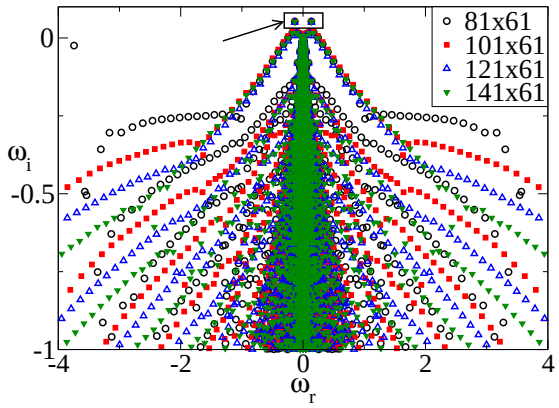

Figure 5.11: Sensitivity of the spectra to the number of grid points in the x direction, for $L = 30$ and $Re = 100$. It can be noted that the spectra contain distinct branches and the second limb of the branches gradually disappear with increase in the number of grid points in x. The sensitivity of the second limb of the branch is further decreased by increasing accuracy in y, as explained in the next figure.

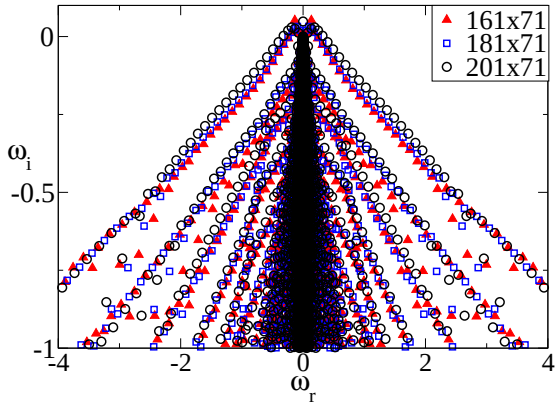

Figure 5.12: In continuation to the previous figure, it can be noted that with 71 points in y the second limb of the branch disappears and 161 points in x are sufficient for a length of 30, at a Reynolds number of 100. It can also be noted that the two very unstable modes which were present with other grid resolutions (in figures 5.10 and 5.11 and enclosed with a rectangle in figure 5.11) have disappeared with increase in m.

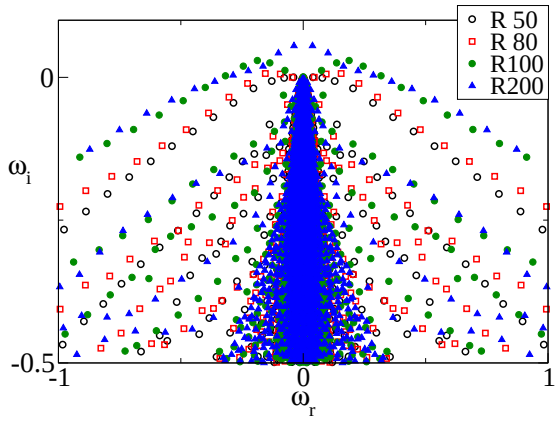

Figure 5.13: Spectra obtained for different Reynolds numbers for a domain length of 30. We can see that the upper branch becomes more destabilized with increase in Reynolds number.

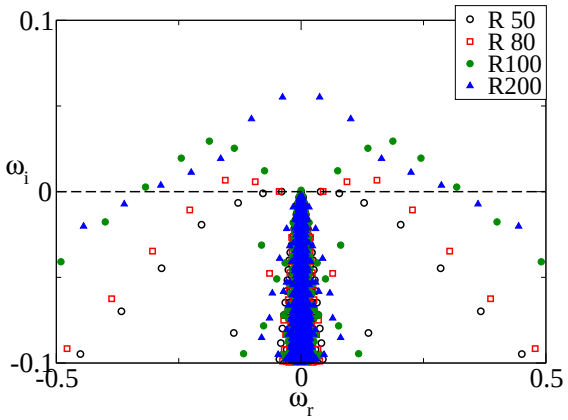

Figure 5.14: Same as figure 5.13, zoomed close to the axis. It can be seen that this flow is globally unstable at a Reynolds number of 80.

a Reynolds number between 50 and 80. It is worth remembering that the Re_{crit} obtained from parallel approach for this flow is 57.

Now, let us try to understand the characteristics of the global modes. The spectra obtained for a Reynolds number of 100 with domain length 30 and a grid size 201x71 is given in figure 5.15. Plots of the streamwise velocity of typical modes from each branch are shown in figures 5.16 and 5.17. We can see that branch 1 has a set of modes which are completely different from the modes of the other branches. Branches 2-4 have similar looking modes. Also, the modes of branches 2-4 have extended regions of positive and negative velocities, thus giving them an appearance of 'arrow heads'. These modes shall be contrasted with the modes obtained from local stability analysis, shown

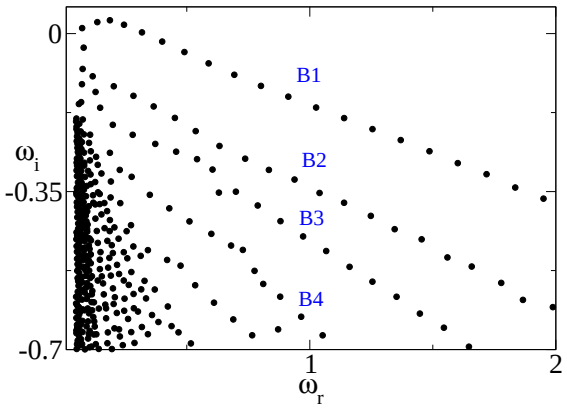

Figure 5.15: Spectrum obtained for a Reynolds number of 100 with domain length 30 with a grid size 201x71. The spectrum has distinct branches, named as branches 1-4 as shown.

in figure 5.18. The richer variety of disturbances obtained using a global approach is immediately apparent.

Next, we compare the modes within one branch, say branch 1. The following trend is observed: modes with large frequency have different structure compared to the low frequency modes, a comparison shown in figure 5.19. We can note here that the peak of the low frequency mode is very close to the wall whereas the high frequency mode peaks at about $\eta = 1$ which is close to the inflection point of the velocity profile. These two types of modes are called as wall mode (or inner mode) and inflectional mode (or outer mode), respectively. These two types of modes have been reported earlier in literature, see Mele *et al.* (1986) for example. A similar trend is seen in other branches also, a sample is given in figure 5.21 which shows modes from branch 2.

Another interesting behaviour to be noted about the low frequency branch 1 mode is the non-wave-like behaviour, see top of figure 5.19. Towards the beginning of the domain, this global mode displays three blobs at each streamwise station. As we proceed downstream, we can notice that the top two blobs merge, so that at the end of the domain we see just two blobs. This is another non-wave like feature revealed by a global study which is inaccessible to local study. This particular feature is seen in wall jets, and others were seen in previous chapters. In addition, the variation of the maximum amplitude of this mode is different at different wall-normal locations. This is shown in figure 5.20, where the maximum amplitude variation of one of the global modes shown in figure 5.19 is shown. The corresponding two wall-normal locations are also shown in the right side of the figure. We can see that within a single global mode, the amplitude of the modes

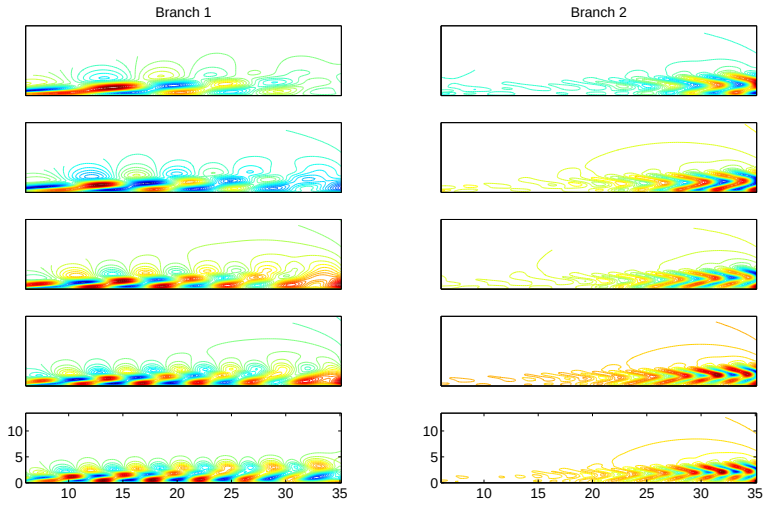

Figure 5.16: Typical set of modes from branch 1 (left column) and branch 2 (right column). Plotted here are the contours of streamwise velocity. We can see that the branches exhibit qualitatively different modes. Especially the modes in branch 1 show different wavelengths close to and away from wall.

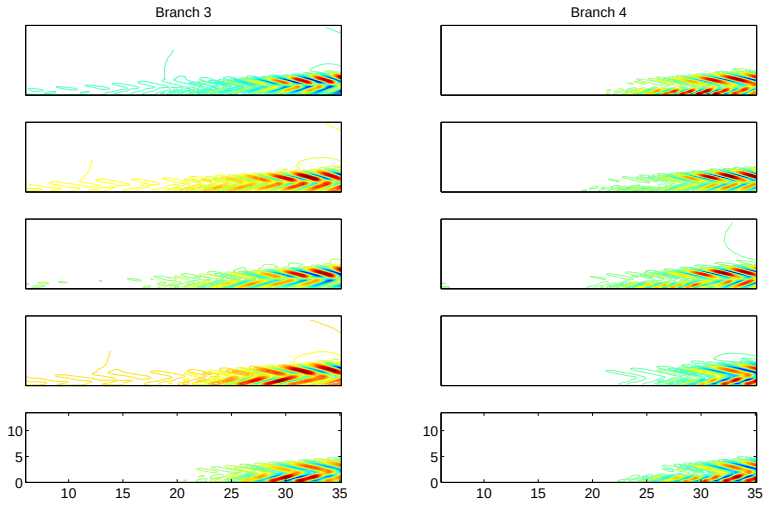

Figure 5.17: Typical set of modes from branch 3 (left column) and branch 4 (right column). Plotted here are the contours of streamwise velocity. We can see that these two branches have modes looking similar to those in branch 2. These modes exhibit extended regions of positive and negative velocities thus giving them the shape of a ‘arrow head’.

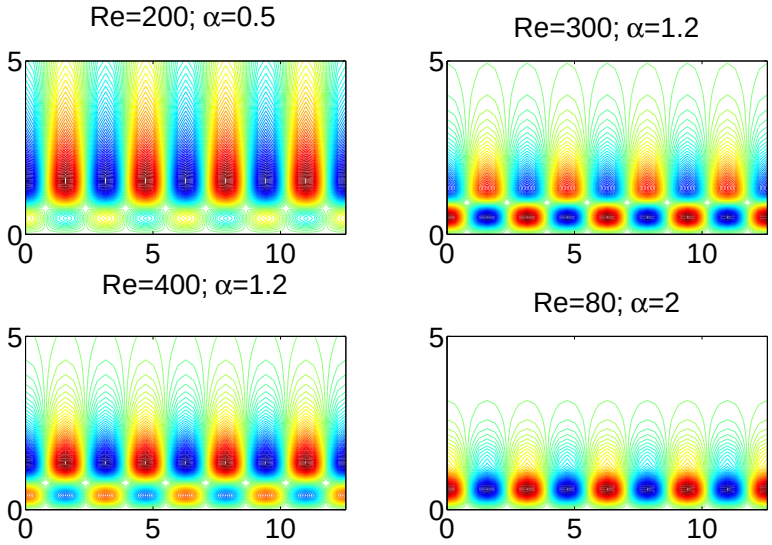

Figure 5.18: Typical modes obtained from the local stability analysis. The local profile obtained is extended in x with the given wavenumber, indicated as α in the figure. The inflectional modes (the two plots to the left) have their maximum amplitude away from the wall and the wall modes (the two plots to the right) have their maximum amplitude close to the wall.

can vary differently at different y, similar to what was reported in the previous chapter.

To add to this, we perform a wavelet transform of a typical global mode, shown in figure 5.22. Similar to the geometries studied in the previous chapters, we see that the dominant lengthscale of these modes varies with both x and y. For the mode just discussed, the wavenumber variation is not very significant.

An interesting feature about these global modes is their growth in space. Except for the low frequency modes of branch 1, (see figures 5.16 and 5.17) we see that the other modes exhibit a spatial growth, in which the amplitude of the mode increases with x. These modes are temporally more stable. This behaviour is similar to the situation discussed in the previous chapter on converging-diverging channels. The difference is, the spatial growth discussed in chapter 4 is the growth over many periodic units of the channel. But the spatial growth we discuss here is local spatial growth in amplitude of the global modes. Except for the slight downstream change in character of some of the modes and some small quantitative differences, we may conclude that a parallel or WNP study can capture the important features of a wall jet. In the global“ study of Ehrenstein & Gallaire (2005) on a boundary layer, there was a similar finding, in that the global

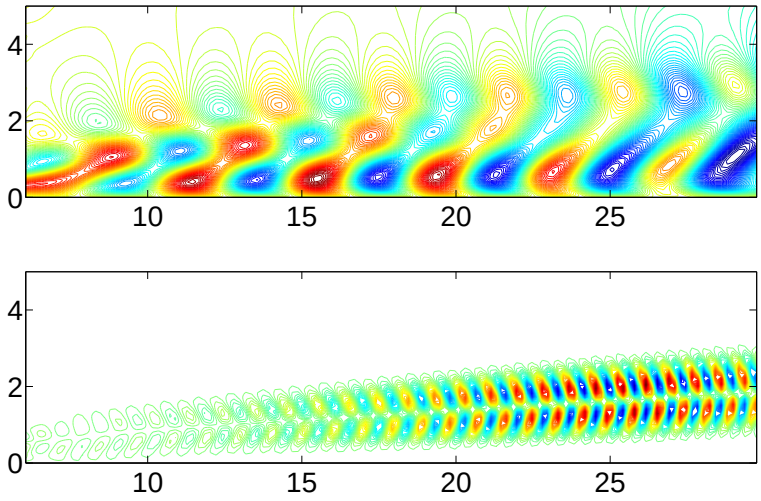

Figure 5.19: Typical low frequency global mode (top) and high frequency global mode (bottom) from branch 1 of figure 5.15. It can be seen that the low frequency mode peaks closer to the wall, whereas the high frequency mode peaks slightly further from the wall.

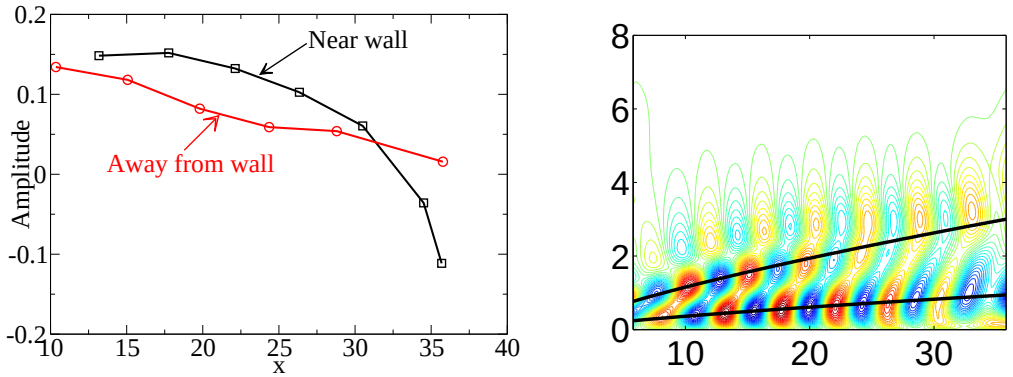

Figure 5.20: The maximum amplitude variation of the global mode shown in the top of figure 5.19 at two wall-normal locations. The two wall normal locations are indicated by the black solid line in the figure to the right.

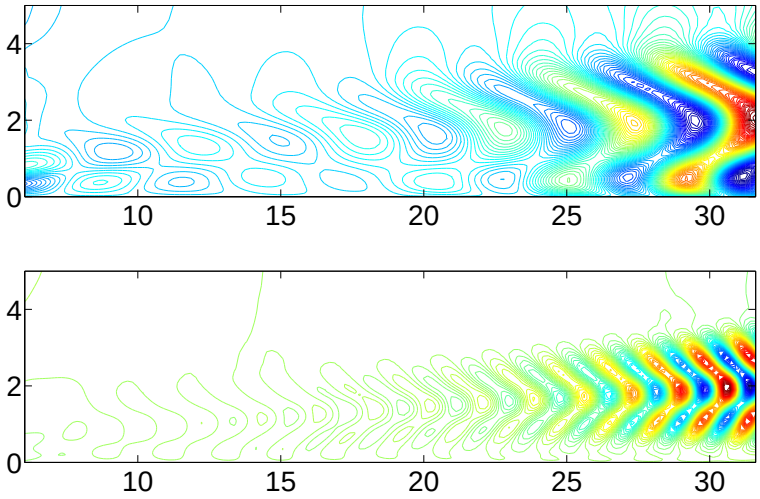

Figure 5.21: Typical low frequency mode (top) and high frequency mode (bottom) from branch 2 of figure 5.15. It can be seen that the low frequency mode's peak is close to the wall whereas the high frequency mode's peak is close to the inflection point.

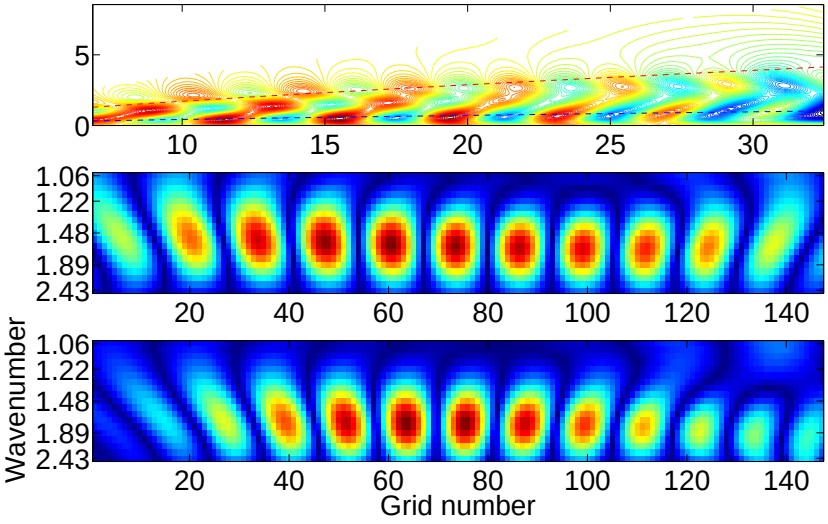

Figure 5.22: (Top) Contours of streamwise velocity of a typical global mode from branch 1 of figure 5.15. (Bottom and center) Wavelet transforms of the global mode at the two wall-normal locations indicated by the red dashed lines. We can see that the variation of wavenumber with x is more prominent that the variation of wavenumber with y.

study produced only a quantitative rather than a qualitative change. These studies thus indicate that stability behavior is modified on a global basis for enclosed flows through channels while the structure is local for wall jets and boundary layers.

CHAPTER 6

SUMMARY

6.1 Introduction

A global stability code has been developed and validated against existing results in straight channel and diverging channels with small angles of divergence. The role of the Robin boundary conditions in validation has been highlighted. A bi-global stability approach has been conducted on flow through variable geometry channels and fully-developed wall jets. In all the cases studied, it is seen that the global stability approach reveals new types of instability modes which are inaccessible to local stability approaches.

The first thing to highlight is the fact that this is the first global stability study, to our knowledge, on all the three cases considered. More importantly, this is the first global stability study to compute the entire eigenvalue spectrum. It has been seen that the spectrum obtained for each case has distinct branches and the global modes of a particular branch has a characteristic mode structure.

The highlights of all the three studies undertaken are given below separately.

6.2 Diverging Channel Flows

- Flow through a diverging channel is studied first as it is the simplest non-parallel flow to construct. The Reynolds number of this flow remains constant downstream.

- Flow through infinitely diverging channel (JH case) and channel with a finite diverging region (SDS case) are studied. Base flow for JH case is obtained from similarity equation and that for SDS case is obtained from numerical simulations.

- For the same parametric setting of $Re = 100$ and $\theta = 5^o$, JH flow does not show any separation whereas SDS flow shows a region of weak separation. The instability mechanism is dominated by the effect of divergence, in the parameter ranges studied.

- An analytical expression on why the critical Reynolds number should be so sensitive to geometry is provided. This is explained based on the change in the second derivative of the velocity profile, due to divergence.

- Even though the JH flow diverges infinitely and the SDS flow has a finite diverging region, the global spectra and the instability modes obtained for both the cases have a striking similarity. The mode structure of both the cases have similar qualitative features. The disturbance modes are localized in the diverging region and the stability characteristics are defined by the diverging region, finite or infinite.

- The global modes obtained do not obey the local scaling relation. This type of modes cannot be obtained from a local stability analysis.

- A wavelet transform of the global modes indicate that the local lengthscale of the global modes vary with the streamwise distance x, with a scale usually different from what one would expect from a local stability analysis. In addition, the modes exhibit different lengthscales at different wall-normal locations, which has never been reported before.

- Time evolution of the modes in the form of a movie indicates the existence of a new branch in the spectrum, in which all the modes propagate upstream. Modes in all other branches propagate downstream. This new branch exists only beyond a certain divergence angle. This branch exists even after application of heavy amount of sponging at the exit of the domain, to avoid spurious reflections, if any. This particular set of modes is interesting to study, since the Howard's semicircle theorem would allow upstream propagating modes only in flows with separated profiles.

6.3 Converging-diverging Channel Flows

- Flow through a series of converging-diverging units is studied with extrapolated boundary conditions. Geometries with fore-aft symmetry and asymmetry are studied using a global approach for the first time. Different wall waviness amplitudes are considered with special emphasis on large amplitudes, to achieve low Reynolds number global instability. We see that these channels become unstable at Reynolds numbers as low as 50.

- It has been shown that imposing periodic boundary conditions, as done by previous workers, over a single periodic unit of flow is too restrictive a condition and produces many spurious modes.

- The first result is that the disturbances do not obey the periodicity of the base flow. In addition, instability ratchets are possible, which is defined here as the sequential increase of the disturbance energy over successive periodic units. This instability ratchet is discussed using Floquet theory with complex Floquet exponents. It is re-emphasized that previous Floquet studies on such geometries were not able to capture the instability ratchets because of assuming 'real' Floquet exponents. This spatial growth, even of a temporally damped mode, is important as it could enhance transient growth in the downstream units compared to the upstream units.

- There is an interplay between the temporal and spatial stability characteristics of the global modes. Spatial instability here has to be interpreted in terms of the instability ratchet. For a given parameteric setting, the total amount of instability contained in the mode is fixed. Increase in one type of instability results in corresponding decrease in the other type of instability of the mode. This interplay is different from that predicted by Gaster's transformation. This has been shown using a model Floquet study.

- Increasing the number of periodic units connected in series increases the number of eigenvalues. More importantly, it increases the spatio-temporal interplay among the modes.

- Increase in Reynolds number destabilizes the flow and an entire branch of the spectrum becomes near-neutral, in contrast to straight channels, where typically only one mode gets destabilized with increase in Reynolds number.

- The branches of the spectrum split into two sub-branches with the upper sub-branch showing spatial decay and the lower one exhibiting spatial growth. This split-up of the branches is more for large Reynolds numbers. This is another manifestation of the spatio-temporal interplay.

- Wavelet transform of the global modes indicate that the local lengthscale of these modes are functions of both x and y. More important than their lengthscale is their growth behaviour, which is scale dependant and space dependant. This has

also been shown using a wavelet transform. This indicates that a single Floquet exponent cannot describe the growth behaviour of the entire periodic unit and it has to be studied using a global approach.

- Flow through geometries with fore-aft asymmetry are temporally more unstable than those with fore-aft symmetry. More the fore-aft asymmetry is, more unstable the flow is, in a temporal sense. We can exploit this feature to design the geometry of the channel to obtain the desired stability behaviour.

- Increase in wall waviness amplitude of the channel increases the temporal instability. Flow with wall corrugations on both sides are more unstable than those with just one side wall corrugation. Flow through a channel is more stable than one through a channel whose length is doubled, with all other parameters fixed.

- Mere superposition of two modes show localized pockets of large transient growth. Such a behaviour would be missed if we were to integrate the kinetic energy over the entire domain. Hence, we suggest that the energy of the global modes must be estimated on a local basis in calculation of transient growth characteristics.

6.4 Wall Jets

- A local stability analysis has been performed first, using the Orr-Sommerfeld equation. This is done to understand the region behind the ‘stable bubble’ within the unstable region of the neutral curve. It has been seen that the region behind this stable bubble remains unstable for a large range of Reynolds numbers.

- The global spectrum has distinct branches and modes of a particular branch have similar mode structure.

- The critical Reynolds number predicted by global stability analysis coincides with the one predicted by the local analysis.

- A global stability analysis reveals modes whose amplitudes peak close to the wall region, called as wall modes and those whose amplitudes peak a little away from the wall, called as inflectional modes.

- A different facet of non-wave-like behaviour of global modes is seen here, with the mode shape changing downstream. In addition, the growth behaviour of the global

modes is also different for different wall-normal locations. These are however minor compared to the effects.

6.5 Future Work

- The global stability code which has been developed has no assumptions and restrictions in the usage. Hence, it can be easily extended to study the stability behaviour of any 2D complex flow field, like wakes, mixing layers, separated regions, etc., to name a few.

- The present work deals with the addition of two-dimensional perturbations to the base flow. Transient growth obtained with 2D disturbances is much less than what one would obtain from 3D disturbances. Even with 2D perturbations, we obtain transient growth of the order of 1000 in the case of converging-diverging channels. It would be very interesting to study the transient growth obtained from 3D perturbations in all these flows. Extension of the present code to accomodate 3D disturbances is underway.

- A collaboration has been initiated with Dr. Rajesh Ganapathy, ICMS, JNCASR, for the experimental verification of the instability in converging-diverging channels at small scales. The idea to work with wall corrugation on only side came from him as it is easy to construct.

- The present work is limited to a fully developed wall jet. Our ultimate aim is to study the stability characteristics of a developing wall jet which occurs close to the origin and then study the heat and mass transfer characteristics of them. This has a lot of industrial applications.

Bibliography

AKERVIK, E., EHRENSTEIN, U., GALLAIRE, F. & HENNINGSON, D. S. 2008 Global two-dimensional stability measures of the flat plate boundary-layer flow. *Euro. J. of Mechanics B/Fluids* **27**, 501–513.

AKERVIK, E., HOEPFFNER, J., EHRENSTEIN, U. & HENNINGSON, D. S. 2007 Optimal growth, model reduction and control in a separated boundary-layer flow using global eigenmodes. *J. Fluid Mech.* **579**, 305–314.

ALIZARD, F. & ROBINET, J.-C. 2007 Spatially convective global modes in a boundary layer. *Phys. of Fluids* **19**, 114105.

ALLMEN, M. J. & EAGLES, P. M. 1984 Stability of divergent flow: a numerical approach. *Proc. R. Soc. Lond* **A 392**, 359–372.

BAJURA, R. A. & CATALANO, M. R. 1975 Transition in a two-dimensional plane wall jet. *J. Fluid Mech.* **70**, 773–799.

BAJURA, R. A. & SZEWCZYK, A. A. 1970 Experimental investigation of a laminar two-dimensional plane wall jet. *Phys. Fluids* **13**, 1653–1664.

BANKS, DRAZIN & ZATURSKA 1988 On perturbations of jeffrey-hamel flow. *J. Fluid Mech* **186**, 159.

BARBAGALLO, A., SIPP, D. & SCHMID, P. J. 2009 Closed-loop control of an open cavity ow using reduced-order models. *J. Fluid Mech.* **preprint**.

BARKLEY, D., GOMES, M. G. M. & HENDERSON, R. D. 2002 Three-dimensional instability in flow over a backward-facing step. *J. Fluid Mech.* **473**, 167–190.

BERS, A. 1983 Space-time evolution of plasma instabilities - absolute and convective. *Handbook of Plasma Physics, ed. M N Rosenbluth and R Z Sagdeev* **1**, 451–517.

BERTOLOTTI, F. P. & HERBERT, T. 1991 Analysis of the linear stability of compressible boundary layer using the pse. *Theor. Comp. Fluid Dyn.* **3**, 117–24.

BERTOLOTTI, F. P., HERBERT, T. & SPALART, P. R. 1992 Linear and nonlinear stability of blasius boundary layer. *J. Fluid Mech.* **242**, 441–474.

BETCHOV, R. & CRIMINALE, W. O. 1966 Spatial instability of the inviscid jet and wake. *Phys. Fluids* **9 (2)**, 359–362.

BHATTACHARYA, P., MANOHARAN, M., GOVINDARAJAN, R. & NARASIMHA, R. 2006 The critical reynolds number of a laminar incompressible mixing layer from minimal composite theory. *J. Fluid Mech.* **565**, 105–114.

BLANCHER, S. & CREFF, R. 2004 Analysis of convective hydrodynamics instabilities in a symmetric wavy channel. *Phys. Fluids* **16, (10)**, October.

BLANCHER, S., CREFF, R., BATINA, J. & ANDRE, P. 1994 Hydrodynamic stability in periodic geometry. *Finite Elements Analysis and Design* **16**, 261–270.

BOTTARO, A., CORBETT, P. & LUCHINI, P. 2003 The effect of base flow variation on flow stability. *J. Fluid Mech* **476**, 293–302.

BUTLER, K. M. & FARRELL, B. F. 1992 Three-dimensional optimal perturbations in viscous shear flow. *Phys. Fluids A* **4 (8)**, 1637–1650.

CABAL, A., SZUMBARSKI, J. & FLORYAN, J. M. 2002 Stability of flow in a wavy channel. *J. Fluid Mech.* **457**, 191–212.

CEBECI, T., SHAO, J. P. & KAFYEKE, F. 2005 *Computational fluid dynamics for engineers: from panel to Navier-Stokes methods with computer programs*. Springer.

CHEDEVERGNE, F., CASALIS, G. & FERAILLE, T. 2006 Biglobal linear stability analysis of the flow induced by wall injection. *Phys. Fluids* **18**, 014103.

CHO, K. J., KIM, M. & SHIN, H. D. 1998 Linear stability of two-dimensional steady flow in wavy-walled channels. *Fluid Dynamics Research* **23**, 349–370.

CHRISTODOLOU, K. N. & SCRIVEN, L. E. 1988 Finding leading modes of a viscous free surface flow: An asymmetric generalized eigenproblem. *J. Scientific Computing* **3 (4)**, 355–406.

CHUN, D. H. & SCHWARZ, W. H. 1967 Stability of the plane incompressible viscous wall-jet subjected to small disturbances. *Phys. Fluids A* **10**, 911–915.

COHEN, J. & AMITAY, M. 1992 Laminar-turbulent transition of wall-jet flows subjected to blowing and suction. *Phys. Fluids(A)* **4 (2)**, 283–289.

CRIMINALE, W. O., JACKSON, T. L., LASSEIGNE, D. G. & JOSLIN, R. D. 1997 Perturbation dynamics in viscous channel flows. *J. Fluid Mech.* **339**, 55–75.

DEISSLER, R. J. 1987 The convective nature of instability in plane poiseuille flow. *Phys. of Fluids* **30(8)**, 2303–2305.

DENNIS, S. C. R., BANKS, W. H. H., DRAZIN, P. G. & ZATURSKA, M. B. 1997 Flow along a diverging channel. *J. Fluid Mech.* **336**, 183–202.

DIJKSTRA, H. A., MOLEMAKER, M. J., PLOEG, A. V. D. & BOTTA, E. F. F. 1995 A efficient code to compute non-parallel steady flows and their linear stability. *Computers and Fluids* **24 (4)**, 415–434.

DRAZIN, P. G. 1999 Flow through a diverging channel: instability and bifurcation. *Fluid Dynamics Research* **24**, 321–327.

DRAZIN, P. G. & REID, W. H. 1981 Hydrodynamic stability. *Cambridge University Press* .

DRAZIN, P. G. & REID, W. H. 2004 *Hydrodynamic stability*. Cambridge University Press.

EAGLES, P. M. 1966 The stability of a family of jeffery-hamel solutions for divergent channel flow. *J. Fluid Mech.* **24, part 1**, 191–207.

EAGLES, P. M. & SMITH, F. T. 1980 The influence of nonparallelism in channel flow stability. *J. Engg. Math.* **14, 3**, 219–237.

EAGLES, P. M. & WEISSMAN, M. A. 1975 On the stability of slowly varying flow: the divergent channel. *J. Fluid Mech* **69**, 241–262.

EHRENSTEIN, U. 1996 On the linear stability of channel flow over riblets. *Physics of Fluids* **8 (11)**, 3194–3196.

EHRENSTEIN, U. & GALLAIRE, F. 2005 On two-dimensional temporal modes in spatially evolving open flows: the flat-plate boundary layer. *J. Fluid Mech.* **536**, 209–218.

FARRELL, B. F. 1988 Optimal excitation of perturbations in viscous shear flow. *Phys. of Fluids* **31 (8)**, 2093–2102.

FARRELL, B. F. & IOANNOU, P. J. 1993 Optimal excitation of three-dimensional perturbations in viscous constant shear flow. *Phys. Fluids A* **5 (6)**, 1390–1400.

FLORYAN, J. M. 2003 Vortex instability in a diverging-converging channel. *J. Fluid Mech.* **482**, 17–50.

FLORYAN, J. M. 2005 Two-dimensional instability of flow in a rough channel. *Phys. Fluids* **17, 044101**, 1–8.

FLORYAN, J. M. 2007 Three-dimensional instabilities of laminar flow in a rough channel and the concept of hydraulically smooth wall. *European Journal of Mechanics B/Fluids* **26**, 305–329.

FLORYAN, J. M. & FLORYAN, C. 2010 Traveling wave instability in a diverging-converging channel. *Fluid Dyn. Res.* **42,2**, 025509.

GASTER, M. 1962 A note on the relation between temporally-increasing and spatially-increasing disturbances in hydrodynamic stability. *J. Fluid Mech.* **14 (2)**, 222–224.

GASTER, M. 1968 Growth of disturbances in both space and time. *Phys. of Fluids* **11 (4)**, 723–727.

GASTER, M. 1974 On the effects of boundary layer growth on flow stability. *J. Fluid Mech.* **66**, 465–480.

GASTER, M. 1975 A theoretical model of a wavepacket in the boundary layer on a flat plate. *Proc. R. Soc. London A* **347**, 271–289.

GASTER, M. 2000 On the growth of waves in boundary layers. *J. Fluid Mech.* **424**, 367–377.

GEORGIOU, G. A. & EAGLES, P. M. 1985 The stability of flows in channels with small wall curvature. *J. Fluid Mech* **159**, 259–287.

GHADDAR, N. K., KORCZAK, K. Z., MIKIC, B. B. & PATERA, A. T. 1986 Numerical investigation of incompressible flow in grooved channels. part 1.stability and self-sustained oscillations. *J. Fluid Mech.* **163**, 99–127.

GLAUERT, M. B. 1956 The wall jet. *J. Fluid Mech.* **1**, 625–643.

GONZALEZ, L. M., THEOFILIS, V. & GOMEZ-BLANCO, R. 2007 Finite element methods for viscous incompressible biglobal instability analysis on unstructured meshes. *AIAA Journal* **45 (4)**, 840.

GOVINDARAJAN, R. 2004 Effect of miscibility on linear instability of two fluid channel flow. *Int. J. Multiphase flow* **30**, 1177–1192.

GOVINDARAJAN, R. & NARASIMHA, R. 1995 Stability of spatially developing boundary layers in pressure gradients. *J. Fluid Mech.* **300**, 117–147.

GOVINDARAJAN, R. & NARASIMHA, R. 1997 A low order theory for stability of non-parallel boundary layer flows. *Proceedings: Mathematical, Physical and Engineering Sciences* **453(1967)**, 2537–2549.

GOVINDARAJAN, R., V., L. S., I., P. & SAMEEN, A. 2003 Stabilisation of hydrodynamic flows by small viscosity stratification. *Phy. Rev., E.* **67** (026310), 026310.

GOVINDARAJAN, R., V., L. S. & PROCACCIA, I. 2001 Retardation of the onset of turbulence by minor viscosity contrasts. *Physical Review Letters* **87** (17), 174501.

HAMADICHE, SCOTT & JEANDEL 1994 Temporal stability of jeffery-hamel flow. *J. Fluid Mech* **268**, 71–88.

HEIN, S., HOHAGE, T. & KOCH, W. 2004 On resonances in open systems. *J. Fluid Mech.* **506**, 255–284.

HENNINGSON, D. S. 1996 Comment on "transition in shear flows: non-linear normality versus non-normal linearity" [phys. fluids 7,3060 (1995)]. *Phys. Fluids* **8**, 2257–2258.

HENNINGSON, D. S. & AKERVIK, E. 2008 The use of global modes to understand transition and perform flow control. *Phys. of Fluids* **20**, 031302.

HERBERT, T. 1997 Parabolized stability equations. *Annu. Rev. Fluid. Mech.* **29**, 245–283.

HERWIG, H., GLOSS, D. & WENTERODT, T. 2008 A new approach to understanding and modelling the influence of wall roughness on friction factors for pipe and channel flows. *J. Fluid Mech.* **613**, 35–53.

HOF, B., VAN DOORNE, C. W. H., WESTERWEEL, J., NIEUWSTADT, F. T. M., FAISST, H., ECKHARDT, B., WEDIN, H., KERSWELL, R. R. & WALEFFE, F. 2004 Experimental observation of nonlinear traveling waves in turbulent pipe flow. *Science* **305**, 1594–1598.

HOF, B., JUEL, A. & MULLIN, T. 2003 Scaling of the turbulence transition threshold in a pipe. *Phys. Rev. Lett.* **91**, 244502.

HUERRE, P. & MONKEWITZ, P. A. 1985 Absolute and convective instabilities in free shear layers. *J. Fluid Mech.* **159**, 151–168.

HUERRE, P. & MONKEWITZ, P. A. 1990 Local and global instabilities in spatially developing flows. *Annual Review of Fluid Mechanics* **22**, 473–537.

AN DG J KUNKEL, L. I. L. & SMITS, A. J. 2008 Flow in a commercial steel pipe. *J. Fluid Mech.* **595**, 323–339.

JACKSON, C. P. 1987 A finite-element study of the onset of vortex shedding in flow past variously shaped bodies. *J. Fluid Mech.* **182**, 23–45.

JACKSON, D. & LAUNDER, B. 2007 Osborned reynolds and the publication of his papers on turbulent flow. *Annual Review of Fluid Mechanics* **39**, 19–35.

KARNIADAKIS, G. E., MIKIC, B. B. & PATERA, A. T. 1922 Minimum-dissipation transport enhancement by flow destabilization: Reynold's analogy revisited. *J. Fluid Mech.* **192**, 365–391.

KERSWELL, R. R., TUTTY, O. R. & DRAZIN, P. G. 2004 Steady nonlinear waves in diverging channel flow. *J. Fluid Mech.* **501**, 231–250.

KUNDU, P. K. & COHEN, I. M. 2004 *Fluid Mechanics*, 8th edn. Elsevier.

LEE, N. Y., SCHULTZ, W. W. & BOYD, J. P. 1989 Stability of fluid in a rectangular enclosure by spectral method. *Journal of Heat and Mass Transfer* **32 (3)**, 513–520.

LEVIN, O., CHERNORAY, V. G., LOFDAHL, L. & HENNINGSON, D. 2005 A study of the blasius wall jet. *Journal of Fluid Mechanics* **539**, 313–347.

LIN, C. C. 1961 Some mathematical problems in the theory of the stability of parallel flows. *J. Fluid Mech.* **10, 3**, 430–438.

LIN, R. S. & MALIK, M. R. 1996 On the stability of attachment-line boundary layers. part 2. the incompressible swept hiemenz flow. *J. Fluid Mech.* **311**, 239–255.

LIN, R. S. & MALIK, M. R. 1997 On the stability of attachment-line boundary layers. part 2. the effecting of leading-edge curvature. *J. Fluid Mech.* **333**, 125–137.

LINGWOOD, R. J. 1995 Absolute instability of the boundary layer on a rotating disk. *J. Fluid Mech.* **299**, 17–33.

MARQUET, O., LOMBARDI, M., CHOMAZ, J. M., SIPP, D. & JACQUIN, L. 2009 Direct and adjoint global modes of a recirculation bubble: lift-up and convective non-normalities. *J. Fluid Mech.* **622**, 1–21.

MARTIN, D., CARRIERE, P. & MONKEWITZ, P. A. 2006 Three dimensional global instability modes associated with a localized hot spot in rayleigh-benard-poiseuille convection. *J. Fluid Mech.* **551**, 275–301.

MCALPINE, A. & DRAZIN, P. G. 1998 On the spatio-temporal development of small perturbations of jeffery-hamel flows . *Fluid Dynamics Research* **22**, 123–138.

MELE, P., MORGANTI, M., SCIBILLA, M. F. & LASEK, A. 1986 Behaviour of wall jet in lanimar-to-turbulent transition. *AIAA J.* **24**, 938–939.

MITTAL, S. & KUMAR, B. 2003 Flow past a rotating cylinder. *J. Fluid Mech.* **476**, 303–334.

MITTAL, S. & KUMAR, B. 2007 A stabilized finite element method for global analysis of convective instabilities in nonparallel flows. *Phys. of Fluids* **19**, 008105.

MITTAL, S. & SINGH, S. 2005 Vortex induced vibrations at subcritical re. *J. Fluid Mech.* **534**, 185–194.

MONKEWITZ, HUERRE & CHOMAZ 1993 Global linear stability analysis of weakly non-parallel shear flows. *J. Fluid Mech* **251**, 1–20.

MORZYNSKI, M., AFANASIEV, K. & THIELE, F. 1999 Solution of the eigenvalue problems resulting from global non-parallel flow stability analysis. *Computer methods in applied mechanics and Engineering* **169**, 161–176.

NAKAYA, C. & HASEGAWA, E. 1970 Stability of steady flow in a diverging channel. *Phys. Fluids* **13** (12), 2904–2906.

NAYAR, N. & ORTEGA, J. M. 1993 Computation of selected eigenvalues of generalized eigenvalue problems. *Journal of Computational Physics* **108**, 8–14.

NISHIMURA, T., BIAN, Y., KUNITSUGU, K. & MOREGA, A. M. 2003 Fluid flow and mass transfer in a sinusoidal wavy-walled tube at moderate reynolds numbers. *Heat Transer - Asian Research* **32, 7**, 650–661.

NISHIMURA, T., OHORI, Y. & KAWAMURA, Y. 1984 Flow characteristics in a channel with symmetric wavy wall for steady flow. *J. of Chemical Engineering of Japan* **17, 5**, 466–471.

NISHIOKA, M., IIDA, S. & ICHIKAWA, Y. 1975 An experimental investigation of the stability of plane Poiseuille flow. *J. Fluid Mech.* **72**, 731–751.

NOACK, B. R. & ECKELMANN, H. 1994 A global stability analysis of the steady and periodic cylinder wake. *J. Fluid Mech.* **270**, 297–330.

NOACK, B. R., KONIG, M. & ECKELMANN, H. 1993 Three-dimensional stability analysis of the periodic flow aroud a circular cylinder. *Phys. Fluids A* **5 (6)**, 1279–1281.

ORSZAG, S. A. 1971 Accurate solution of the orr-sommerfeld stability equation. *J. Fluid Mech.* **50, part 4**, 689–703.

PIER, B. 2007 Primary crossflow vortices, secondary absolute instabilities and their control in the rotating-disk boundary layer. *J. of Engg. Math.* **57**, 237–251.

PIER, B. 2008 Local and global instabilities in the wake of a sphere. *J. Fluid Mech.* **603**, 39–61.

PIERREHUMBERT, R. T. 1986 Universal short-wave instability of two-dimensional eddies in an inviscid fluid. *Phys. Rev. Letters* **57, 17**, 2157–60.

PUTKARADZE, V. & VOROBIEFF, P. 2006 Instabilities, bifurcations, and multiple solutions in expanding channel flows. *Phys. Rev. Lett.* **97**, 144502.

REDDY, S. C. & HENNINGSON, D. S. 1993 Energy growth in viscous channel flows. *J. Fluid Mech.* **252**, 209–238.

REDDY, S. C. & HENNINGSON, D. S. 1994 On the role of linear mechanisms in transition to turbulence. *Phys. Fluids* **6**, 1396.

REDDY, S. C., SCHMID, P. J., BAGGET, J. S. & HENNINGSON, D. S. 1998 On stability of streamwise streaks and transition thresholds in plane channel flows. *J. Fluid Mech.* **365**, 269–303.

SAAD, Y. 1980 Variations of arnoldi's method for computing eigenelements of large unsymmetric matrices. *Linear Algebra Applications* **34**, 269–295.

SAAD, Y. & SCHULTZ, M. H. 1986 Gmres: A generalized minimal residual algorithm for solving nonsymmetric linear systems. *SIAM J. Sci. Stat. Comput.* **7 (3)**, 856–869.

SAHU, K. C. 2003 Numerical computation of spatially developing flows by full-multigrid technique. Master's thesis, Jawaharlal Nehru Centre for Advanced Scientific Research.

SAHU, K. C. 2004 A possible linear instability mechanism in small-scale pipe flows. *Proceedings of the Sixth IUTAM Symposium on Laminar-Turbulent Transition, Bangalore, India* .

SAHU, K. C. & GOVINDARAJAN, R. 2005 Stability of flow through a slowly diverging pipe. *J. Fluid Mech* **531**, 325–334.

SAHU, K. C., SAMEEN, A. & GOVINDARAJAN, R. 2008 The relative roles of divergence and velocity slip in the stability of plane channel flow. *The European Phys. J. Appl. Phys.* **44**, 104–107.

SAHU, K. C., VALLURI, P., SPELT, P. D. M. & MATAR, O. K. 2007 Linear instability of pressure-driven channel flow of a newtonian and a herschel-bulkley fluid. *Phys. Fluids* **19**, 122101.

SAMEEN, A. & GOVINDARAJAN, R. 2007 The effect of wall heating on instability of channel flow. *J. Fluid Mech.* **577**, 417–442.

SCHATZ, M. F., BARKLEY, D. & SWINNEY, H. L. 1995 Instability in a spatially periodic open flow. *Phys. Fluids* **7 (2)**, 344–358.

SCHLICHTING, H. 2000 *Boundary Layer Theory*, 8th edn. Springer.

SCHMID, P. J. 2007 Nonmodal stability theory. *Annual Review of Fluid Mechanics* **39**, 129–162.

SCHMID, P. J. & HENNINGSON, D. S. 2001 *Stability and Transition in Shear Flows*. Springer.

SCHMID, P. J. & HENNINGSON, D. S. 2002 On the stability of a falling liquid curtain. *J. Fluid Mech.* **463**, 163–171.

SCIBILIA, M.-F. 2003 Variation of transition characteristics in a wall jet. *J. of Thermal Science* **12** (2).

SEIDEL, J. & FASEL, H. 2001 Numerical investigation of heat transfer mechanisms in the forced laminar wall jet. *J. Fluid Mech.* **442**, 191–215.

SELVARAJAN, S., TULAPURKARA, E. G. & RAM, V. V. 1999 Stability characteristics of wavy walled channel flows. *Phys. Fluids* **11, 3**, 579–589.

SHANKAR, V. & KUMURAN, V. 2000 Stability of fluid flow in a flexible tube to non-axisymmetric disturbances. *J. Fluid. Mech.* **407**, 291–314.

SRINIVASAN, S., KLIKA, M., LUDWIG, M. H. & RAM, V. V. 1994 A beginner's guide to the use of the spectral collocation method for solving some eigenvalue problems in fluid mechanics. *Tech. Rep.*. National Aerospace Laboratories, Bangalore, India.

STUART, J. T. 1971 Nonlinear stability theory. *Annu. Rev. Fluid. Mech.* **3**, 347–370.

STURROCK, P. A. 1958 Kinematics of growing waves. *Phys. Review* **112**, 1488–1503.

SZUMBARSKI, J. & FLORYAN, J. M. 2006 Transient disturbance growth in a corrugated channel. *J. Fluid Mech.* **568**, 243–272.

TAKAOKA, M., SANO, T., YAMAMOTO, H. & MIZUSHIMA, J. 2009 Convective instability of flow in a symmetric channel with spatially periodic structures. *Phys. Fluids* **21**, 1–10.

TATSUMI, T. & YOSHIMURA, T. 1990 Stability of the laminar flow in a rectangular duct. *J. Fluid Mech.* **212**, 437–449.

THEOFILIS, V. 1997 On the verification and extension of the gortler-hammerlin assumption in three-dimensional incompressible swept attachment-line buondary layer fow. *Tech. report.* **IB 223-97, A 44, DLR**.

THEOFILIS, V. 2003 Advances in global linear instability analysis of non-parallel and three-dimensional flows. *Progress in Aerospace Sciences* **39**, 249–315.

THEOFILIS, V., DUCK, P. W. & OWEN, J. 2004 Viscous linear stability analysis of rectangular duct and cavity flows. *J. Fluid Mech.* **505**, 249–286.

THEOFILIS, V., FEDEROV, A., OBRIST, D. & DALLMANN, U. C. 2003 The extended gortler-hammerlin model for linear instability of three-dimensional incompressible swept attachment-line boundary layer flow. *J. Fluid Mech.* **487**, 271–313.

THEOFILIS, V., HEIN, S. & DALLMANN, U. 2000 On the origins of unsteadiness and three-dimensionality in a laminar separation bubble. *Phi. Tran. R. Soc. Lond. A* **358**, 3229–3246.

THEOFILIS, V., SHERWIN, S. J. & ABDESSEMED, N. 2005 On global instabilities of separated bubble flows and their control in external and internal aerodynamic applications. *NATO RTO-AVT* **RTO-AVT-111**, 21–1 to 21–9.

TILTON, N. & CORTELEZZI, L. 2006 The destabilizing effects of wall permeability in channel flow: A linear stability analysis. *Phys. Fluids* **18**, 051702.

TILTON, N. & CORTELEZZI, L. 2008 Linear stability analysis of pressure-driven flows in channels with porous walls. *J. Fluid Mech.* **604**, 411–445.

TOLLMIEN, W. 1929 ber die entstehung der turbulenz. 1. mitteilung, nachr. ges. wiss. gttingen. *Math. Phys. Klasse* pp. 21–44.

TUMIN, A. & AIZATULIN, L. 1997 Instability and receptivity of laminar wall jets. *Theoret. Comput. Fluid Dynamics* **9**, 33–45.

TUTTY, O. R. 1996 Nonlinear development of flow in channels with non-parallel walls. *J. Fluid Mech.* **326**, 265–284.

URIBE, BRAVO & PERALTA 1997 On the stability of jeffery-hamel flow. *Phys. Fluids* **9**, 1070–2798.

VENKATESH, T. N., SARASAMMA, V. R., RAJALAKSHMY, S., SAHU, K. C. & GOVINDARAJAN, R. 2006 Super-linear speedup of a parallel multigrid navier-stokes solver on flosolver. *Current Science* **88(4)**, 589–593.

WALEFFE, F. 1995 Transition in shear flows: non-linear normality versus non-normal linearity. *Phys. Fluids* **7** (12), 3060.

WALL, D. P. & WILSON, S. K. 1996 The linear stability of channel flow of fluid with temperature-dependent viscosity. *J. Fluid Mech.* **323**, 107–132.

ZEBIB, A. 1987 Stability of viscous flow past a circular cylinder. *Journal of Engineering Mathematics* **21**, 155–165.